HIGH-THROUGHPUT EXPERIMENTATION OF THE BUCHWALD-HARTWIG AMINATION FOR REACTION SCOUTING AND GUIDED SYNTHESIS

by

Damien E. Dobson

A Thesis

Submitted to the Faculty of Purdue University

In Partial Fulfillment of the Requirements for the degree of

Master of Science

Department of Chemistry

West Lafayette, Indiana

August 2022

THE PURDUE UNIVERSITY GRADUATE SCHOOL
STATEMENT OF COMMITTEE APPROVAL

Dr. David Thompson, Chair

Department of Chemistry

Dr. R. Graham Cooks

Department of Chemistry

Dr. Herman Sintim

Department of Chemistry

Approved by:

Dr. Christine Hrycyna

I dedicate this Thesis to my father, for he provided me with the wisdom, strength, and fortitude responsible for the man I have become.

ACKNOWLEDGMENTS

I would like to thank the Thompson group for the support throughout my tenure at Purdue University. Without them, the experience would not have been as remotely fruitful. Additionally, I would like to thank Dr. Michael McGuire for his advisory role in my degree, and his wise insight on chemical industry.

As part of my professional development, the words of Xenophon, Alexander Hamilton, and Augustus bestowed me great wisdom with respect to justice, prudence, and overall strength required to travel the graduate school journey as a young man. These great men led me through difficult times.

Finally, I'd to thank my mother, father, and brother for providing me with support and love over the years to overcome adversity, and to continue to persevere. They showed me that my options in life are limitless.

TABLE OF CONTENTS

LIST OF TABLES 6
LIST OF FIGURES 7
ABSTRACT 12
CHAPTER 1. INTRODUCTION 13
1.1-Overview of High Throughput Experimentation (HTE) 13
1.1.1 Use of HTE To Study C-N Bond Forming Reactions 14
1.2 Buchwald-Hartwig Amination 16
1.3 References 18
CHAPTER 2. HIGH THROUGHPUT EXPERIMENTATION CAMPAIGN OF THE BUCHWALD-HARTWIG AMINATION TO INVESTIGATE SUBSTRATE COMPATIBILITY 22
2.1 Introduction 22
2.2 Methods 26
2.2.1 Order of Addition Experiment 29
2.2.2 LC-MS Validation of Signal-to-Noise Thresholds for HTE 30
2.2.3 Broad Substrate Scope HTE 30
2.3 Results and Discussion 32
2.3.1 Order of Addition Experiment 32
2.3.2 LC-MS Validation of Signal-to-Noise Thresholds for HTE 33
2.3.3 Broad Substrate Scope HTE 36
2.4 Conclusion 41
2.5 Supplementary Information 42
2.5.1 Synthesis Experimentals 42
2.5.2 Order of Addition HTE Contour Plots 46
2.5.3 Broad Substrate Screen Heat Maps 49
2.5.4 NMR Spectra 69
2.6 References 76

LIST OF TABLES

Table 1. Overview of the different reagent addition orders investigated in the HTE. 29

Table 2. Overview of the different reactions condition parameters investigated during the order of addition HTE. Each column represents the different values tested within that parameter. Rows do not indicate dependance. 30

Table 3. Results from LC-MS S/N validation study. The S/N values are the ones extrapolated through the DESI-MS data in both ion modes. FA = Formic acid buffer, AmAc = Ammonium acetate (0.01 M) buffer. 34

Table 4. Overview of observed trends for substate compatibility with the respective ancillary ligands. 40

LIST OF FIGURES

Figure 1. Overview of standard methods for aryl C-N bond formation. 17

Figure 2. Catalytic cycle of the Buchwald-Hartwig amination. 18

Figure 3. Structures of aryl and aryl(pseudo) halides used in the HTE campaign. Structures in red were purchased in the phenolic form and converted to the respecting sulfonyl ester. 24

Figure 4. Structures of the 24 nitrogen-containing nucleophiles used in the HTE campaign. 25

Figure 5. Structures of the 10 biaryl monophosphine ligands and xanthene based bis-phosphine. 25

Figure 6. Beckman Coulter i7 liquid handling robot used for the HTE campaign. 27

Figure 7. 96-well aluminum heating block inside the Peltier heater. 28

Figure 8. Contrast plot from the order of addition HTE of the data at the 2 h mark. The larger the dot at the intersection of condition labels, the greater the product ion count from observed in DESI-MS. 33

Figure 9. Negative ion heat map from the *t*BuXPhos experiment after being heated at 100 °C for 2 h. (1) is 50% *t*BuOH in H_2O. (2) is 30% 1,4-Dioxane in *t*BuOH. (3) is 10% *t*BuOH in PhMe. (4) is 20% *t*BuOH, 30% 1,4-Dioxane, 50% H_2O. 37

Figure 10. Positive ion heat map from the *t*BuXPhos experiment after being heated at 100 °C for 2 h. (1) is 50% *t*BuOH in H_2O. (2) is 30% 1,4-Dioxane in *t*BuOH. (3) is 10% *t*BuOH in PhMe. (4) is 20% *t*BuOH, 30% 1,4-Dioxane, 50% H_2O. 38

Figure 11. Negative ion heat map from the *t*BuXPhos experiment after sitting at RT for 2 h. (1) is 50% *t*BuOH in H_2O. (2) is 30% 1,4-Dioxane in *t*BuOH. (3) is 10% *t*BuOH in PhMe. (4) is 20% *t*BuOH, 30% 1,4-Dioxane, 50% H_2O. 38

Figure 12. Positive ion heat map from the *t*BuXPhos experiment after sitting at RT for 2 h. (1) is 50% *t*BuOH in H_2O. (2) is 30% 1,4-Dioxane in *t*BuOH. (3) is 10% *t*BuOH in PhMe. (4) is 20% *t*BuOH, 30% 1,4-Dioxane, 50% H_2O. 39

Figure 13. Contrast plot from the order of addition HTE of the data at the 1 h mark. The larger the dot at the intersection of condition labels, the greater the product ion count from observed in DESI-MS. 46

Figure 14. Contrast plot from the order of addition HTE of the data at the 3 h mark. The larger the dot at the intersection of condition labels, the greater the product ion count from observed in DESI-MS. 47

Figure 15. Contrast plot from the order of addition HTE of the data at the 4 h mark. The larger the dot at the intersection of condition labels, the greater the product ion count from observed in DESI-MS. 48

Figure 16. Positive ion heat map from the XPhos experiment after sitting at RT for 2 h. (1) is 50% *t*BuOH in H_2O. (2) is 30% 1,4-Dioxane in *t*BuOH. (3) is 10% *t*BuOH in PhMe. (4) is 20% *t*BuOH, 30% 1,4-Dioxane, 50% H_2O. 49

Figure 17. Positive ion heat map from the XPhos experiment after sitting at 100 °C for 2 h. (1) is 50% *t*BuOH in H_2O. (2) is 30% 1,4-Dioxane in *t*BuOH. (3) is 10% *t*BuOH in PhMe. (4) is 20% *t*BuOH, 30% 1,4-Dioxane, 50% H_2O. 49

Figure 18. Negative ion heat map from the XPhos experiment after sitting at RT for 2 h. (1) is 50% *t*BuOH in H_2O. (2) is 30% 1,4-Dioxane in *t*BuOH. (3) is 10% *t*BuOH in PhMe. (4) is 20% *t*BuOH, 30% 1,4-Dioxane, 50% H_2O. 50

Figure 19. Negative ion heat map from the XPhos experiment after sitting at 100 °C for 2 h. (1) is 50% *t*BuOH in H_2O. (2) is 30% 1,4-Dioxane in *t*BuOH. (3) is 10% *t*BuOH in PhMe. (4) is 20% *t*BuOH, 30% 1,4-Dioxane, 50% H_2O. 50

Figure 20. Positive ion heat map from the Me_3(OMe)*t*BuXPhos experiment after sitting at RT for 2 h. (1) is 50% *t*BuOH in H_2O. (2) is 30% 1,4-Dioxane in *t*BuOH. (3) is 10% *t*BuOH in PhMe. (4) is 20% *t*BuOH, 30% 1,4-Dioxane, 50% H_2O. 51

Figure 21. Positive ion heat map from the Me_3(OMe)*t*BuXPhos experiment after sitting at 100 °C for 2 h. (1) is 50% *t*BuOH in H_2O. (2) is 30% 1,4-Dioxane in *t*BuOH. (3) is 10% *t*BuOH in PhMe. (4) is 20% *t*BuOH, 30% 1,4-Dioxane, 50% H_2O. 51

Figure 22. Negative ion heat map from the Me_3(OMe)*t*BuXPhos experiment after sitting at RT for 2 h. (1) is 50% *t*BuOH in H_2O. (2) is 30% 1,4-Dioxane in *t*BuOH. (3) is 10% *t*BuOH in PhMe. (4) is 20% *t*BuOH, 30% 1,4-Dioxane, 50% H_2O. 52

Figure 23. Negative ion heat map from the Me_3(OMe)*t*BuXPhos experiment after sitting at 100 °C for 2 h. (1) is 50% *t*BuOH in H_2O. (2) is 30% 1,4-Dioxane in *t*BuOH. (3) is 10% *t*BuOH in PhMe. (4) is 20% *t*BuOH, 30% 1,4-Dioxane, 50% H_2O. 52

Figure 24. Positive ion heat map from the Me_4*t*BuXPhos experiment after sitting at RT for 2 h. (1) is 50% *t*BuOH in H_2O. (2) is 30% 1,4-Dioxane in *t*BuOH. (3) is 10% *t*BuOH in PhMe. (4) is 20% *t*BuOH, 30% 1,4-Dioxane, 50% H_2O. 53

Figure 25. Positive ion heat map from the Me_4*t*BuXPhos experiment after sitting at 100 °C for 2 h. (1) is 50% *t*BuOH in H_2O. (2) is 30% 1,4-Dioxane in *t*BuOH. (3) is 10% *t*BuOH in PhMe. (4) is 20% *t*BuOH, 30% 1,4-Dioxane, 50% H_2O. 53

Figure 26. Negative ion heat map from the Me_4*t*BuXPhos experiment after sitting at RT for 2 h. (1) is 50% *t*BuOH in H_2O. (2) is 30% 1,4-Dioxane in *t*BuOH. (3) is 10% *t*BuOH in PhMe. (4) is 20% *t*BuOH, 30% 1,4-Dioxane, 50% H_2O. 54

Figure 27. Negative ion heat map from the Me_4*t*BuXPhos experiment after sitting at 100 °C for 2 h. (1) is 50% *t*BuOH in H_2O. (2) is 30% 1,4-Dioxane in *t*BuOH. (3) is 10% *t*BuOH in PhMe. (4) is 20% *t*BuOH, 30% 1,4-Dioxane, 50% H_2O. 54

Figure 28. Positive ion heat map from the BrettPhos experiment after sitting at RT for 2 h. (1) is 50% *t*BuOH in H_2O. (2) is 30% 1,4-Dioxane in *t*BuOH. (3) is 10% *t*BuOH in PhMe. (4) is 20% *t*BuOH, 30% 1,4-Dioxane, 50% H_2O. 55

Figure 29. Positive ion heat map from the BrettPhos experiment after sitting at 100 °C for 2 h. (1) is 50% *t*BuOH in H_2O. (2) is 30% 1,4-Dioxane in *t*BuOH. (3) is 10% *t*BuOH in PhMe. (4) is 20% *t*BuOH, 30% 1,4-Dioxane, 50% H_2O. 55

Figure 30. Negative ion heat map from the BrettPhos experiment after sitting at RT for 2 h. (1) is 50% *t*BuOH in H_2O. (2) is 30% 1,4-Dioxane in *t*BuOH. (3) is 10% *t*BuOH in PhMe. (4) is 20% *t*BuOH, 30% 1,4-Dioxane, 50% H_2O. 56

Figure 31. Negative ion heat map from the BrettPhos experiment after sitting at 100 °C for 2 h. (1) is 50% *t*BuOH in H_2O. (2) is 30% 1,4-Dioxane in *t*BuOH. (3) is 10% *t*BuOH in PhMe. (4) is 20% *t*BuOH, 30% 1,4-Dioxane, 50% H_2O. 56

Figure 32. Positive ion heat map from the *t*BuBrettPhos experiment after sitting at RT for 2 h. (1) is 50% *t*BuOH in H_2O. (2) is 30% 1,4-Dioxane in *t*BuOH. (3) is 10% *t*BuOH in PhMe. (4) is 20% *t*BuOH, 30% 1,4-Dioxane, 50% H_2O. 57

Figure 33. Positive ion heat map from the *t*BuBrettPhos experiment after sitting at 100 °C for 2 h. (1) is 50% *t*BuOH in H_2O. (2) is 30% 1,4-Dioxane in *t*BuOH. (3) is 10% *t*BuOH in PhMe. (4) is 20% *t*BuOH, 30% 1,4-Dioxane, 50% H_2O. 57

Figure 34. Negative ion heat map from the *t*BuBrettPhos experiment after sitting at RT for 2 h. (1) is 50% *t*BuOH in H_2O. (2) is 30% 1,4-Dioxane in *t*BuOH. (3) is 10% *t*BuOH in PhMe. (4) is 20% *t*BuOH, 30% 1,4-Dioxane, 50% H_2O. 58

Figure 35. Negative ion heat map from the *t*BuBrettPhos experiment after sitting at 100 °C for 2 h. (1) is 50% *t*BuOH in H_2O. (2) is 30% 1,4-Dioxane in *t*BuOH. (3) is 10% *t*BuOH in PhMe. (4) is 20% *t*BuOH, 30% 1,4-Dioxane, 50% H_2O. 58

Figure 36. Positive ion heat map from the AdBrettPhos experiment after sitting at RT for 2 h. (1) is 50% *t*BuOH in H_2O. (2) is 30% 1,4-Dioxane in *t*BuOH. (3) is 10% *t*BuOH in PhMe. (4) is 20% *t*BuOH, 30% 1,4-Dioxane, 50% H_2O. 59

Figure 37. Positive ion heat map from the AdBrettPhos experiment after sitting at 100 °C for 2 h. (1) is 50% *t*BuOH in H_2O. (2) is 30% 1,4-Dioxane in *t*BuOH. (3) is 10% *t*BuOH in PhMe. (4) is 20% *t*BuOH, 30% 1,4-Dioxane, 50% H_2O. 59

Figure 38. Negative ion heat map from the AdBrettPhos experiment after sitting at RT for 2 h. (1) is 50% *t*BuOH in H_2O. (2) is 30% 1,4-Dioxane in *t*BuOH. (3) is 10% *t*BuOH in PhMe. (4) is 20% *t*BuOH, 30% 1,4-Dioxane, 50% H_2O. 60

Figure 39. Negative ion heat map from the AdBrettPhos experiment after sitting at 100 °C for 2 h. (1) is 50% *t*BuOH in H_2O. (2) is 30% 1,4-Dioxane in *t*BuOH. (3) is 10% *t*BuOH in PhMe. (4) is 20% *t*BuOH, 30% 1,4-Dioxane, 50% H_2O. 60

Figure 40. Positive ion heat map from the XantPhos experiment after sitting at RT for 2 h. (1) is 50% *t*BuOH in H_2O. (2) is 30% 1,4-Dioxane in *t*BuOH. (3) is 10% *t*BuOH in PhMe. (4) is 20% *t*BuOH, 30% 1,4-Dioxane, 50% H_2O. 61

Figure 41. Positive ion heat map from the XantPhos experiment after sitting at 100 °C for 2 h. (1) is 50% *t*BuOH in H_2O. (2) is 30% 1,4-Dioxane in *t*BuOH. (3) is 10% *t*BuOH in PhMe. (4) is 20% *t*BuOH, 30% 1,4-Dioxane, 50% H_2O. 61

Figure 42. Negative ion heat map from the XantPhos experiment after sitting at RT for 2 h. (1) is 50% *t*BuOH in H_2O. (2) is 30% 1,4-Dioxane in *t*BuOH. (3) is 10% *t*BuOH in PhMe. (4) is 20% *t*BuOH, 30% 1,4-Dioxane, 50% H_2O. 62

Figure 43. Negative ion heat map from the XantPhos experiment after sitting at 100 °C for 2 h. (1) is 50% *t*BuOH in H_2O. (2) is 30% 1,4-Dioxane in *t*BuOH. (3) is 10% *t*BuOH in PhMe. (4) is 20% *t*BuOH, 30% 1,4-Dioxane, 50% H_2O. 62

Figure 44. Positive ion heat map from the EPhos experiment after sitting at RT for 2 h. (1) is 50% *t*BuOH in H_2O. (2) is 30% 1,4-Dioxane in *t*BuOH. (3) is 10% *t*BuOH in PhMe. (4) is 20% *t*BuOH, 30% 1,4-Dioxane, 50% H_2O. 63

Figure 45. Positive ion heat map from the EPhos experiment after sitting at 100 °C for 2 h. (1) is 50% *t*BuOH in H_2O. (2) is 30% 1,4-Dioxane in *t*BuOH. (3) is 10% *t*BuOH in PhMe. (4) is 20% *t*BuOH, 30% 1,4-Dioxane, 50% H_2O. 63

Figure 46. Negative ion heat map from the EPhos experiment after sitting at RT for 2 h. (1) is 50% *t*BuOH in H_2O. (2) is 30% 1,4-Dioxane in *t*BuOH. (3) is 10% *t*BuOH in PhMe. (4) is 20% *t*BuOH, 30% 1,4-Dioxane, 50% H_2O. 64

Figure 47. Negative ion heat map from the EPhos experiment after sitting at 100 °C for 2 h. (1) is 50% *t*BuOH in H_2O. (2) is 30% 1,4-Dioxane in *t*BuOH. (3) is 10% *t*BuOH in PhMe. (4) is 20% *t*BuOH, 30% 1,4-Dioxane, 50% H_2O. 64

Figure 48. Positive ion heat map from the SPhos experiment after sitting at RT for 2 h. (1) is 50% *t*BuOH in H_2O. (2) is 30% 1,4-Dioxane in *t*BuOH. (3) is 10% *t*BuOH in PhMe. (4) is 20% *t*BuOH, 30% 1,4-Dioxane, 50% H_2O. 65

Figure 49. Positive ion heat map from the SPhos experiment after sitting at 100 °C for 2 h. (1) is 50% *t*BuOH in H_2O. (2) is 30% 1,4-Dioxane in *t*BuOH. (3) is 10% *t*BuOH in PhMe. (4) is 20% *t*BuOH, 30% 1,4-Dioxane, 50% H_2O. 65

Figure 50. Negative ion heat map from the SPhos experiment after sitting at RT for 2 h. (1) is 50% *t*BuOH in H_2O. (2) is 30% 1,4-Dioxane in *t*BuOH. (3) is 10% *t*BuOH in PhMe. (4) is 20% *t*BuOH, 30% 1,4-Dioxane, 50% H_2O. 66

Figure 51. Negative ion heat map from the SPhos experiment after sitting at 100 °C for 2 h. (1) is 50% *t*BuOH in H_2O. (2) is 30% 1,4-Dioxane in *t*BuOH. (3) is 10% *t*BuOH in PhMe. (4) is 20% *t*BuOH, 30% 1,4-Dioxane, 50% H_2O. 66

Figure 52. Positive ion heat map from the RuPhos experiment after sitting at RT for 2 h. (1) is 50% *t*BuOH in H_2O. (2) is 30% 1,4-Dioxane in *t*BuOH. (3) is 10% *t*BuOH in PhMe. (4) is 20% *t*BuOH, 30% 1,4-Dioxane, 50% H_2O. 67

Figure 53. Positive ion heat map from the RuPhos experiment after sitting at 100 °C for 2 h. (1) is 50% *t*BuOH in H_2O. (2) is 30% 1,4-Dioxane in *t*BuOH. (3) is 10% *t*BuOH in PhMe. (4) is 20% *t*BuOH, 30% 1,4-Dioxane, 50% H_2O. 67

Figure 54. Negative ion heat map from the RuPhos experiment after sitting at RT for 2 h. (1) is 50% *t*BuOH in H_2O. (2) is 30% 1,4-Dioxane in *t*BuOH. (3) is 10% *t*BuOH in PhMe. (4) is 20% *t*BuOH, 30% 1,4-Dioxane, 50% H_2O. 68

Figure 55. Negative ion heat map from the RuPhos experiment after sitting at 100 °C for 2 h. (1) is 50% *t*BuOH in H_2O. (2) is 30% 1,4-Dioxane in *t*BuOH. (3) is 10% *t*BuOH in PhMe. (4) is 20% *t*BuOH, 30% 1,4-Dioxane, 50% H_2O. 68

Figure 56. ^{1}H NMR spectrum of 2-nitro-4-(trifluoromethyl)phenyl trifluoromethanesulfonate in $CDCl_3$. 69

Figure 57. ^{1}H NMR spectrum of 4-acetyl-2-methoxyphenyl methanesulfonate in $CDCl_3$. 70

Figure 58. ^{1}H NMR spectrum of 3,5-dimethylphenyl methanesulfonate in $CDCl_3$. 71

Figure 59. ^{1}H NMR spectrum of methyl-2-(tosyloxy)benzoate in $CDCl_3$. 72

Figure 60. ^{1}H NMR spectrum of 4-chloro-3,5-dimethylphenyl trifluoromethanesulfonate in $CDCl_3$. 73

Figure 61. ^{1}H NMR spectrum of 3,4-dimethylphenyl-4-methylbenzenesulfonate in $CDCl_3$. 74

Figure 62. ^{1}H NMR spectrum of 4-(3,4,5-trimethoxyphenyl)morpholine in $CDCl_3$. 75

ABSTRACT

Aromatic C-N bond formation is critical for synthetic chemistry in pharmaceutical, agrochemical, and natural product synthesis. Due to the prevalence of this bond class, many synthetic routes have been developed over time to meet the demand. The most recent and robust C-N bond formation reaction is the palladium catalyzed Buchwald-Hartwig amination. Considering the importance of the Buchwald-Hartwig amination, a high-throughput experimentation (HTE) campaign was devised to create a library in which chemists can refer to optimal reaction conditions and ligand/catalyst choice based on the nature of their substrates to be coupled. This study showed trends for the appropriate choice of ligand and catalyst, along with what bases, temperatures, stoichiometries, and solvents are appropriate for the selected substrate combination at hand.

CHAPTER 1. INTRODUCTION

1.1-Overview of High Throughput Experimentation (HTE)

In the last 20 years, HTE has been introduced as a powerful tool for vast amounts of data acquisition, yet for organic synthesis HTE remains relatively underdeveloped.[1] Integrating the use of HTE as a means of supporting synthesis possesses great potential for discovering optimal reaction conditions and new potential pathways.[2,3] A large contributing factor to the significance of HTE is the ability to perform multiple reactions in parallel. This is contrary to the standard "one reaction at a time" approach. Utilizing the vast number of reactions that can be performed in a relatively small timeframe, the data obtained from these experiments can drastically reduce the need for trial-by-error, and man hours needed to achieve project goals. HTE providing insight on optimal temperature and solvent, stoichiometries, yield, by-products, and reproducibility all contribute to streamlining the reaction optimization/discovery process. Substrate compatibility for a specific reaction can also be investigated quickly and easily with HTE through testing multiple substrates in a single experiment. Furthermore, if proper controls and experimental design are incorporated, mechanistic insight on transformations is possible.

The use of micro scale quantities is typically used in HTE employing micromole to picomole ranges.[4] This is cost-advantageous to reaction discovery/optimization due to requiring only small quantities of substates to produce large data sets. Along with cost advantages, HTE also drastically reduces the amount of time and man-power required to achieve optimal reaction conditions for target-oriented synthesis. For established reactions, HTE can also be beneficial to optimize those that are found to be low-yielding, slow, or requiring excessive reagents.[5] The plethora of data that HTE can provide, along with the coupling of various analytical methods, massive data libraries can be compiled and used to inform machine learning and artificial intelligence platforms.[6,7] With respect to the future, creating these large libraries and utilizing computers to extrapolate trends from datasets can possibly revolutionize the manner synthesis is performed.

HTE systems frequently employ robots than can handle liquids, solids, or both. These tools allow for the dispensing of solutions and/or reagents in a fast and systematic manner to perform the desired reactions. Reaction vessels typically used include, but are not limited to 96-well plates, 384-well plates, and 24/96-well aluminum heating blocks. These blocks can then hold glass vials

that act as an individual reaction vessel. Aluminum heating blocks also possess the ability to have LED arrays installed to allow for photochemical reactions in a HTE setting. The robots are given the method set by the user for how the experiment is to be performed. This includes how much reagent, solvent, and substate; and where/how to dispense them into the respective reaction vessels. If robots aren't being used, manual pipetting can be utilized in the form of 8-channel pipettes. Each reaction well can possess a unique reaction, but to ensure trustworthy data sets, repeats of the same reaction and condition(s) are utilized to build statistical power into the experiment. In HTE, multi-variate screens are very widespread, but recently a large increase of design of experiment (DoE)-based experiments has been observed.[8–10] To assay these experiments, the reaction can be directly analyzed, or it can be extracted, diluted, and/or evaporated to prepare it for analysis. Typical analytical tools used for the analysis of a HTE include but are not limited to high or ultra-high pressure chromatography (HPLC/UPLC), electrospray ionization mass spectrometry (ESI-MS), atmospheric pressure chemical ionization mass spectrometry (APCI-MS), gas chromatography (GC), gas chromatography mass spectrometry (GC-MS), liquid chromatography mass spectrometry (LC-MS), matrix assisted laser desorption ionization time-of-flight mass spectrometry (MALDI-TOF-MS), and desorption electrospray ionization mass spectrometry (DESI-MS).

HTE has emerged as a vital means for synthetic methodology development especially in relation to the pharmaceutical industry.[11–13] Every year, it becomes harder to find new potential drug candidates making lead optimization and discovery a crucial endeavor. Methods such as HTE have allowed for large and continuously growing libraries of molecules to be screened more thoroughly in order to produce novel drugs.[14–16] HTE is increasingly being used in the academic realm, even though in the recent past it has conventionally been utilized in industry.[3] For the sake of ensuring safety, maximizing production, and confirming reproducibility in the chemical industry, it has been a long-time directive to automate the laboratory.[17] The advantages of HTE methods are so valuable that it has found its way into organic synthesis, catalysis, polymers, and materials chemistry.[18–20]

1.1.1 Use of HTE To Study C-N Bond Forming Reactions

Out of all transformations investigated with HTE, C-N bond forming reactions are the second most studied.[21] The Buchwald-Hartwig amination, a very prevalent reaction to form aryl

C-N bonds, was investigated by Sather and Martinot[22] using 5-membered heteroarenes and piperidine-based nucleophiles as substrates. Coupling of these substrates is challenging because they often lead to by-product formation due to protodehalogenation and ß-hydride elimination. They utilized HTE to determine an optimal catalyst choice, followed by experiments to find appropriate loadings of the catalyst. Using LC-MS to monitor these reactions, it was found that the base required for the reaction was causing degradation of the arene electrophile rendering the transformation ineffective. With this data in-hand, further experiments testing various bases, solvents, temperature, and catalyst loadings were carried out. Out of the 48 different nucleophiles and equal amount of aryl halides tested in the experiment, it was found that side reactions occurred with ester-containing substrates, along with poor reaction efficiency using alcohols and secondary amides.

Another example of HTE being used to gain insight on specific Buchwald-Hartwig transformations was done by Hayhow and coworkers[23] where they investigated the use of the Buchwald-Hartwig amination as a key-step in PROTAC synthesis. The strategy was to install the amine fragment on an isoindoline moiety using the Buchwald-Hartwig amination and crucially perform this key coupling as the last step of the sequence, rather than the first, to facilitate exploration of structural diversity. The HTE focused on the significance of the base and solvent used, along with compatibility of various amine nucleophiles with the isoindoline electrophile. Ultimately, they were able to optimize the reaction to be high yielding and gain the ability to selectively substitute all positions around the ring of the isoindoline.

In the medicinal chemistry realm, nucleophilic aromatic substitution (S_NAr) is a heavily used reaction for the formation of aryl C-N bonds. HTE has been used recently to investigate this transformation with a goal of finding substrate compatibility, and the implications of solvent/base. Thompson and coworkers[24] were able to utilize a liquid handling robot to perform 3072 unique S_NAr reactions using NMP as a solvent. DESI-MS was the key analytical tool in the study as only 3.5 seconds were required to analyze a single reaction. Using several rounds of HTE, they were able to test 4 different bases against 12 electrophiles and 8 amines. Data acquired through the HTE campaign was able to be analyzed and effectively translated to optimized continuous flow synthesis.

HTE was used again to study S_NAr reactions tailored to synthesize diacylglycerol acyltransferase 1 (DGAT1) inhibitors.[25] There were 43 different compounds synthesized which

required several rounds of HTE to achieve. Using a fixed set of nucleophiles, while varying electrophiles, base, and solvent, HTE allowed for a large array of compounds to be synthesized and tested for structure-activity trends. After all the compounds were isolated, a success rate of 81% was found for each substrate combination.

A testament to the ability of HTE to give valuable insight into chemical transformations with very little material required was exhibited by Cernak and coworkers.[26] They performed a HTE campaign initially using spiropiperidine and 2-fluoropyridine as substrates for S_NAr. S_NAr was a key step in their overall synthesis and HTE was sought to optimize it. On a small scale (~1 mg starting material for each reaction), 4 solvents and 6 bases were tested against the 2 substrates. The substrate scope was subsequently expanded to 6 different nucleophiles and electrophiles along with 4 different bases and solvents. UPLC-MS was used as the key analytical tool for the HTE campaign.

The Ullmann Coupling is a copper mediated coupling reaction that forms aryl C-N bonds. A HTE campaign was utilized to couple amines with DNA conjugated aryl iodides with the lowest Cu(I) loadings, and the most reaction efficiency.[27] The basis for the use of the Ullmann coupling was to avoid palladium cross-couplings due to regulatory concerns for the drug target. A large library of 6300 primary amines were tested against the DNA conjugated aryl iodide using >230 combinations of ligand, solvent, and base. UPLC-MS analysis was used to assay all the different reaction combinations. Additionally, the HTE gave valuable insight into the solubility aspects of the starting materials and the coupled products.

1.2 Buchwald-Hartwig Amination

Aryl amines and related heterocycles are extremely prevalent in pharmaceuticals, natural products, and agrochemicals.[28] The implications of the value of C-N bond formation were verified by a 2019 statistic stating that 80% of all drugs currently on the market contain C-N bonds.[29] Due the importance of aryl amines and related C-N bonds, synthetic chemists have developed a plethora of reactions over time to meet demand.[30] Reactions such as nucleophilic aromatic substitution, Ullmann Coupling, and the Chan-Lam Coupling have been extensively studied and applied to the formation of C-N bonds but possess their own set of limitations including the need of directing groups, harsh reagents, high temperatures, and the use of copper in either stoichiometric or catalytic amounts. These requirements can limit the substrate scope and opportunities to introduce

chemically labile substituents early on in a chemical synthesis. **Figure 1** exhibits the most common methods for aryl C-N bond formation.

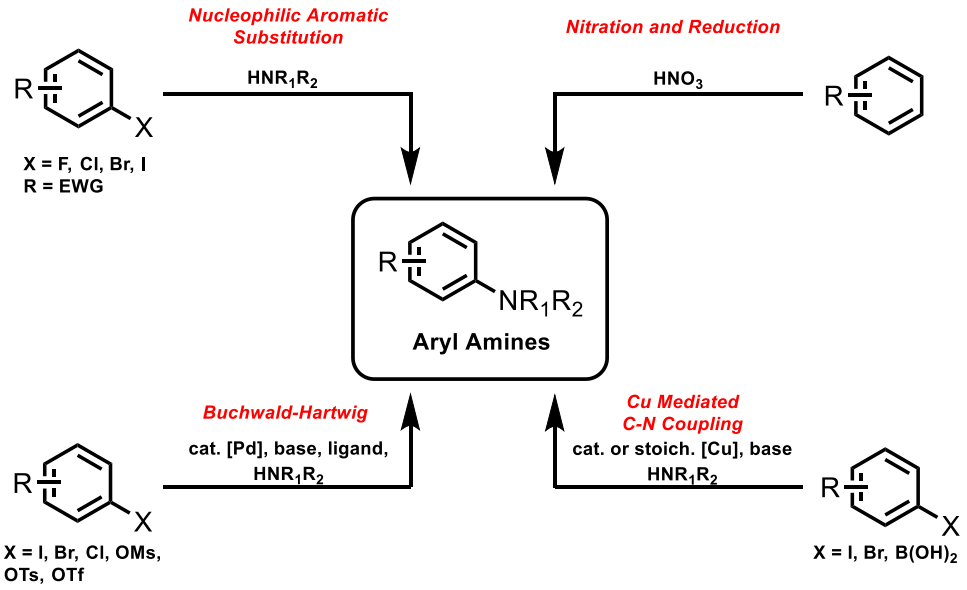

Figure 1. Overview of standard methods for aryl C-N bond formation.

A revolutionary development of C-N bond formation was introduced with the Buchwald-Hartwig amination.[28,29] This reaction has set a new precedent in C-N bond formation resulting in 10% of all recent medicinal chemistry publications utilizing the reaction at least once.[31] Not only does the palladium-catalyzed cross-coupling allow a broad range of usable aryl halide substrates, but also various nitrogen-containing nucleophiles including but not limited to amines, amides, sulfonamides, and ureas.[32] Coupling of the nitrogen-containing nucleophile and the aryl halide electrophile occurs at the C-X bond of the aryl halide where X = Cl, Br, or I. A distinct advantage is the usage of "pseudo" halides identified as mesylates, tosylates, triflates, and other sulfonyl esters. These pseudo halides allow for phenolic substrates to be activated and usable with Buchwald-Hartwig creating additional opportunity for synthetic strategy.

A key contributor to the success and selectivity of the Buchwald-Hartwig amination are the ancillary ligands.[32] Over the years many ancillary ligands have been developed consisting primarily of the biaryl monophosphine class, while others being phosphine-substituted ferrocenes and xanthene-based bis-phosphines. The catalytic cycle of the Buchwald-Hartwig amination (**Figure 2**) consists of three elementary steps. An oxidative addition step, followed by transmetalation comprising of nucleophile binding and deprotonation mediated by an organic or

inorganic base, and a reductive elimination step. Each step of the catalytic cycle is facilitated by the ancillary ligand hence the importance for the overall success of the reaction.

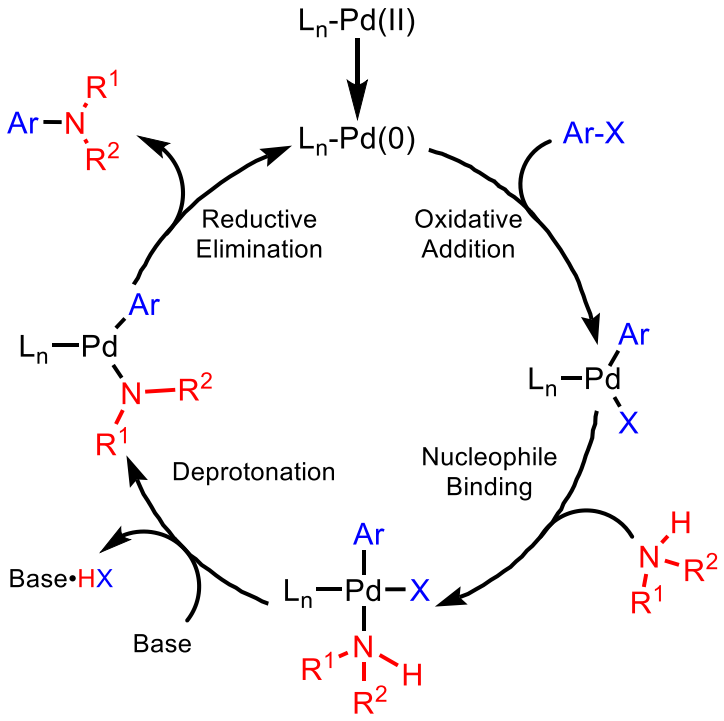

Figure 2. Catalytic cycle of the Buchwald-Hartwig amination.

1.3 References

(1) Krska, S. W.; DiRocco, D. A.; Dreher, S. D.; Shevlin, M. The Evolution of Chemical High-Throughput Experimentation To Address Challenging Problems in Pharmaceutical Synthesis. *Acc. Chem. Res.* **2017**, *50* (12), 2976–2985. https://doi.org/10.1021/acs.accounts.7b00428.

(2) Campos, K. R.; Coleman, P. J.; Alvarez, J. C.; Dreher, S. D.; Garbaccio, R. M.; Terrett, N. K.; Tillyer, R. D.; Truppo, M. D.; Parmee, E. R. The Importance of Synthetic Chemistry in the Pharmaceutical Industry. *Science* **2019**, *363* (6424), eaat0805. https://doi.org/10.1126/science.aat0805.

(3) Troshin, K.; Hartwig, J. F. Snap Deconvolution: An Informatics Approach to High-Throughput Discovery of Catalytic Reactions. *Science* **2017**, *357* (6347), 175–181.https://doi.org/10.1126/science.aan1568.

(4) Buitrago Santanilla, A.; Regalado, E. L.; Pereira, T.; Shevlin, M.; Bateman, K.; Campeau, L.-C.; Schneeweis, J.; Berritt, S.; Shi, Z.-C.; Nantermet, P.; Liu, Y.; Helmy, R.; Welch, C. J.; Vachal, P.; Davies, I. W.; Cernak, T.; Dreher, S. D. Nanomole-Scale High-Throughput Chemistry for the Synthesis of Complex Molecules. *Science* **2015**, *347* (6217), 49–53. https://doi.org/10.1126/science.1259203.

(5) Shevlin, M. Practical High-Throughput Experimentation for Chemists. *ACS Med. Chem. Lett.* **2017**, *8* (6), 601–607. https://doi.org/10.1021/acsmedchemlett.7b00165.

(6) Granda, J. M.; Donina, L.; Dragone, V.; Long, D.-L.; Cronin, L. Controlling an Organic Synthesis Robot with Machine Learning to Search for New Reactivity. *Nature* **2018**, *559* (7714), 377–381. https://doi.org/10.1038/s41586-018-0307-8.

(7) Eyke, N. S.; Koscher, B. A.; Jensen, K. F. Toward Machine Learning-Enhanced High-Throughput Experimentation. *Trends Chem.* **2021**, *3* (2), 120–132. https://doi.org/10.1016/j.trechm.2020.12.001.

(8) Nunn, C.; DiPietro, A.; Hodnett, N.; Sun, P.; Wells, K. M. High-Throughput Automated Design of Experiment (DoE) and Kinetic Modeling to Aid in Process Development of an API. *Org. Process Res. Dev.* **2018**, *22* (1), 54–61. https://doi.org/10.1021/acs.oprd.7b00295.

(9) Biyani, S. A.; Qi, Q.; Wu, J.; Moriuchi, Y.; Larocque, E. A.; Sintim, H. O.; Thompson, D. H. Use of High-Throughput Tools for Telescoped Continuous Flow Synthesis of an Alkynylnaphthyridine Anticancer Agent, HSN608. *Org. Process Res. Dev.* **2020**, *24* (10), 2240–2251. https://doi.org/10.1021/acs.oprd.0c00289.

(10) Murbach-Oliveira, G.; Banerjee, K.; Nociari, M. M.; Thompson, D. H. Continuous Flow Synthesis of A2E Guided by Design of Experiments and High-Throughput Studies. *ACS Bio Med Chem Au* **2022**. https://doi.org/10.1021/acsbiomedchemau.1c00060.

(11) Grainger, R.; Whibley, S. A Perspective on the Analytical Challenges Encountered in High-Throughput Experimentation. *Org. Process Res. Dev.* **2021**, *25* (3), 354–364. https://doi.org/10.1021/acs.oprd.0c00463.

(12) Welch, C. J. High Throughput Analysis Enables High Throughput Experimentation in Pharmaceutical Process Research. *React. Chem. Eng.* **2019**, *4* (11), 1895–1911. https://doi.org/10.1039/C9RE00234K.

(13) Mennen, S. M.; Alhambra, C.; Allen, C. L.; Barberis, M.; Berritt, S.; Brandt, T. A.; Campbell, A. D.; Castañón, J.; Cherney, A. H.; Christensen, M.; Damon, D. B.; Eugenio de Diego, J.; García-Cerrada, S.; García-Losada, P.; Haro, R.; Janey, J.; Leitch, D. C.; Li, L.; Liu, F.; Lobben, P. C.; MacMillan, D. W. C.; Magano, J.; McInturff, E.; Monfette, S.; Post, R. J.; Schultz, D.; Sitter, B. J.; Stevens, J. M.; Strambeanu, I. I.; Twilton, J.; Wang, K.; Zajac, M. A. The Evolution of High-Throughput Experimentation in Pharmaceutical Development and Perspectives on the Future. *Org. Process Res. Dev.* **2019**, *23* (6), 1213–1242. https://doi.org/10.1021/acs.oprd.9b00140.

(14) Maier, W. F. Early Years of High-Throughput Experimentation and Combinatorial Approaches in Catalysis and Materials Science. *ACS Comb. Sci.* **2019**, *21* (6), 437–444. https://doi.org/10.1021/acscombsci.8b00189.

(15) Lipinski, C. A.; Lombardo, F.; Dominy, B. W.; Feeney, P. J. Experimental and Computational Approaches to Estimate Solubility and Permeability in Drug Discovery and Development Settings1PII of Original Article: S0169-409X(96)00423-1. The Article Was Originally Published in Advanced Drug Delivery Reviews 23 (1997) 3–25.1. *Adv. Drug Deliv. Rev.* **2001**, *46* (1), 3–26. https://doi.org/10.1016/S0169-409X(00)00129-0.

(16) Vries, J. G. de; Vries, A. H. M. de. The Power of High-Throughput Experimentation in Homogeneous Catalysis Research for Fine Chemicals. *Eur. J. Org. Chem.* **2003**, *2003* (5), 799–811. https://doi.org/10.1002/ejoc.200390122.

(17) Lindsey, J. S. A Retrospective on the Automation of Laboratory Synthetic Chemistry. *Chemom. Intell. Lab. Syst.* **1992**, *17* (1), 15–45. https://doi.org/10.1016/0169-7439(92)90025-B.

(18) Cawse, J. N. Experimental Strategies for Combinatorial and High-Throughput Materials Development. *Acc. Chem. Res.* **2001**, *34* (3), 213–221. https://doi.org/10.1021/ar000117s.

(19) Upadhya, R.; Kosuri, S.; Tamasi, M.; Meyer, T. A.; Atta, S.; Webb, M. A.; Gormley, A. J. Automation and Data-Driven Design of Polymer Therapeutics. *Adv. Drug Deliv. Rev.* **2021**, *171*, 1–28. https://doi.org/10.1016/j.addr.2020.11.009.

(20) Williams, T.; McCullough, K.; Lauterbach, J. A. Enabling Catalyst Discovery through Machine Learning and High-Throughput Experimentation. *Chem. Mater.* **2020**, *32* (1), 157–165. https://doi.org/10.1021/acs.chemmater.9b03043.

(21) Biyani, S. A.; Moriuchi, Y. W.; Thompson, D. H. Advancement in Organic Synthesis Through High Throughput Experimentation. *Chemistry–Methods* **2021**, *1* (7), 323–339. https://doi.org/10.1002/cmtd.202100023.

(22) Sather, A. C.; Martinot, T. A. Data-Rich Experimentation Enables Palladium-Catalyzed Couplings of Piperidines and Five-Membered (Hetero)Aromatic Electrophiles. *Org. Process Res. Dev.* **2019**, *23* (8), 1725–1739. https://doi.org/10.1021/acs.oprd.9b00233.

(23) Hayhow, T. G.; Borrows, R. E. A.; Diène, C. R.; Fairley, G.; Fallan, C.; Fillery, S. M.; Scott, J. S.; Watson, D. W. A Buchwald–Hartwig Protocol to Enable Rapid Linker Exploration of Cereblon E3-Ligase PROTACs. *Chem. – Eur. J.* **2020**, *26* (70), 16818–16823. https://doi.org/10.1002/chem.202003137.

(24) Jaman, Z.; Logsdon, D. L.; Szilágyi, B.; Sobreira, T. J. P.; Aremu, D.; Avramova, L.; Cooks, R. G.; Thompson, D. H. High-Throughput Experimentation and Continuous Flow Evaluation of Nucleophilic Aromatic Substitution Reactions. *ACS Comb. Sci.* **2020**, *22* (4), 184–196. https://doi.org/10.1021/acscombsci.9b00212.

(25) Chow, S. Y.; Nelson, A. Embarking on a Chemical Space Odyssey. *J. Med. Chem.* **2017**, *60* (9), 3591–3593. https://doi.org/10.1021/acs.jmedchem.7b00423.

(26) Cernak, T.; Gesmundo, N. J.; Dykstra, K.; Yu, Y.; Wu, Z.; Shi, Z.-C.; Vachal, P.; Sperbeck, D.; He, S.; Murphy, B. A.; Sonatore, L.; Williams, S.; Madeira, M.; Verras, A.; Reiter, M.; Lee, C. H.; Cuff, J.; Sherer, E. C.; Kuethe, J.; Goble, S.; Perrotto, N.; Pinto, S.; Shen, D.-M.; Nargund, R.; Balkovec, J.; DeVita, R. J.; Dreher, S. D. Microscale High-Throughput Experimentation as an Enabling Technology in Drug Discovery: Application in the Discovery of (Piperidinyl)Pyridinyl-1H-Benzimidazole Diacylglycerol Acyltransferase 1 Inhibitors. *J. Med. Chem.* **2017**, *60* (9), 3594–3605. https://doi.org/10.1021/acs.jmedchem.6b01543.

(27) Carter, H. L.; Connor, A. W.; Hart, R.; McCabe, J.; McIntyre, A. C.; McMillan, A. E.; Monks, N. R.; Mullen, A. K.; Ronson, T. O.; Steven, A.; Tomasi, S.; Yates, S. D. Rapid Route Design of AZD7594. *React. Chem. Eng.* **2019**, *4* (9), 1658–1673. https://doi.org/10.1039/C9RE00118B.

(28) Ruiz-Castillo, P.; Buchwald, S. L. Applications of Palladium-Catalyzed C–N Cross-Coupling Reactions. *Chem. Rev.* **2016**, *116* (19), 12564–12649. https://doi.org/10.1021/acs.chemrev.6b00512.

(29) Ma, D.; Zhai, S.; Wang, Y.; Liu, A.; Chen, C. Synthetic Approaches for C-N Bonds by TiO2 Photocatalysis. *Front. Chem.* **2019**, *7*.

(30) Forero-Cortés, P. A.; Haydl, A. M. The 25th Anniversary of the Buchwald–Hartwig Amination: Development, Applications, and Outlook. *Org. Process Res. Dev.* **2019**, *23* (8), 1478–1483. https://doi.org/10.1021/acs.oprd.9b00161.

(31) Brown, D. G.; Boström, J. Analysis of Past and Present Synthetic Methodologies on Medicinal Chemistry: Where Have All the New Reactions Gone? *J. Med. Chem.* **2016**, *59* (10), 4443–4458. https://doi.org/10.1021/acs.jmedchem.5b01409.

(32) Ingoglia, B. T.; Wagen, C. C.; Buchwald, S. L. Biaryl Monophosphine Ligands in Palladium-Catalyzed C–N Coupling: An Updated User's Guide. *Tetrahedron* **2019**, *75* (32), 4199–4211. https://doi.org/10.1016/j.tet.2019.05.003.

CHAPTER 2. HIGH THROUGHPUT EXPERIMENTATION CAMPAIGN OF THE BUCHWALD-HARTWIG AMINATION TO INVESTIGATE SUBSTRATE COMPATIBILITY

2.1 Introduction

Considering how impactful and necessary the Buchwald-Hartwig amination is to aryl C-N bond formation, we set out to investigate the implications of the important reaction components. The effect of the ancillary ligand on substrate coupling ability, catalyst/ligand loadings, starting material stoichiometries, and temperature were to be investigated using HTE as the supporting tool. Substrates chosen contained 32 aryl(pseudo) halides (**Figure 3**) of the heterocyclic, electron-donating substituted, and electron withdrawing substituted class of arenes, along with 24 nitrogen-containing nucleophiles (**Figure 4**) to create 768 unique reaction combinations. Of the ancillary ligands tested, 10 were of the biaryl monophosphine class and the final was a xanthene-based bis phosphine (XantPhos). **Figure 5** shows the structures of these ancillary ligands. The goal for the data acquired from this study can be extrapolated and used by synthetic chemists to guide their choice of reagent and condition selection when opting to perform the Buchwald-Hartwig amination. Having 8,448 unique reaction conditions, and 768 unique microdroplet reactions is a good starting point for a Buchwald-Hartwig data library that can be applied to machine learning algorithms.

To begin the HTE campaign, batch experiments of the Buchwald-Hartwig amination were performed on a set of relatively simple substates to establish a positive control. This created a validated starting point to perform high throughput experiments knowing at least the investigated batch reaction and will proceed. **Scheme 1** outlines the selected substrates being coupled in high yields.

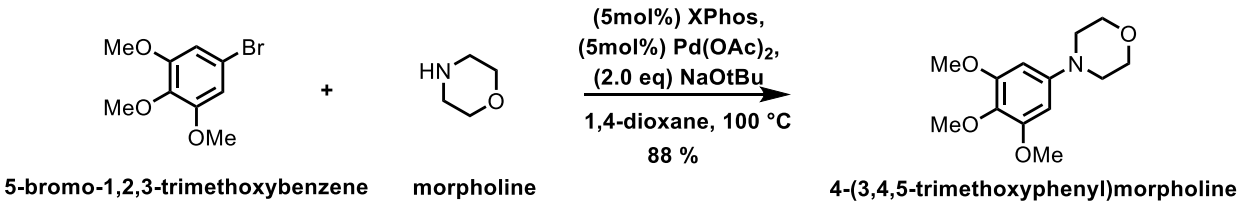

Scheme 1. Reaction scheme of chosen batch reaction to optimize as a positive control for HTE.

It was found in a previous study that the order of addition for reagents was vital to the success in palladium catalyzed cross coupling reactions, specifically in the realm of HTE.[1] With this knowledge in-hand, a high throughput experiment was designed to help us determine the best order of addition. This would be applied to the broad substate scope screen to help reduce reaction inefficiency across the board of substrates.

With the chosen order of addition, the main substate screening was able to be pursued. Each ligand was tested against the 768 unique substrate combinations and analyzed via DESI-MS. Heat maps were generated to help visualize what reactions were “hits” and what were “misses”. Signal-to-noise ratios (S/N) were used for each m/z of the reactions to determine whether the reaction was successful or not. Furthermore, select samples were made from the HTE reaction solutions to be tested via LC-MS for the sake of validating what the lower threshold was for signal-to-noise ratios to be considered hits or misses.

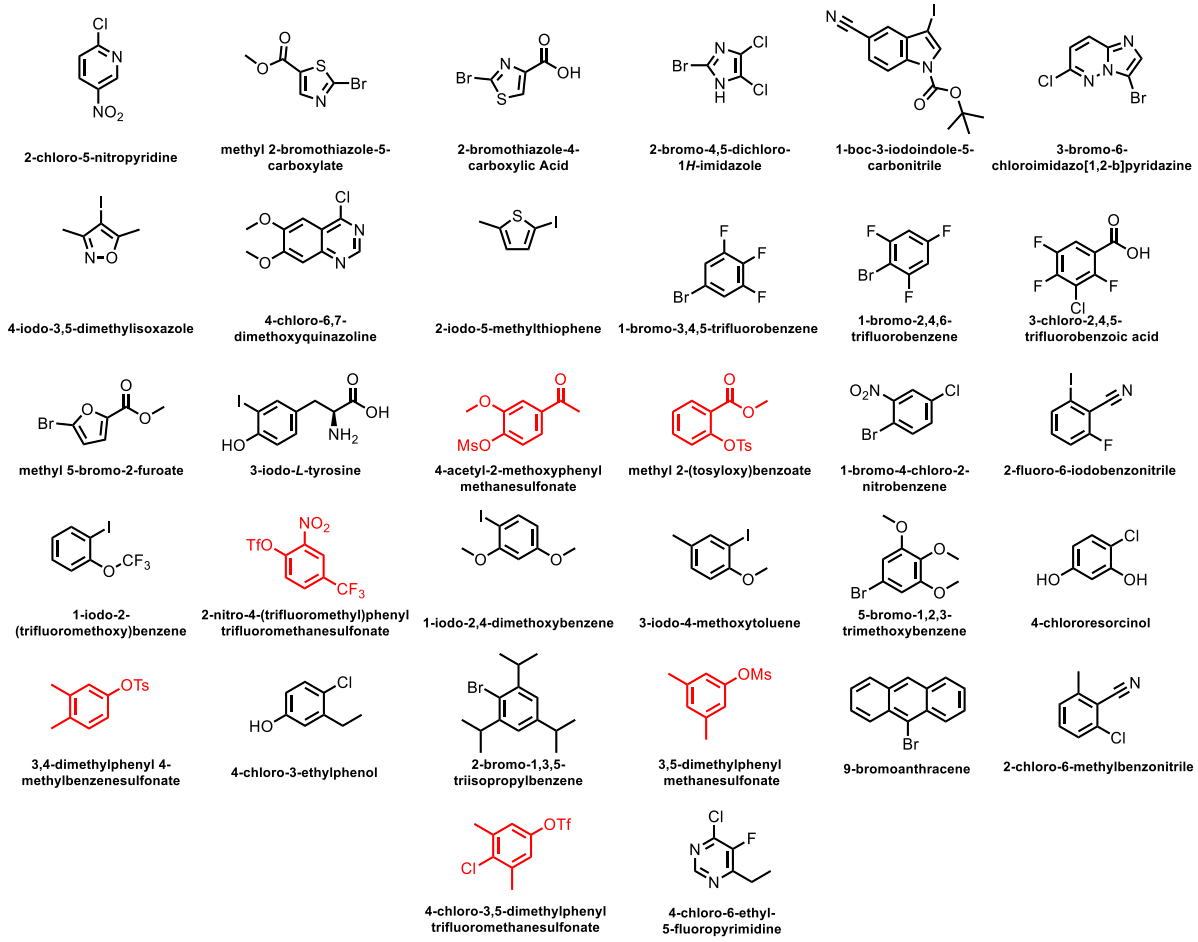

Figure 3. Structures of aryl and aryl(pseudo) halides used in the HTE campaign. Structures in red were purchased in the phenolic form and converted to the respecting sulfonyl ester.

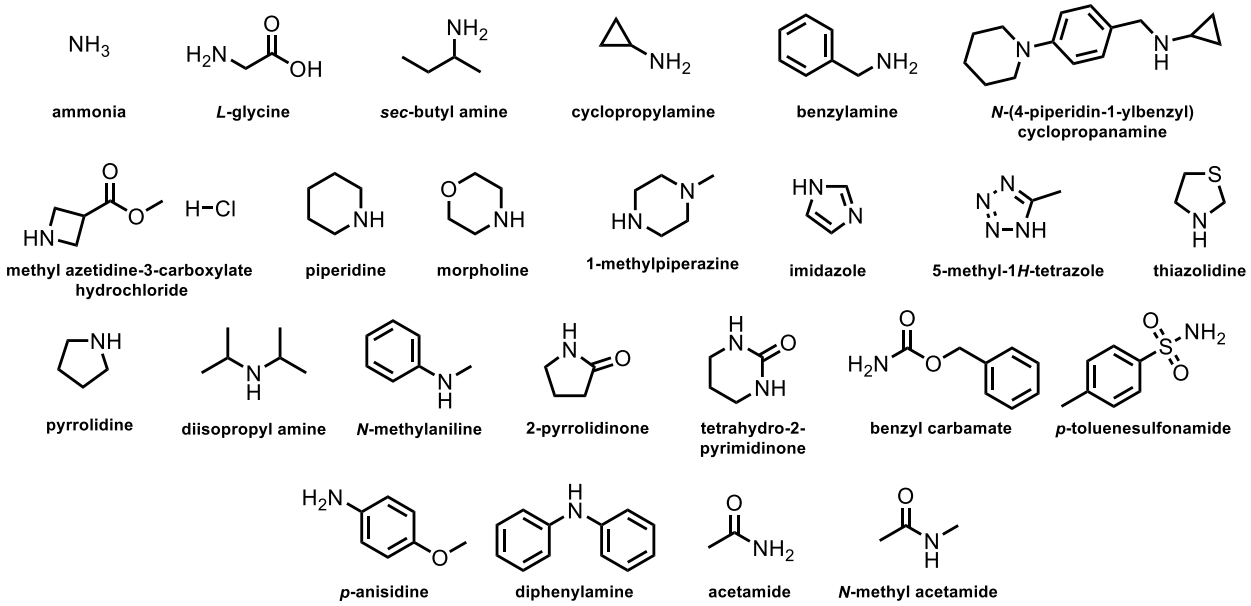

Figure 4. Structures of the 24 nitrogen-containing nucleophiles used in the HTE campaign.

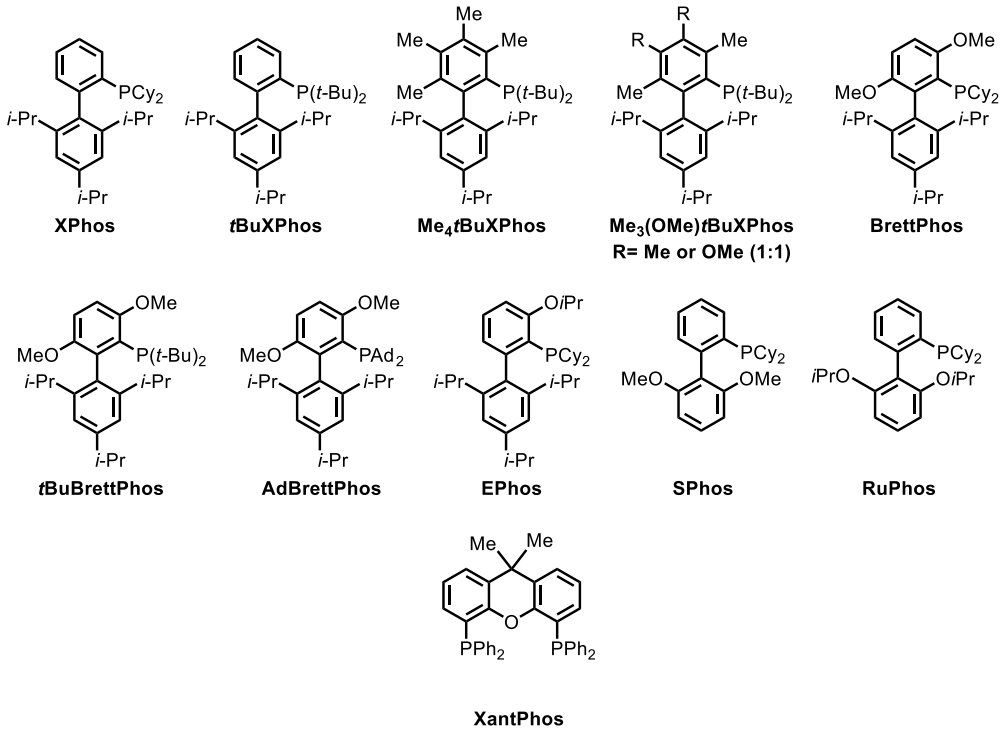

Figure 5. Structures of the 10 biaryl monophosphine ligands and xanthene based bis-phosphine.

2.2 Methods

To carry out this research, a system developed in collaboration with others[2] utilizing a Beckman Coulter i7 liquid handling robot (**Figure 6**) was used to perform the microdroplet reactions which were assayed for their efficiency and outcome via DESI-MS. The i7 liquid handing robot used in the HTE system utilized 96-well aluminum heating blocks (Analytical Sales) that hold 1 mL glass vial inserts. The heating blocks have a septum-sealed lid that ultimately produces 96 individual bomb reactors. Pipetting methods are given to the liquid handling robot in which solutions are aspirated and dispensed into the respective vials. After solutions are dispensed, the lid can be placed on the heating block and then heated with a Peltier heater (**Figure 7**). If the reactions don't require heating, or a room temperature aliquot is needed, a pipetting method can transfer 60 µL from each 1 mL vial to a 384-well plate. If the reactions require heating, upon completion the lid is removed from the heating block and the same pipetting method is used to transfer 60 µL of the reaction to the 384-well plate for analysis. Typical reaction volumes in the 96-well heating blocks were 250 µL, with final substrate concentrations at 30 mM.

Analysis of the HTE by DESI-MS was performed by taking a 384-well plate containing the aliquots from the 96-well heating block and dipping a 384-pin tool into the wells. The liquid handling robot has a method that uses this pin tool to take 50 nL from each well of the 384-well plate and stamps the pins onto a glass plate covered with a PTFE film. This plate is then placed on the stage of the DESI-MS instrument where the stage moves in a serpentine motion to analyze each reaction spot. The data acquisition for DESI-MS was performed using a linear ion trap mass spectrometer (LTQ, Thermo Scientific) fitted with a DESI stage that is commercially available (2D Prosolia DESI stage, Waters Corporation). A nebulized spray of nitrogen gas and 10% acetonitrile in methanol at a flow rate of 2.75 µL/min is used to desorb each reaction spot where any desorbed material is taken in the MS inlet for analysis. The spray solvent was spiked with 0.1% formic acid for positive ion analysis. No formic acid was added for negative ion analysis. In a reproducible manner, 1,536 reaction spots can be assayed in a matter of 34 minutes. MS/MS capability is another feature than can be employed if necessary. Proprietary CHRIS software can then take the raw data from assaying the DESI plate and search for m/z values set by the user. CHRIS then outputs spreadsheets containing ion counts for all m/z values given by the user to be observed.

Reagents were purchased from MilliporeSigma, TCI, and Acros Organics. Solvents used were all of HPLC grade unless noted.

Analysis of LC-MS samples was performed using a Thermo Fisher TSQ Quantum Access MAX mass spectrometer connected with a Dionex Ultimate 3000 Series Binary Pump (UPLC) and an WPS-3000 autosampler (Thermo Fisher Scientific, Waltham, MA). An Agilent XDB C18 column (5 µm particle size, 4.6 x 150 mm) with an injection volume 5 µL was used. UPLC gradients were 10-100% methanol in aqueous buffer over a time of 15 minutes.

^{1}H NMR spectra were obtained using a Bruker Avance III-HD (500 MHz) instrument. Chemical shifts are reported using the residual solvent peak as reference.

Figure 6. Beckman Coulter i7 liquid handling robot used for the HTE campaign.

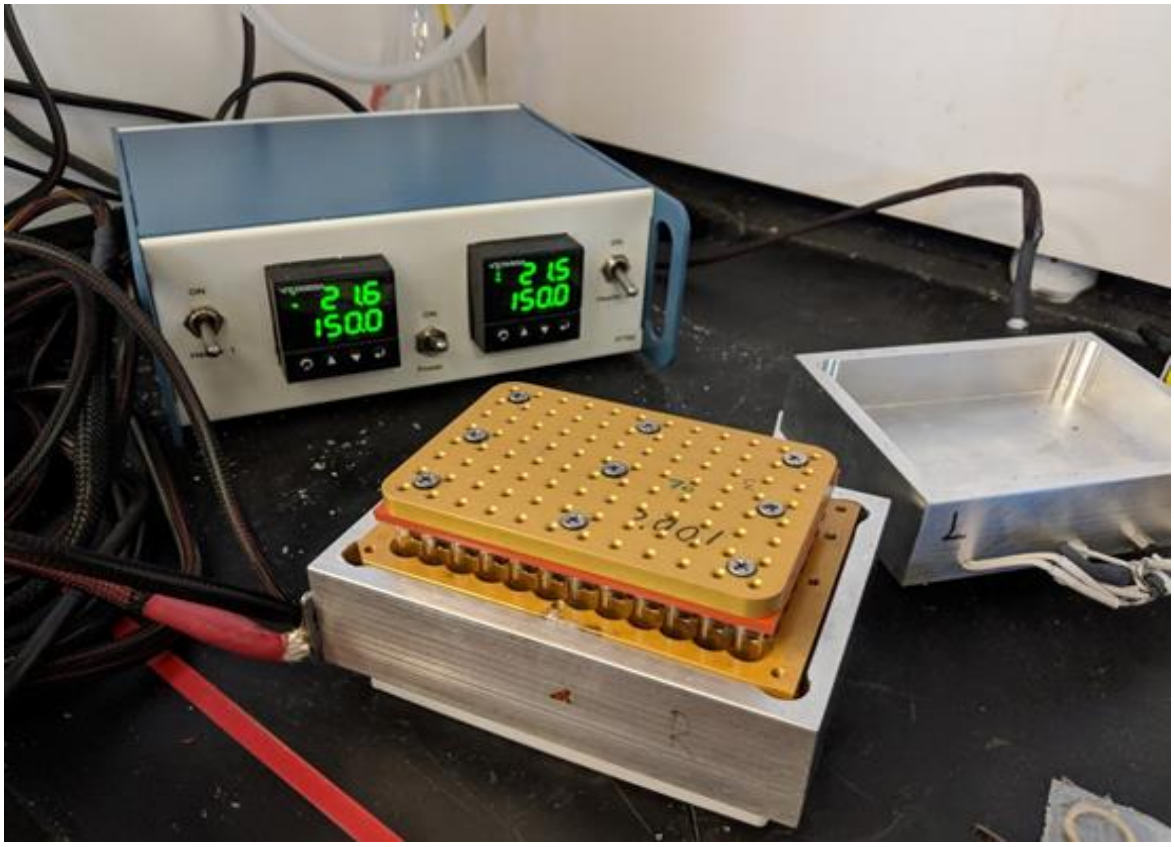

Figure 7. 96-well aluminum heating block inside the Peltier heater.

2.2.1 Order of Addition Experiment

Using the optimized batch reaction from **Scheme 1**, a high throughput experiment was devised to investigate reaction time, temperature, stoichiometries, and ultimately the order of the reagent additions. Orders tested included the order used in the batch validation experiment and 8 different addition orders. Every reaction in the order of addition HTE used morpholine and 5-bromo-1,2,3-trimethoxybenzene as the substates. **Tables 1** and **2** outline the various reagent orders, and the reaction conditions tested in the order of addition HTE. The aryl halide (ArX) was treated as the limiting reagent at 1 eq. Each individual reaction parameter was tested against all other variable in each parameter. 1,4-Dioxane was used as the reaction solvent. Heating blocks used in the i7 had lids placed on top to seal each reaction vessel to prevent solvent evaporation while heating. Each reaction in the HTE was 400 µL to allow for multiple aliquots to be taken for analysis at the different time points. Final concentration of the ArX starting material after addition of all reaction components was 30 mM in each vial. This was to help reduce issues related to signal strength in subsequent DESI-MS analysis. Comparison of product ion counts from the mass spectrometer was used to determine which reaction conditions and reagent addition order was optimal.

Table 1. Overview of the different reagent addition orders investigated in the HTE.

Order of Addition Notation	Reagent Order
O1 (+ control)	ArX, nucleophile, ligand, catalyst, base
O2	ArX, nucleophile, *no ligand*, catalyst, base
O3	nucleophile, base, ligand, catalyst, ArX
O4	catalyst, ArX, base, ligand, nucleophile
O5	catalyst, ArX, base, nucleophile, ligand
O6	ligand, catalyst, nucleophile, base, ArX
O7	base, nucleophile, ArX, catalyst, ligand
O8	base, ArX, catalyst, ligand, nucleophile

Table 2. Overview of the different reactions condition parameters investigated during the order of addition HTE. Each column represents the different values tested within that parameter. Rows do not indicate dependance.

	Time (h)	Temp (°C)	Base (eq)	Pd (mol%)	Ligand (mol%)	Nucleophile
Conditions	1	RT	1	1	1	1
	2	60	1.5	2.5	2.5	1.5
	3	100	2	5	5	2
	4	140		10	10	

2.2.2 LC-MS Validation of Signal-to-Noise Thresholds for HTE

Representation of the data for the upcoming broad substrate scope HTE is in the form of a heat map exemplified by the signal to noise values (S/N) at each intersection of nucleophile and aryl halide. The details of how these experiments were performed will be in the next section, but in order to understand how S/N ratio thresholds were set to determine whether a reaction was a hit or miss, the LC-MS experiment to validate thresholds must be elaborated. The S/N values were calculated by dividing the observed product ion count for each reaction's respective product m/z value by a blank value which was acquired by the DESI-MS scanning a non-spotted area of the DESI plate for the respective m/z. To determine what a "hit" and "miss" were, a LC-MS experiment was carried out. From a single broad substate scope HTE (tBuXPhos), 28 LC-MS samples were made with the same concentration. Out of the 768 reactions for each experiment, the 28 were chosen by picking S/N values from 1-15 in ascending order to refine the threshold where a certain S/N was considered a hit or miss. After S/N of 15, the reactions chosen for analysis were ones that gradually increased in S/N until a maximum value of 1852 was reached. Each sample was analyzed in LC-MS use both polarities. To ensure the mobile phase buffer wasn't skewing results, both 0.1% formic acid in water and 0.01 M ammonium acetate in water were used.

2.2.3 Broad Substrate Scope HTE

After finding an optimal order of addition for reagents, including information on temperature, time, and stoichiometry, this information was translated to the development of a HTE to investigate substrate compatibility with different commercially available ancillary ligands (**Figure 5**). The HTE campaign was set to have 11 individual experiments in which each

experiment only uses 1 ligand for the 768 reaction combinations. Of the ligands used, 10 were of the biaryl monophosphine class, while the final was the xanthene-based bis phosphine ligand. Nucleophiles were chosen based on the variance of nucleophilicity, substitution degree, and steric properties. Aryl halides and pseudo halides were chosen based on their heterocyclic character, electron richness/deficiency, steric properties, and the presence of notably labile substituents known to be troublesome in palladium cross-coupling reactions. The pseudo halides screened in the experiments were synthesized from their commercially availability phenolic forms and their experimentals can be found in the **supplementary information**. Catalyst and ligand loadings, stoichiometry, temperature, and base were all kept constant. Each experiment was also performed at room temperature and at an elevated temperature of 100 °C. 1,4-Dioxane was the primary solvent as most of the substrates and reagents were soluble. Notable exceptions were the NaOtBu where optimal solubility and pipetting efficiency was found to be 40% 1,4-Dioxane in tBuOH, and substates such as glycine where water was necessary to dissolve the substrate. Substates that required different solvent systems other than 1,4-dioxane will be noted accordingly in the data sets. Success of coupling glycine and other substrates in aqueous conditions has other implications as it is a general rule that water must be kept away from Pd catalyzed cross-couplings. Although aqueous Buchwald-Hartwig has been performed[3-4], investigating the scope and efficiency is an intriguing thought. The order of addition HTE led us to use 1 eq of ArX, 1.5 eq of the nucleophile, 2 eq of base (NaO*t*Bu), and 5 mol% of both Pd catalyst and ancillary ligand. Each experiment was allowed to react for 2 h before analysis via DESI-MS was performed. Each reaction in the HTE was 250 µL to allow for an aliquot to be taken for analysis at room temperature and after heating. Solutions of the ArX and nucleophiles were prepared and stored in -80 °C for use in 3 experiments before fresh solutions were made. Since only 4 Peltier heaters were available, and 8 96-well heating blocks were required for each experiment, half of the experiment was pipetted and heated for 2 h. Once the first half of the experiment was finished reacting, it was pinned on the PTFE DESI plates and analyzed while the second half off the experiment was pipetted and heated. Once the second half was completed, it was subsequently analyzed with DESI-MS ultimately completing the 768-reaction high throughput experiment. Aliquots of each reaction from the experiment were stored in 384-well plates and stored in a -80 °C freezer in case the experiment needed to be re-analyzed, MS/MS needed to be performed, or individual reactions needs to be analyzed with LC-MS.

2.3 Results and Discussion

2.3.1 Order of Addition Experiment

Performing the order of addition HTE gave valuable insight on the proper order to add reagents, along with the time, temperature, and stoichiometries best suited for the transformation in **Scheme 1.** It was found that order "O3" (nucleophile, base, ligand, catalyst, ArX) in **Table 1** gave the best results. This is different from the order established in the initial batch experiment; a testament to the strength of HTE as a tool for reaction optimization. In terms of stoichiometry, it was determined to use 2 eq of NaO*t*Bu, 1.5 eq of nucleophile, and 5 mol % of both Pd catalyst and ligand. ArX was set as the limiting reagent (1 eq). Since these conditions were going to be applied to over 8,000 reactions and 768 unique substate combinations, we sought to find the most general conditions to apply keeping in mind that the conditions may not be optimal for other substrate combinations. One of the contrast plots used to visualize the data from the order of addition HTE is shown in **Figure 8**.

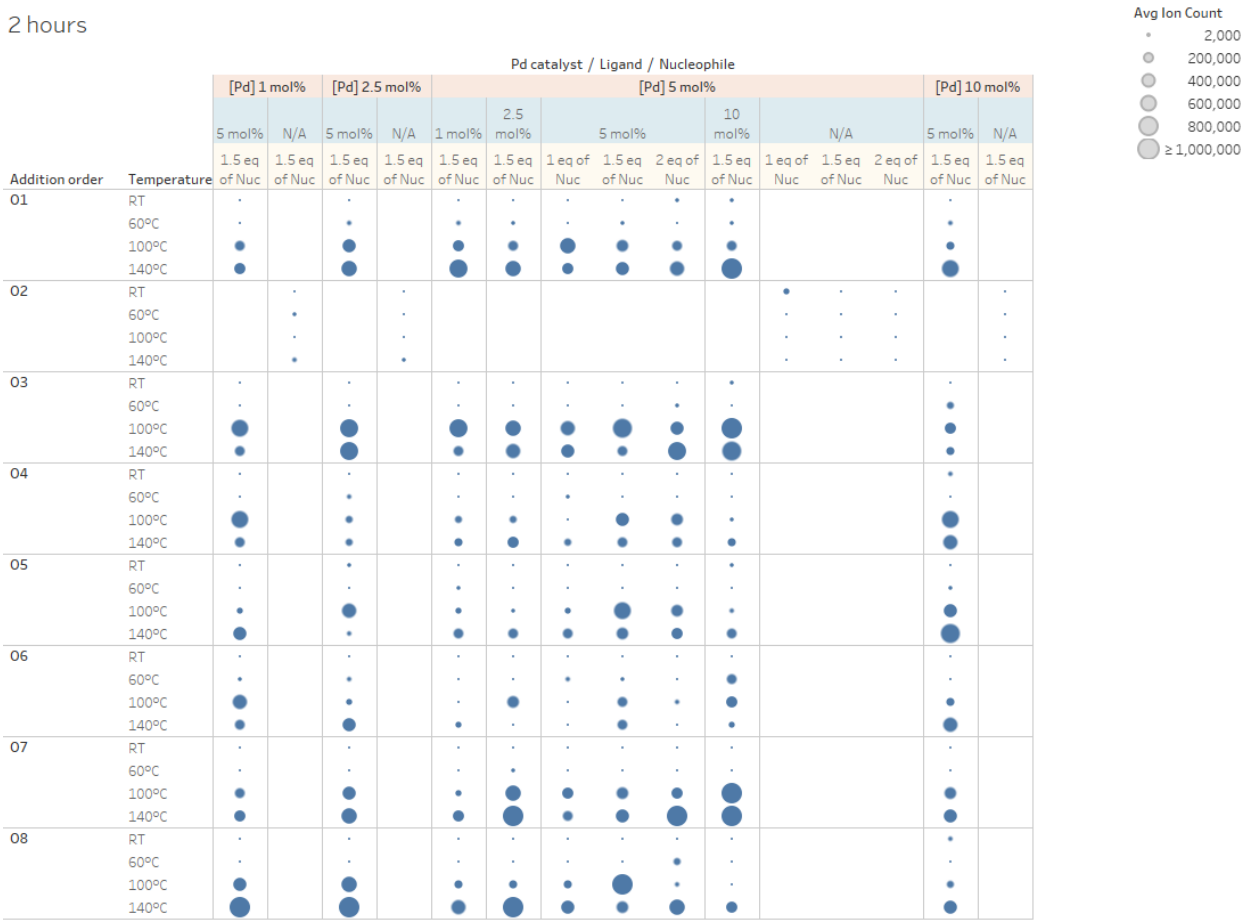

Figure 8. Contrast plot from the order of addition HTE of the data at the 2 h mark. The larger the dot at the intersection of condition labels, the greater the product ion count from observed in DESI-MS.

Data for 1, 3, and 4 h represented in the form of contrast plots is shown in the **supplementary information**. It is thought that the chosen order of addition performed the best across various stoichiometries and other parameters because it may prevent aryl homo-coupling, and also allows the palladium to precomplex with the ancillary ligand accordingly before the ArX is introduced to facilitate oxidative addition.

2.3.2 LC-MS Validation of Signal-to-Noise Thresholds for HTE

Using the HTE from the broad substrate scope screen with *t*BuXPhos as the ligand, 28 specific reactions within the HTE were chosen by picking S/N values from 1-15 in ascending order to refine the threshold where a certain S/N was considered a hit or miss. After S/N of 15, the reactions chosen for analysis were ones that gradually increased in S/N until a maximum value of 1852 was reached. In LC-MS, if the respective m/z of the product was observed above the

instrument's limit of detection in either positive or negative mode, it was deemed that product existed and therefore the HTE reaction was a "hit". Using this methodology, hits in LC-MS were compared to the S/N values given by DESI-MS in positive and negative modes to determine a minimum threshold that is considered a hit in DESI-MS data. Using this methodology and means of interpretation, highly efficient reactions observed in HTE are to exhibit much higher S/N values than the minimum threshold. **Table 3** outlines the data acquired from the LC-MS investigation. Data from LC-MS and DESI-MS was considered to agree with each other when the product of a particular transformation was observed within the limit of detection of the LC-MS and also observed in the DESI-MS spectrum. If LC-MS analysis showed evidence of product, but not DESI-MS analysis, it was considered that for the specific reaction DESI-MS gave a false-positive result. Oppositely, if LC-MS analysis showed evidence of product but not DESI-MS analysis it was considered a false-negative.

Table 3. Results from LC-MS S/N validation study. The S/N values are the ones extrapolated through the DESI-MS data in both ion modes. FA = Formic acid buffer, AmAc = Ammonium acetate (0.01 M) buffer.

ArX	Nucleophile	S/N (+ion)	S/N (-ion)	Product LCMS-FA	Product LCMS-AmAc	DESI -MS
2-chloro-5-nitropyridine	2-pyrrolidinone	1	1	Y	N	N
1-boc-3-iodoindole-5-carbonitrile	*L*-glycine	1	1	N	N	N
methyl-2-bromothiazole-5-carboxylate	5-methyl-1*H*-tetrazole	2	2	N	N	N
4-chlororesorcinol	ammonia	2	2	N	N	N
1-boc-3-iodoindole-5-carbonitrile	*N*-methylaniline	3	3	N	N	N
3-bromo-6-chloroimidazo[1,2-b]pyridazine	2-pyrrolidinone	4	4	Y	Y	Y
3-iodo-*L*-tyrosine	morpholine	5	5	Y	Y	Y
2-chloro-6-methylbenzonitrile	*N*-(4-piperidin-1-yl)cyclopropanamine	1	7	N	N	Y

Table 3 continued

2-bromothiazole-4-carboxylic acid	*N*-methylpiperazine	6	8	Y	Y	Y
methyl-5-bromo-2-furoate	pyrrolidine	1	10	Y	Y	Y
1-bromo-2,4,6-trifluorobenzene	diisopropylamine	2	12	N	N	Y
4-chloro-6-ethyl-5-fluoropyrimidine	piperidine	14	6	Y	Y	Y
2-bromo-1,3,5-triisopropylbenzene	*N*-methylaniline	1	15	N	N	Y
3-chloro-2,4,5-trifluorobenzoic acid	benzylamine	17	6	Y	N	Y
5-bromo-1,2,3-trimethoxybenzene	diphenylamine	5	19	Y	Y	Y
1-bromo-2,4,6-trifluorobenzene	acetamide	21	5	N	N	Y
2-chloro-5-nitropyridine	tetrahydro-2-pyrimidinone	26	1	Y	Y	Y
4-chloro-6-ethyl-5-fluoropyrimidine	benzylamine	29	6	N	N	Y
3-iodo-4-methoxytoluene	*N*-(4-piperidin-1-yl)cyclopropanamine	34	1	Y	Y	Y
3,5-dimethylphenyl-mesylate	ammonia	2	36	Y	N	Y
4-chloro-6,7-dimethoxyquinazoline	thiazolidine	42	7	Y	Y	Y
4-chlororesorcinol	thiazolidine	2	49	N	N	Y
2-iodo-5-methylthiophene	cyclopropylamine	1	53	Y	N	Y
1-iodo-2-trifluoromethoxy-benzene	*p*-toluenesulfonamide	1	61	Y	Y	Y

Table 3 continued

1-bromo-4-chloro-2-nitrobenzene	*p*-toluenesulfonamide	1	74	N	Y	Y
4-chloro-6,7-dimethoxyquinazoline	cyclopropylamine	177	90	Y	Y	Y
methyl-5-bromo-2-furoate	imidazole	3	301	Y	N	Y
2-chloro-5-nitropyridine	*p*-toluenesulfonamide	2	1852	Y	Y	Y

After analysis, a low S/N threshold was set at 5, with 5 being the lowest S/N to be detected in LC-MS. All heat maps produced in the broad substrate scope HTE will use a S/N of 5. Additionally, after analysis it was found that DESI-MS was giving false-negatives 22% of the time, and false-positives 4% of the time. These statistical values align with what was found in a previous study using similar HTE methodology.[5]

2.3.3 Broad Substrate Scope HTE

Having proper reaction conditions from the order of addition HTE, and more insight on data analysis from the LC-MS validation experiment, the main HTE campaign to test the 768 unique reaction combinations against the 11 different ancillary ligands was performed. Palladium(II) Acetate was used as the catalyst and NaO*t*Bu was used as the base. Further experiments could be performed to gain more insight on the palladium catalyst choice and base, but that was outside the scope of this study. Palladium(II) acetate is relatively inexpensive, commercially available, air-stable, and widely used throughout the literature.

Trends seen through these experiments in terms of substate compatibility with respect to the ancillary ligand used gave a general idea of what substates can and cannot be used with a specific ligand. An example of the graphically represented data can be seen in **Figures 9-12** with both negative and positive ion heat maps using the *t*BuXPhos ligand after being heated at 100 °C and sitting at room temperature for 2 h. Many heat maps were produced from this experiment, and all can be viewed in the **supplemental information** section. Since there were many substates and respective products with different degrees of ionizability in the mass spectrometer, both ion modes

were used to assay each high throughput experiment. To briefly summarize the trends extrapolated through the experiment, **Table 4** outlines each ancillary ligand and the classes of nucleophile and ArX that were deemed compatible.

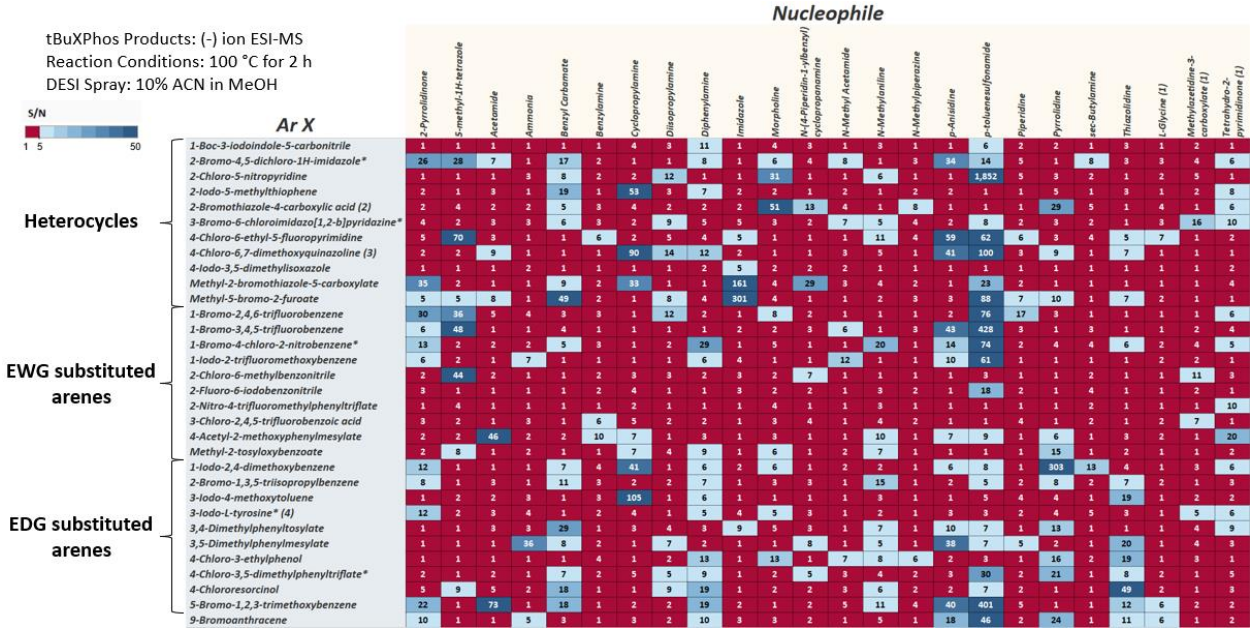

Figure 9. Negative ion heat map from the *t*BuXPhos experiment after being heated at 100 °C for 2 h. (1) is 50% *t*BuOH in H_2O. (2) is 30% 1,4-Dioxane in *t*BuOH. (3) is 10% *t*BuOH in PhMe. (4) is 20% *t*BuOH, 30% 1,4-Dioxane, 50% H_2O.

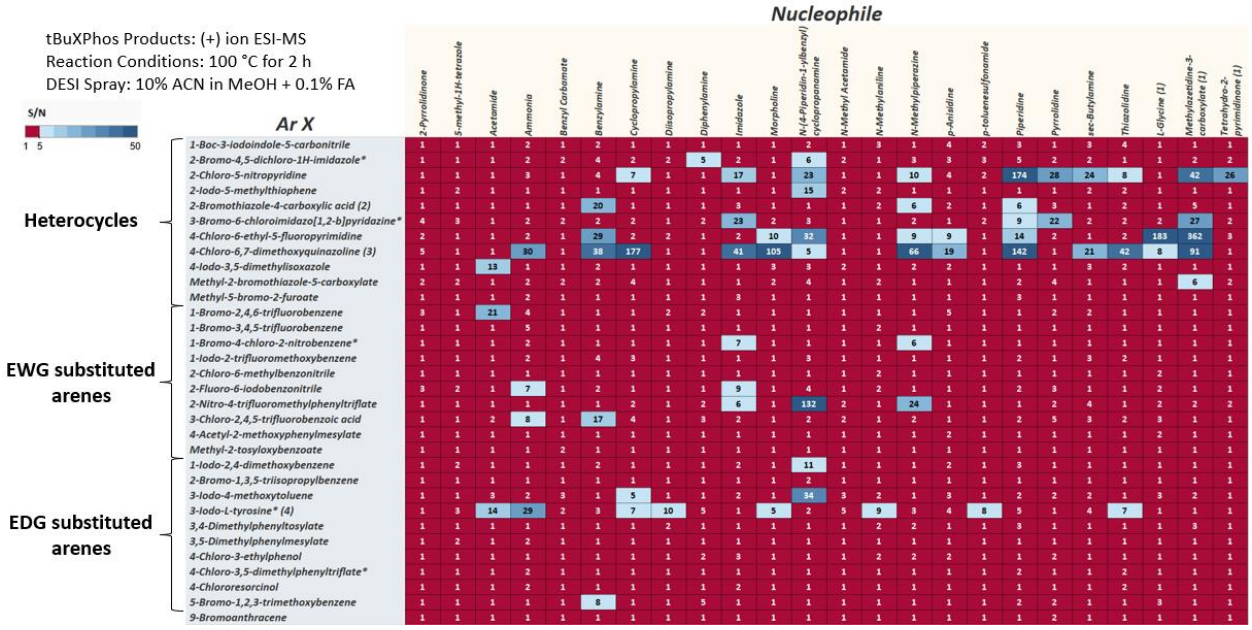

Figure 10. Positive ion heat map from the *t*BuXPhos experiment after being heated at 100 °C for 2 h. (1) is 50% *t*BuOH in H_2O. (2) is 30% 1,4-Dioxane in *t*BuOH. (3) is 10% *t*BuOH in PhMe. (4) is 20% *t*BuOH, 30% 1,4-Dioxane, 50% H_2O.

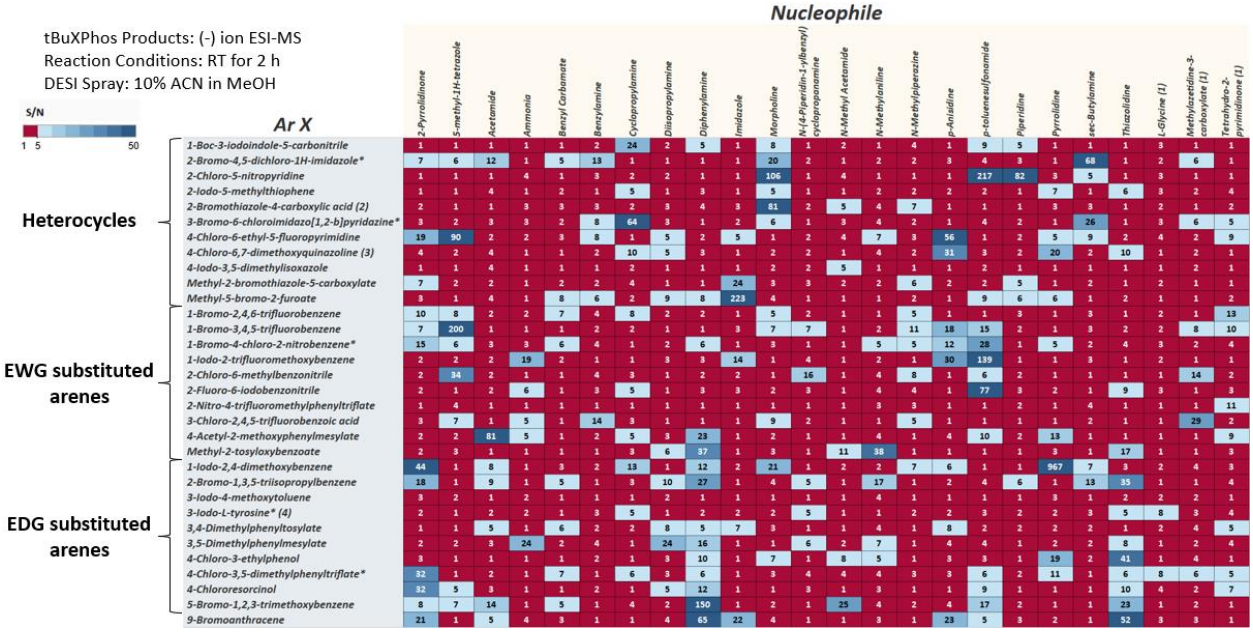

Figure 11. Negative ion heat map from the *t*BuXPhos experiment after sitting at RT for 2 h. (1) is 50% *t*BuOH in H_2O. (2) is 30% 1,4-Dioxane in *t*BuOH. (3) is 10% *t*BuOH in PhMe. (4) is 20% *t*BuOH, 30% 1,4-Dioxane, 50% H_2O.

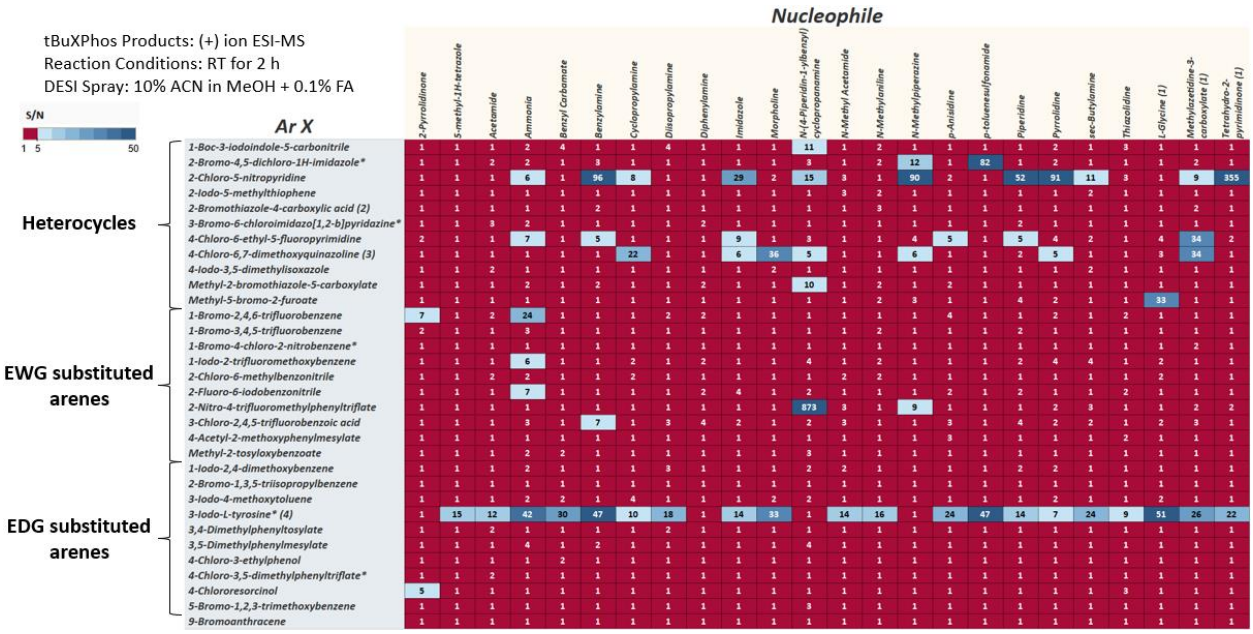

Figure 12. Positive ion heat map from the *t*BuXPhos experiment after sitting at RT for 2 h. (1) is 50% *t*BuOH in H_2O. (2) is 30% 1,4-Dioxane in *t*BuOH. (3) is 10% *t*BuOH in PhMe. (4) is 20% *t*BuOH, 30% 1,4-Dioxane, 50% H_2O.

Table 4. Overview of observed trends for substate compatibility with the respective ancillary ligands.

Ligand	***Nucleophile***	***Aryl (pseudo)Halide***
XPhos	imidazole, glycine, cyclic 2°, 1°	quinazoline, pyrimidines, pyridine, pyridazine
*t*BuXPhos	cyclic 2°, sulfonamides, acyclic 2°, lactam, thiazolidine, tetrazole, carbamate	iodo tyrosine, pyridine, quinazoline, pyrimidine, thiazole
Me_3(OMe)*t*BuXPhos	acyclic 2°, 1°, cyclic 2°, sulfonamide, lactam, imidazole, cyclic urea	furan, quinazoline, thiophene, pyridines, electron rich arenes, iodo tyrosine, imidazole
Me_4*t*BuXPhos	imidazole, glycine, sulfonamide, ammonia, lactam, cyclic 2°, acyclic 2°	nitrobenzene, pyridazines, imidazole, pyrimidine
BrettPhos	sulfonamide, imidazole, glycine, cyclic urea	pyrimidine, dimethoxy benzene, trifluorobenzene
*t*BuBrettPhos	sulfonamide, glycine, cyclic 2°, cyclic urea, lactam, tetrazole, imidazole, acyclic 2°	furan, quinazoline, thiophene, pyridine, iodo tyrosine, resorcinol, nitrobenzene, electron rich arenes
AdBrettPhos	sulfonamide, 1°, imidazole, cyclic 2°	thiazole, furan, quinazoline, heterocycles
XantPhos	sulfonamide, cyclic 2°, cyclic urea	heterocycles
EPhos	1°, acyclic 2°, thiazolidine, methylazetidine, ammonia	furan, thiazole, quinazoline, pyrimidine, pyridine, imidazole
SPhos	bulky acyclic 2°, cyclic 2°, 1°	furan, quinazoline, pyrimidine, pyridine
RuPhos	pyrrolidine, piperidine, N-methylpiperazine	quinazoline, pyrimidine

RuPhos was found to be an ineffective ligand for the chosen substrates whereas SPhos, XantPhos, and EPhos were generally effective when coupling the nucleophiles with heterocyclic aryl halides. All other ligands were effective at performing the Buchwald-Hartwig amination while possessing strengths with certain classes of electrophiles and nucleophiles. Comparing room temperature reactions to 100 °C reactions, there were a minority amount that performed better at room temperature, and performed worse or failed at 100 °C. Typically, reactions that showed promise at room temperature were only improved when they were heated for 2 h. Reactions containing water as a co-solvent were found to be quite effective in many iterations. Whether this is due to the nature of the substates, reagents, or order of addition is unknown, but observing

Buchwald-Hartwig being successful with a large amount of water present shows much promise for potentially “greener” reaction conditions that are effective.

2.4 Conclusion

Herein reported is a library of Buchwald-Hartwig reactions that can guide synthetic chemists in determining their choice of ligand and other reaction conditions when performing this cross-coupling. The plethora of nucleophiles and aryl (pseudo) halides gives a vast array of examples that act as a template for when a chemist must attempt a Buchwald-Hartwig reaction with no literature precedence. Using HTE as a tool to discover the efficiency or to optimize them is a relatively new concept and should pursued at greater lengths amongst the community in order to expedite research and develop new transformations. This tool helped create a library of over 8,000 Buchwald-Hartwig reactions, which would have taken years to complete if the reactions were to be performed solely with man-power. Continuing to use HTE to build libraries of reactions has an even great implication to machine learning and artificial intelligence. Feeding the data from large libraries into algorithms can create a workflow that predicts how reactions will perform, and how one might approach performing a certain transformation. Pursing this pathway will not only make a chemists’ life easier, but also help chemists perform reactions that were thought to be impossible in the past.

2.5 Supplementary Information

2.5.1 Synthesis Experimentals

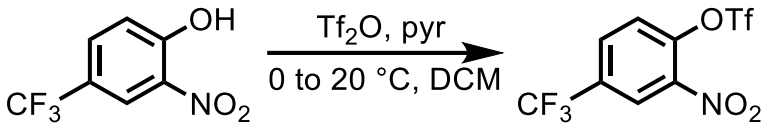

2-nitro-4-(trifluoromethyl)phenyl trifluoromethanesulfonate

Scheme 2. Reaction scheme for the synthesis of 2-nitro-4-(trifluoromethyl)phenyl trifluoromethanesulfonate.

2-Nitro-4-(trifluoromethyl)phenol (1.00 g, 4.83 mmol) was dissolved in anhydrous DCM (15 mL), followed by the addition of pyridine (0.764 g, 9.66 mmol). The solution was cooled to 0 °C, and triflic anhydride (1.64 g, 5.79 mmol) was added. After the addition of triflic anhydride, the solution was heated to room temperature. The reaction was monitored with TLC using 30% EtOAc in Hexanes as the eluent. Upon completion, the solution was rotary evaporated and dried under high vacuum. Purification was achieved via silica flash chromatography using a 0-40% EtOAc:Hexanes gradient. Product was found in 10% EtOAc:Hexanes fractions. Fractions were assayed via TLC using the previously used eluent. Pure fractions were combined, rotary evaporated, and dried under high vacuum. Yield: 1.58 g (96%); LC-MS (LR, ESI) = Calcd. for $C_8H_3F_6NO_5S$: 338.96 (m/z), found: 337.78 $[M-H]^-$. ^1H NMR (500 MHz, $CDCl_3$) δ 8.45 (t, J = 1.8 Hz, 1H), 8.03 (dd, J = 8.6, 2.1 Hz, 1H), 7.65 (d, J = 8.6 Hz, 1H).

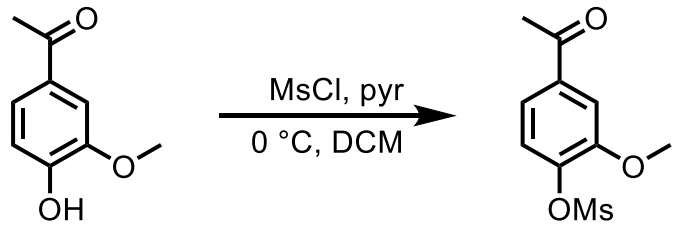

4-acetyl-2-methoxyphenyl methanesulfonate

Scheme 3. Reaction scheme for the synthesis of 4-acetyl-2-methoxyphenyl methanesulfonate.

4-Hydroxy-3-methoxyacetophenone (2.50 g, 15.0 mmol) was dissolved in anhydrous DCM (25 mL), followed by the addition of pyridine (2.38 g, 19.6 mmol). The solution was cooled to 0 °C, and methanesulfonyl chloride (2.24 g, 19.6 mmol) was added slowly. The reaction was monitored with TLC using 1:3 EtOAc:Hexanes as the eluent. Upon completion, the solution was

rotary evaporated and dried under high vacuum. The crude product was purified via flash chromatography using a 10-60% EtOAc:Hexanes gradient. Product eluted at 30%. Fractions were assayed via TLC using the previous 1:3 EtOAc:Hexanes eluent. Pure fractions were combined, rotary evaporated, and dried under high vacuum. Yield: 3.42 g (93%); LC-MS (LR, ESI) = Calcd. for $C_{10}H_{12}O_5S$: 244.04 (m/z), found: 243.01 $[M-H]^-$. ^1H NMR (500 MHz, $CDCl_3$) δ 7.63 (d, *J* = 2.0 Hz, 1H), 7.56 (dd, *J* = 8.3, 2.0 Hz, 1H), 7.39 (d, *J* = 8.3 Hz, 1H), 3.95 (s, 3H), 3.22 (s, 3H), 2.60 (s, 3H).

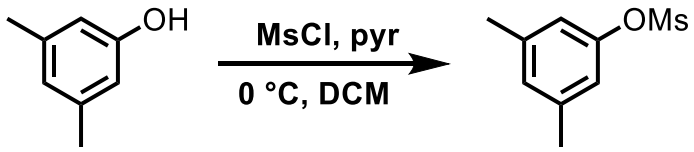

3,5-dimethylphenyl methanesulfonate

Scheme 4. Reaction scheme for the synthesis of 3,5-dimethylphenyl methanesulfonate.

3,5-Dimethylphenol (2.50 g, 20.5 mmol) was dissolved in anhydrous DCM (25 mL), followed by the addition of pyridine (3.24 g, 40.9 mmol). The solution was cooled to 0 °C, and methanesulfonyl chloride (3.05 g, 26.6 mmol) was added slowly. The reaction was monitored with TLC using 25% EtOAc:Hexanes as the eluent. Upon completion, the solution was rotary evaporated and dried under high vacuum. The crude product was purified via flash chromatography using a 10-50% EtOAc:Hexanes gradient. Product eluted at 25%. Fractions were assayed via TLC using the previous 25% EtOAc:Hexanes eluent. Pure fractions were combined, rotary evaporated, and dried under high vacuum. Yield: 3.42 g (83%); LC-MS (LR, ESI) = Calcd. for $C_9H_{12}O_3S$: 200.05 (m/z), found: 198.91 $[M-H]^-$. ^1H NMR (500 MHz, $CDCl_3$) δ 6.95 (s, 1H), 6.90 (s, 2H), 3.12 (s, 3H), 2.33 (s, 6H).

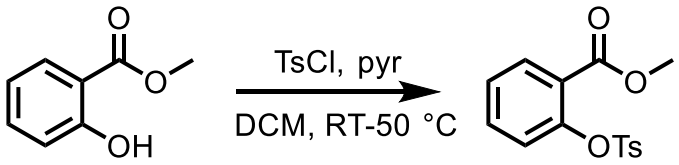

methyl 2-(tosyloxy)benzoate

Scheme 5. Reaction scheme for the synthesis of methyl 2-(tosyloxy)benzoate.

Methyl salicylate (3.00 g, 19.7 mmol) was dissolved in anhydrous DCM (35 mL), followed by the addition of pyridine (3.899 g, 49.3 mmol). Tosyl chloride (9.398 g, 49.3 mmol) was then added, and the solution was heated to 50 °C. The reaction was monitored with TLC using 50% DCM in Hexanes as the eluent. Upon completion, the solution was extracted in 0.1 M HCl, 0.1 M $NaHCO_3$, and brine. The crude product was purified via flash chromatography using a 0-40% EtOAc:Hexanes gradient. Pure fractions were combined, rotary evaporated, and dried under high vacuum. Yield: 4.62 g (76%); LC-MS (LR, ESI) = Calcd. for $C_{15}H_{14}O_5S$: 306.06 (m/z), found: 305.01 $[M-H]^-$. ^1H NMR (500 MHz, $CDCl_3$) δ 7.87 (dd, *J* = 7.8, 1.8 Hz, 1H), 7.75 – 7.68 (m, 2H), 7.46 (ddd, *J* = 8.2, 7.4, 1.8 Hz, 1H), 7.36 – 7.28 (m, 3H), 7.09 (dd, *J* = 8.2, 1.2 Hz, 1H), 3.80 (s, 3H), 2.45 (s, 3H).

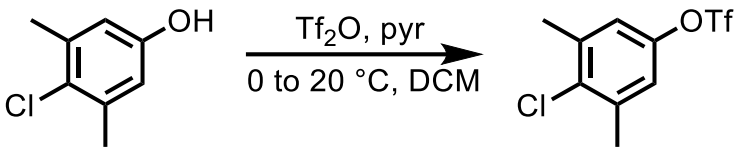

4-chloro-3,5-dimethylphenyl trifluoromethanesulfonate

Scheme 6. Reaction scheme for the synthesis of 4-chloro-3,5-dimethylphenyl trifluoromethanesulfonate.

4-Chloro-3,5-dimethylphenol (2.50 g, 16.0 mmol) was dissolved in anhydrous DCM (35 mL), followed by the addition of pyridine (2.53 g, 31.9 mmol). The solution was cooled to 0 °C, and triflic anhydride (5.41 g, 19.2 mmol) was added. After the addition of triflic anhydride, the solution was heated to room temperature. The reaction was monitored with TLC using 10% EtOAc:Hexanes as the eluent. Upon completion, the solution was rotary evaporated and dried under high vacuum. Purification was achieved via silica flash chromatography using a 10-25% EtOAc:Hexanes gradient. Fractions were assayed via TLC using the previously used eluent. Pure fractions were combined, rotary evaporated, and dried under high vacuum. Yield: 4.21 g (91%); LC-MS (LR, ESI) = Calcd. for $C_9H_8ClF_3O_3S$: 287.98 (m/z), found: 286.43 $[M-H]^-$. ^1H NMR (500 MHz, $CDCl_3$) δ 7.01 (s, 2H), 2.41 (s, 6H).

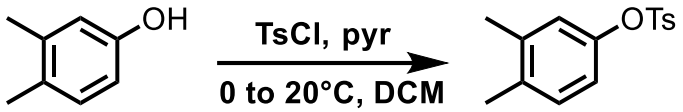

3,4-dimethylphenyl 4-methylbenzenesulfonate

Scheme 7. Reaction scheme for the synthesis of 3,4-dimethylphenyl 4-methylbenzenesulfonate.

3,4-Dimethylphenol (2.50 g, 20.5 mmol) was dissolved in anhydrous DCM (35 mL), followed by the addition of pyridine (3.24 g, 40.9 mmol). The solution was cooled to 0 °C, and tosyl chloride (3.05 g, 26.6 mmol) was added slowly. The reaction was monitored with TLC using 25% EtOAc:Hexanes as the eluent. Upon completion, the solution was rotary evaporated and dried under high vacuum. The crude product was purified via flash chromatography using a 10-60% EtOAc:Hexanes gradient. Fractions were assayed via TLC using the previous 30% EtOAc:Hexanes eluent. Pure fractions were combined, rotary evaporated, and dried under high vacuum. Yield: 4.12 g (73%); LC-MS (LR, ESI) = Calcd. for $C_{15}H_{16}O_3S$: 276.08 (m/z), found: 284.98 $[M-H]^-$. ^1H NMR (500 MHz, $CDCl_3$) δ 7.72 (d, *J* = 8.3 Hz, 2H), 7.31 (dd, *J* = 8.6, 0.7 Hz, 2H), 6.99 (d, *J* = 8.2 Hz, 1H), 6.82 (d, *J* = 2.6 Hz, 1H), 6.63 (dd, *J* = 8.2, 2.6 Hz, 1H), 2.45 (s, 3H), 2.19 (d, *J* = 7.1 Hz, 6H).

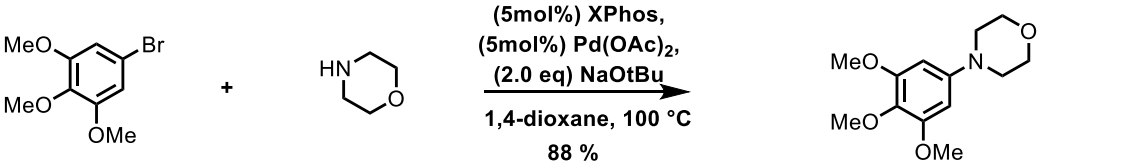

5-bromo-1,2,3-trimethoxybenzene **morpholine** **4-(3,4,5-trimethoxyphenyl)morpholine**

Scheme 8. Reaction scheme of chosen batch reaction to optimize as a positive control for HTE.

5-Bromo-1,2,3-trimethoxybenzene (100 mg, 0.405 mmol) was dissolved in anhydrous 1,4-dioxane (8 mL) under an Ar atmosphere, followed by the addition of morpholine (53.0 mg, 0.607 mmol), XPhos (9.65 mg, 0.020 mmol), and $Pd(OAc)_2$ (4.53 mg, 0.020 mmol). The solution was heated to 100 °C, and NaOtBu (77.8 mg, 0.809 mmol) was added. The reaction was monitored with TLC using 1:1 EtOAc:Hexanes as the eluent. Upon completion, the solution was run through a silica plug, rotary evaporated, and dried under high vacuum. The crude product was purified via flash chromatography using 25-75% EtOAc:Hexanes. Pure fractions were combined, rotary evaporated, and dried under high vacuum. Yield: 89 mg (88%); LC-MS (LR, ESI) = Calcd. for $C_{13}H_{19}NO_4$: 253.13 (m/z), found: 254.05 $[M+H]^+$. ^1H NMR (500 MHz, $CDCl_3$) δ 6.14 (s, 2H), 3.84 (s, 9H), 3.78 (t, *J* = 5.3 Hz, 4H), 3.10 (t, *J* = 5.3 Hz, 4H).

2.5.2 Order of Addition HTE Contour Plots

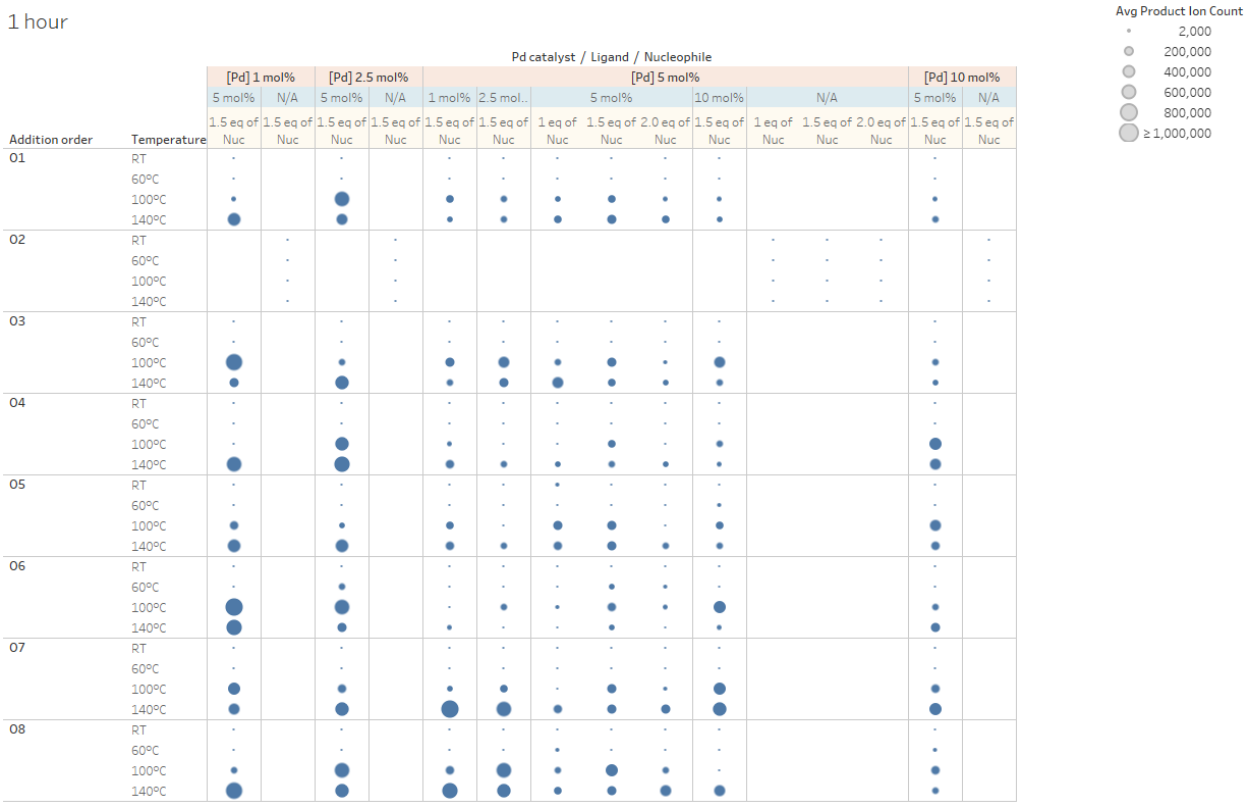

Figure 13. Contrast plot from the order of addition HTE of the data at the 1 h mark. The larger the dot at the intersection of condition labels, the greater the product ion count from observed in DESI-MS.

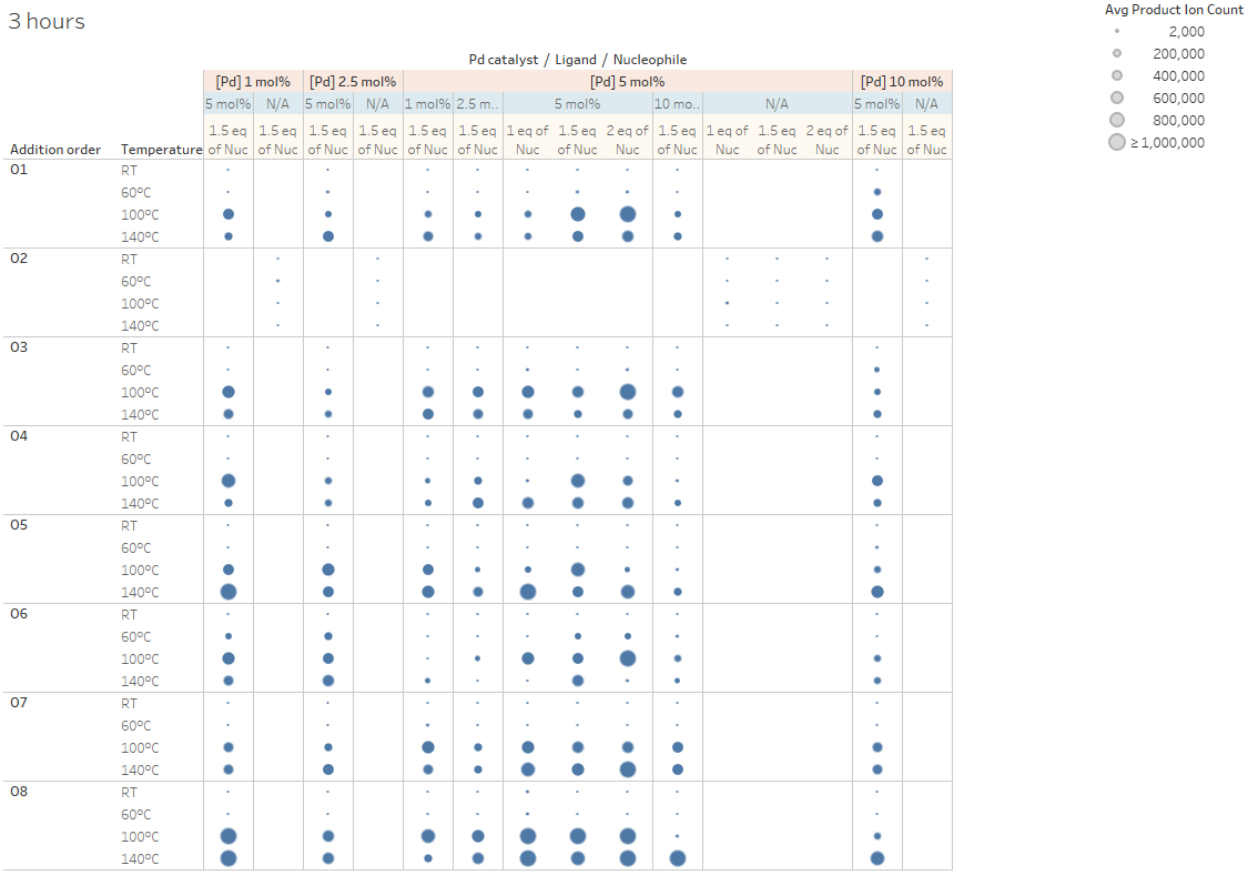

Figure 14. Contrast plot from the order of addition HTE of the data at the 3 h mark. The larger the dot at the intersection of condition labels, the greater the product ion count from observed in DESI-MS.

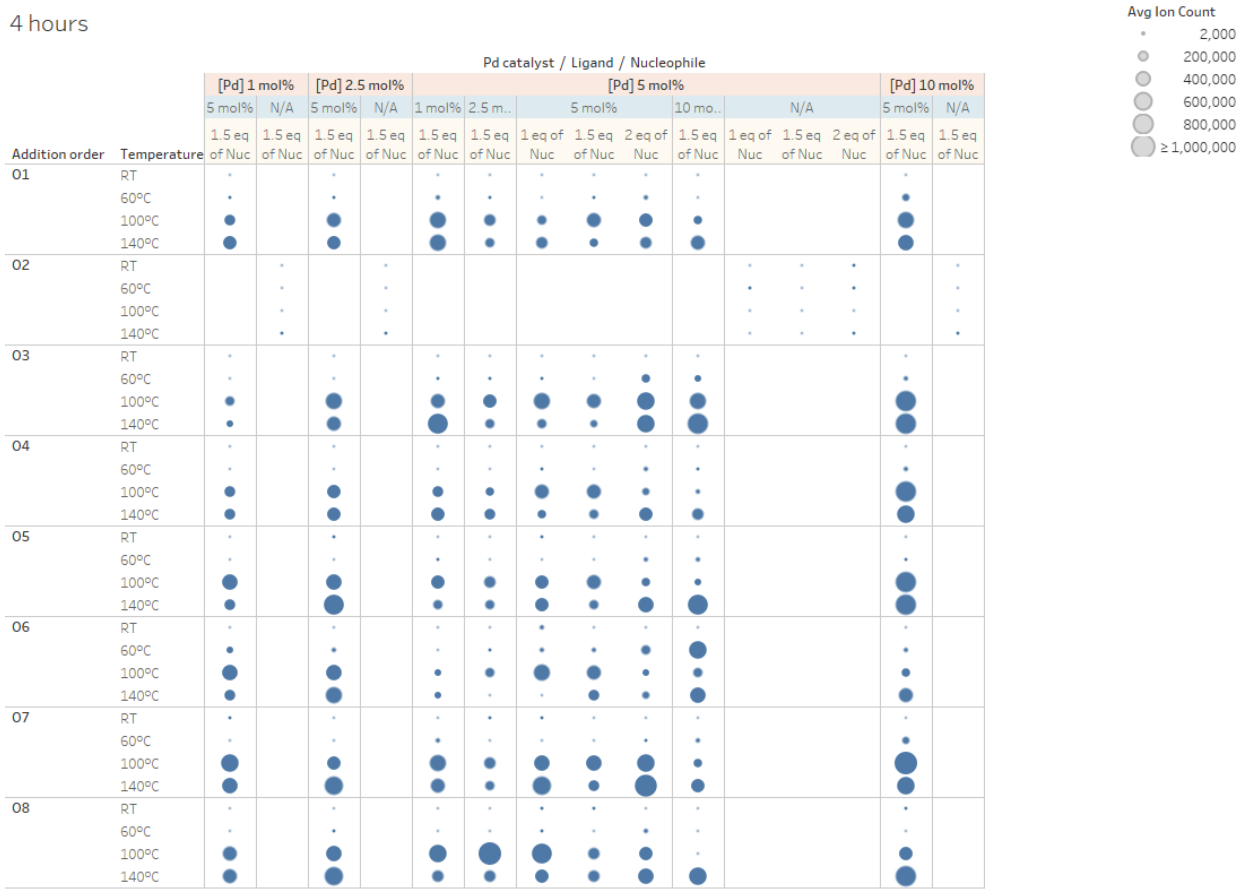

Figure 15. Contrast plot from the order of addition HTE of the data at the 4 h mark. The larger the dot at the intersection of condition labels, the greater the product ion count from observed in DESI-MS.

2.5.3 Broad Substrate Screen Heat Maps

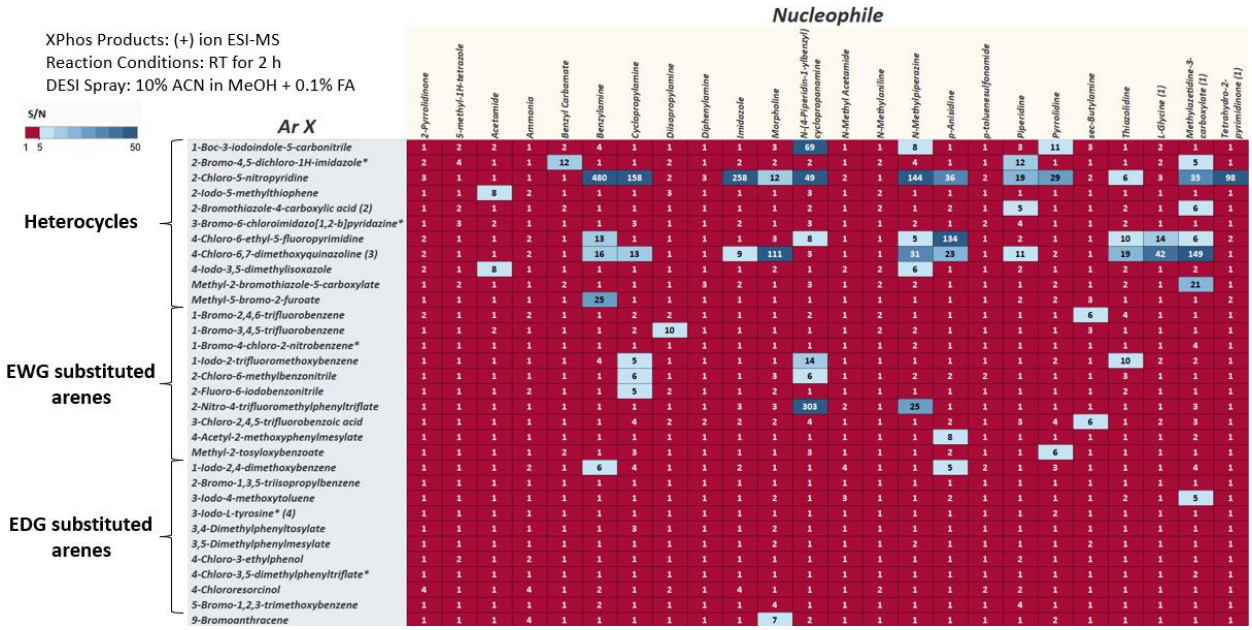

Figure 16. Positive ion heat map from the XPhos experiment after sitting at RT for 2 h. (1) is 50% *t*BuOH in H_2O. (2) is 30% 1,4-Dioxane in *t*BuOH. (3) is 10% *t*BuOH in PhMe. (4) is 20% *t*BuOH, 30% 1,4-Dioxane, 50% H_2O.

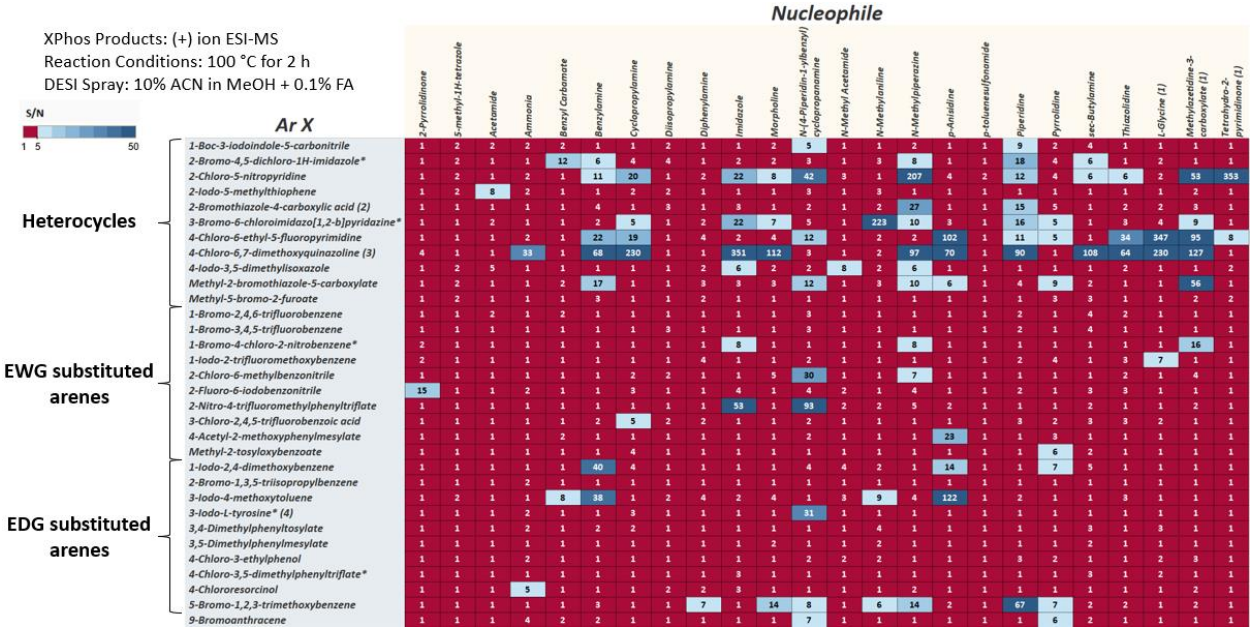

Figure 17. Positive ion heat map from the XPhos experiment after sitting at 100 °C for 2 h. (1) is 50% *t*BuOH in H_2O. (2) is 30% 1,4-Dioxane in *t*BuOH. (3) is 10% *t*BuOH in PhMe. (4) is 20% *t*BuOH, 30% 1,4-Dioxane, 50% H_2O.

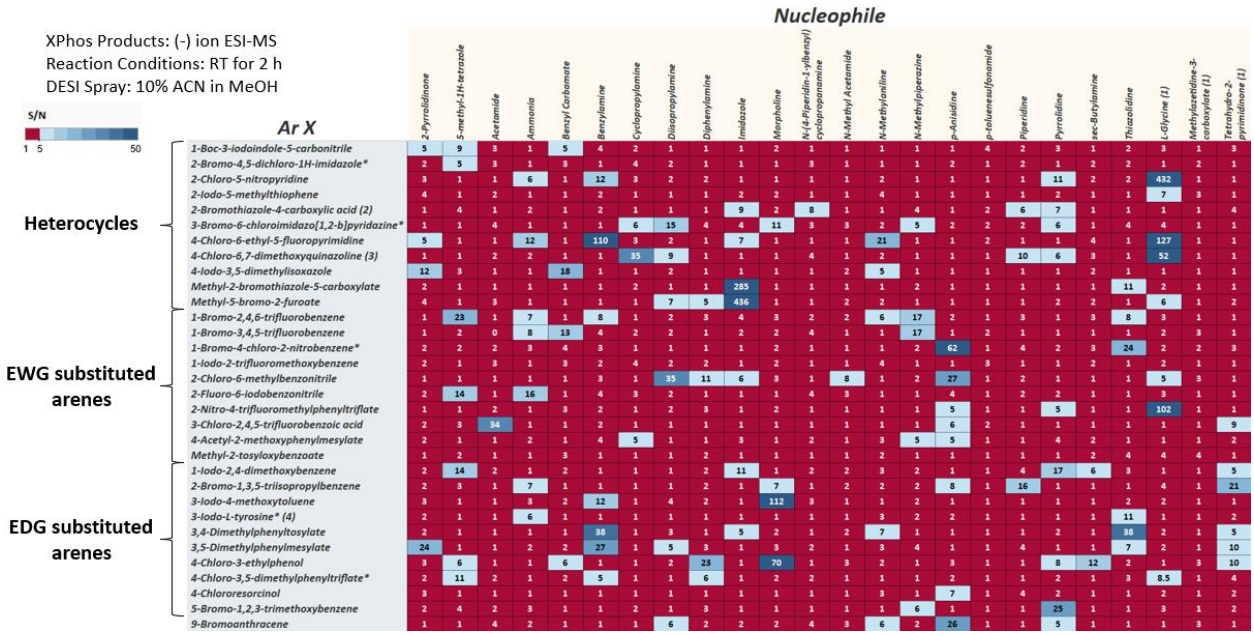

Figure 18. Negative ion heat map from the XPhos experiment after sitting at RT for 2 h. (1) is 50% *t*BuOH in H_2O. (2) is 30% 1,4-Dioxane in *t*BuOH. (3) is 10% *t*BuOH in PhMe. (4) is 20% *t*BuOH, 30% 1,4-Dioxane, 50% H_2O.

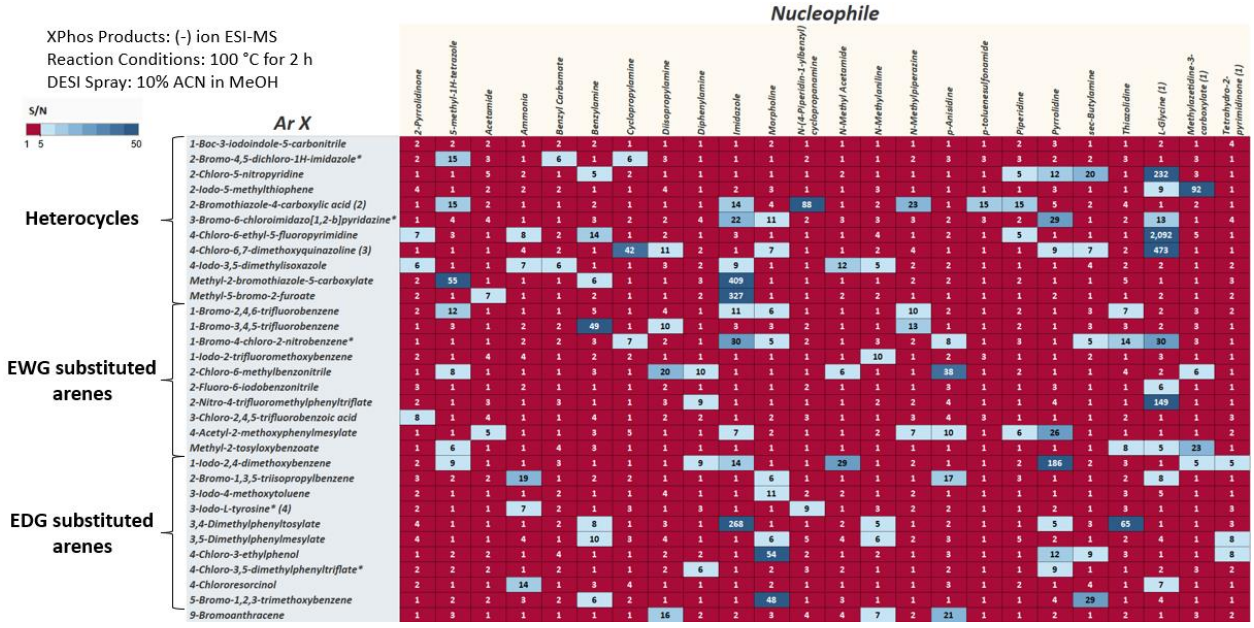

Figure 19. Negative ion heat map from the XPhos experiment after sitting at 100 °C for 2 h. (1) is 50% *t*BuOH in H_2O. (2) is 30% 1,4-Dioxane in *t*BuOH. (3) is 10% *t*BuOH in PhMe. (4) is 20% *t*BuOH, 30% 1,4-Dioxane, 50% H_2O.

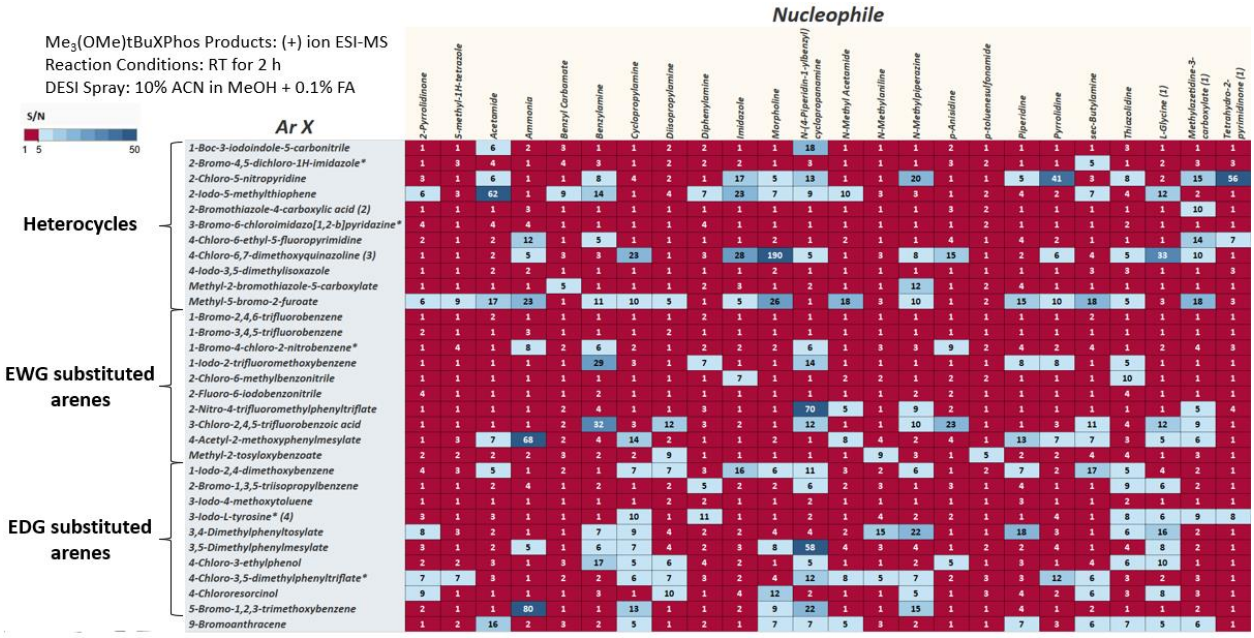

Figure 20. Positive ion heat map from the Me_3(OMe)*t*BuXPhos experiment after sitting at RT for 2 h. (1) is 50% *t*BuOH in H_2O. (2) is 30% 1,4-Dioxane in *t*BuOH. (3) is 10% *t*BuOH in PhMe. (4) is 20% *t*BuOH, 30% 1,4-Dioxane, 50% H_2O.

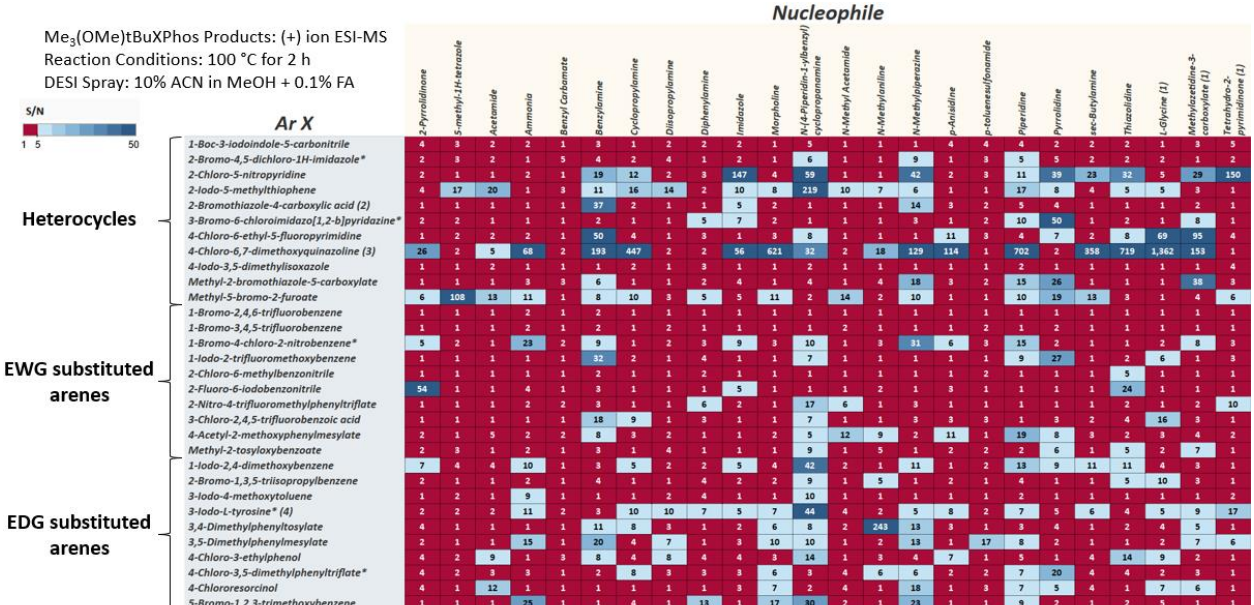

Figure 21. Positive ion heat map from the Me_3(OMe)*t*BuXPhos experiment after sitting at 100 °C for 2 h. (1) is 50% *t*BuOH in H_2O. (2) is 30% 1,4-Dioxane in *t*BuOH. (3) is 10% *t*BuOH in PhMe. (4) is 20% *t*BuOH, 30% 1,4-Dioxane, 50% H_2O.

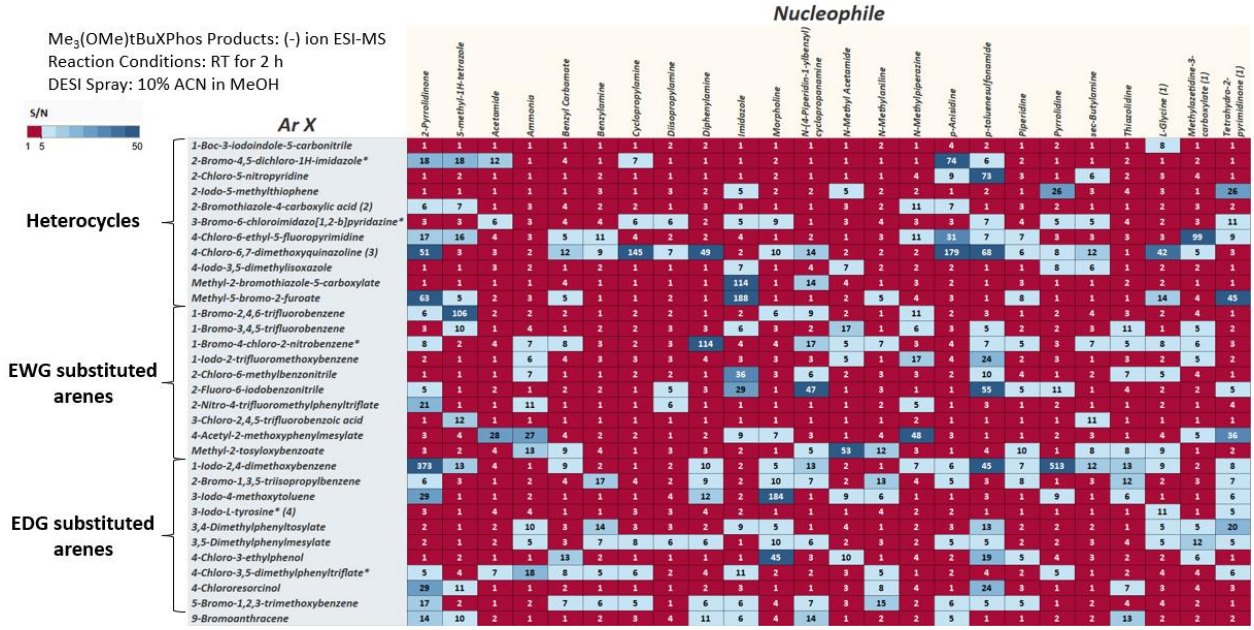

Figure 22. Negative ion heat map from the Me_3(OMe)*t*BuXPhos experiment after sitting at RT for 2 h. (1) is 50% *t*BuOH in H_2O. (2) is 30% 1,4-Dioxane in *t*BuOH. (3) is 10% *t*BuOH in PhMe. (4) is 20% *t*BuOH, 30% 1,4-Dioxane, 50% H_2O.

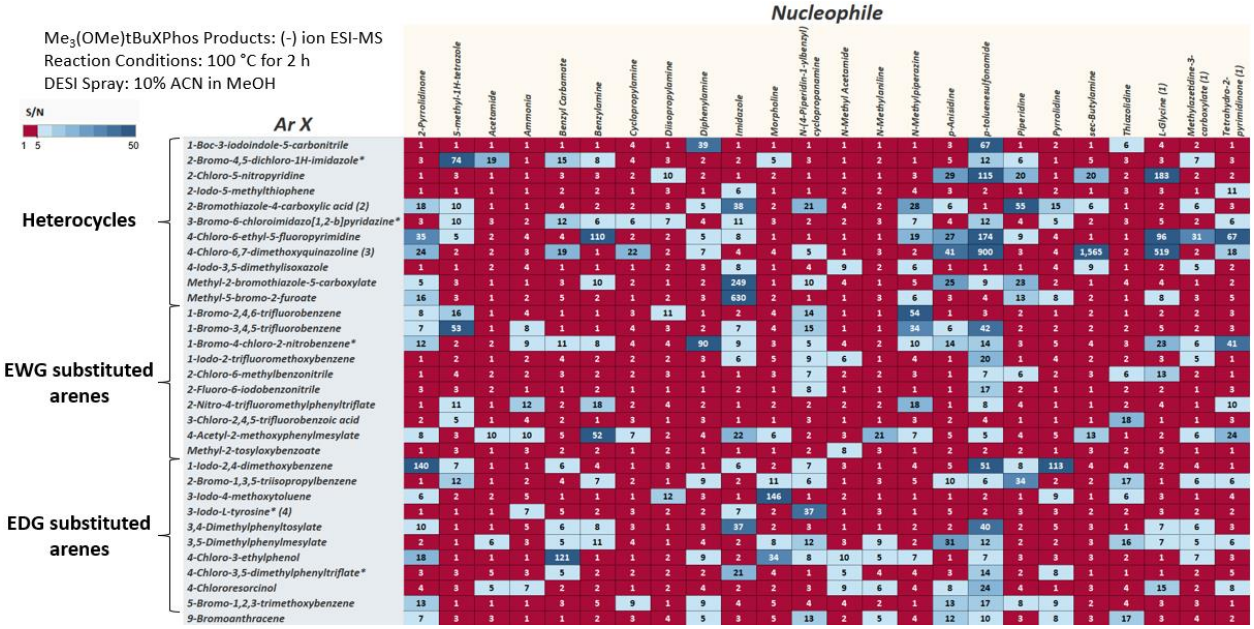

Figure 23. Negative ion heat map from the Me_3(OMe)*t*BuXPhos experiment after sitting at 100 °C for 2 h. (1) is 50% *t*BuOH in H_2O. (2) is 30% 1,4-Dioxane in *t*BuOH. (3) is 10% *t*BuOH in PhMe. (4) is 20% *t*BuOH, 30% 1,4-Dioxane, 50% H_2O.

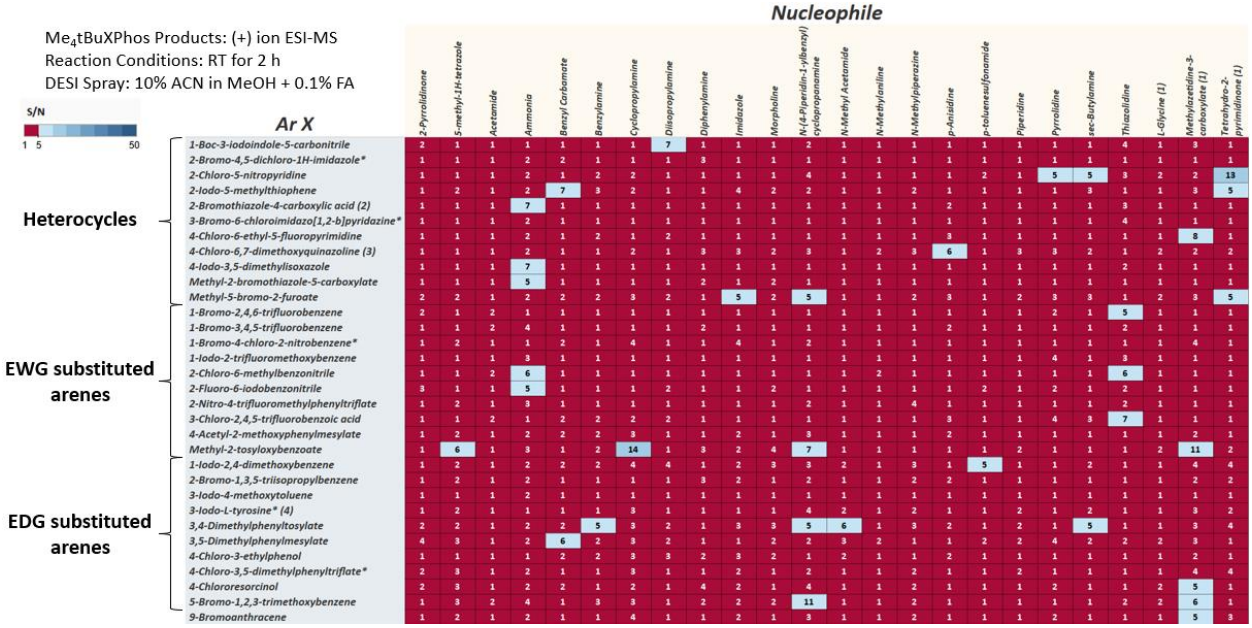

Figure 24. Positive ion heat map from the Me$_4$*t*BuXPhos experiment after sitting at RT for 2 h. (1) is 50% *t*BuOH in H_2O. (2) is 30% 1,4-Dioxane in *t*BuOH. (3) is 10% *t*BuOH in PhMe. (4) is 20% *t*BuOH, 30% 1,4-Dioxane, 50% H_2O.

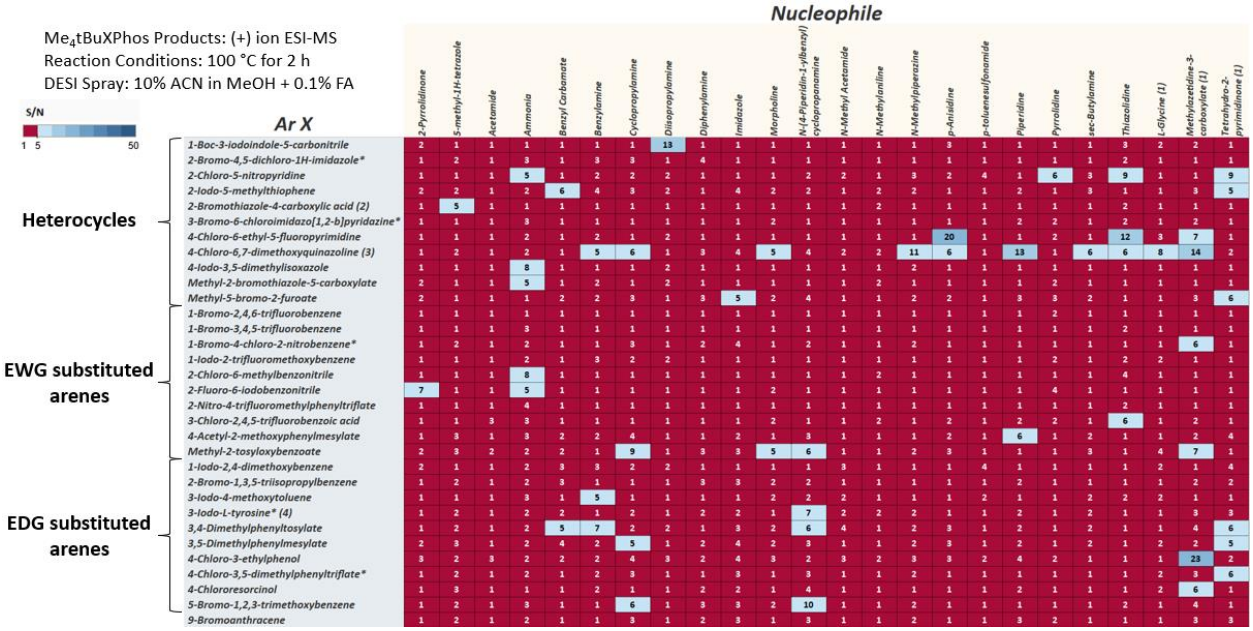

Figure 25. Positive ion heat map from the Me$_4$*t*BuXPhos experiment after sitting at 100 °C for 2 h. (1) is 50% *t*BuOH in H_2O. (2) is 30% 1,4-Dioxane in *t*BuOH. (3) is 10% *t*BuOH in PhMe. (4) is 20% *t*BuOH, 30% 1,4-Dioxane, 50% H_2O.

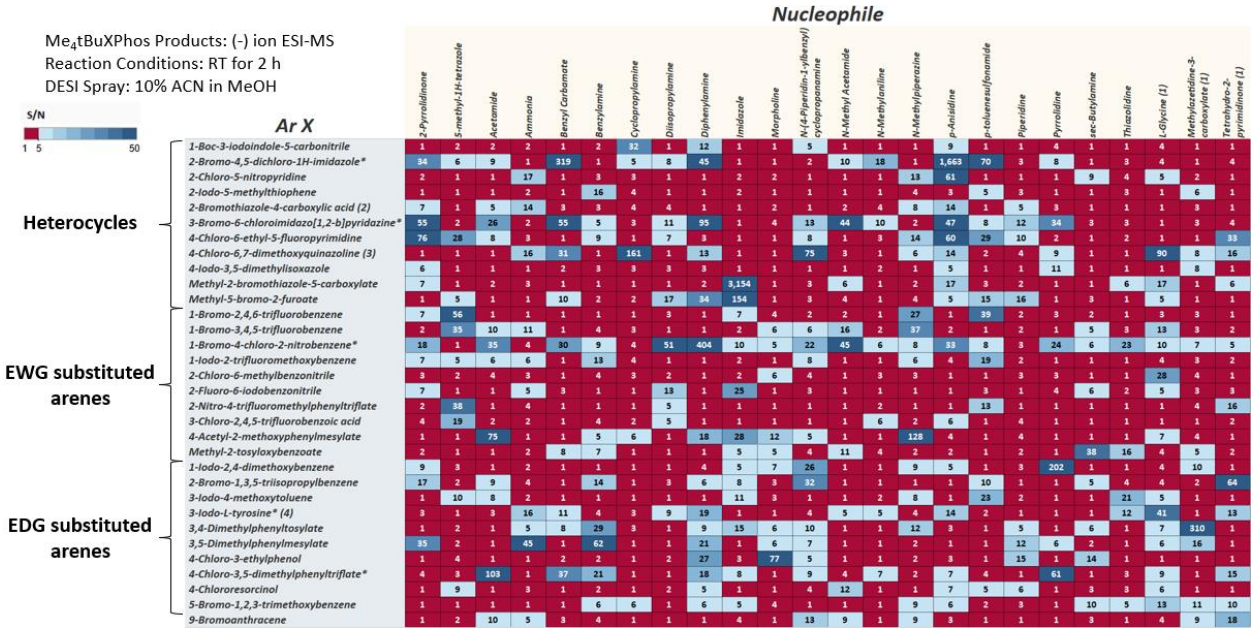

Figure 26. Negative ion heat map from the Me$_4$*t*BuXPhos experiment after sitting at RT for 2 h. (1) is 50% *t*BuOH in H_2O. (2) is 30% 1,4-Dioxane in *t*BuOH. (3) is 10% *t*BuOH in PhMe. (4) is 20% *t*BuOH, 30% 1,4-Dioxane, 50% H_2O.

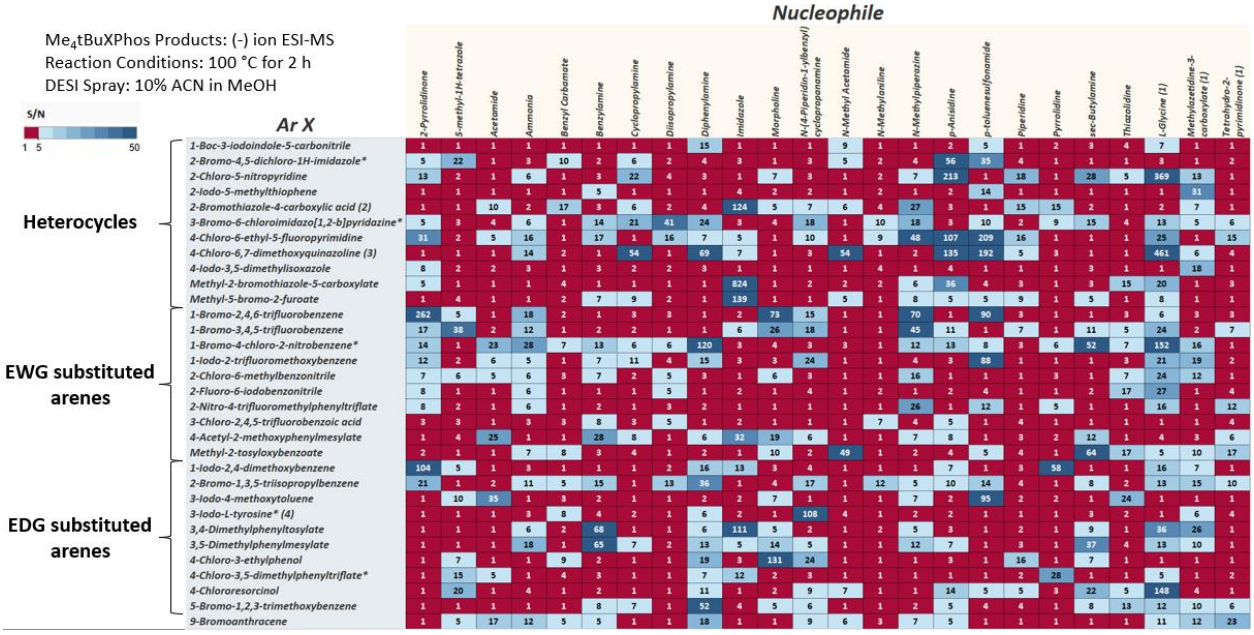

Figure 27. Negative ion heat map from the Me$_4$*t*BuXPhos experiment after sitting at 100 °C for 2 h. (1) is 50% *t*BuOH in H_2O. (2) is 30% 1,4-Dioxane in *t*BuOH. (3) is 10% *t*BuOH in PhMe. (4) is 20% *t*BuOH, 30% 1,4-Dioxane, 50% H_2O.

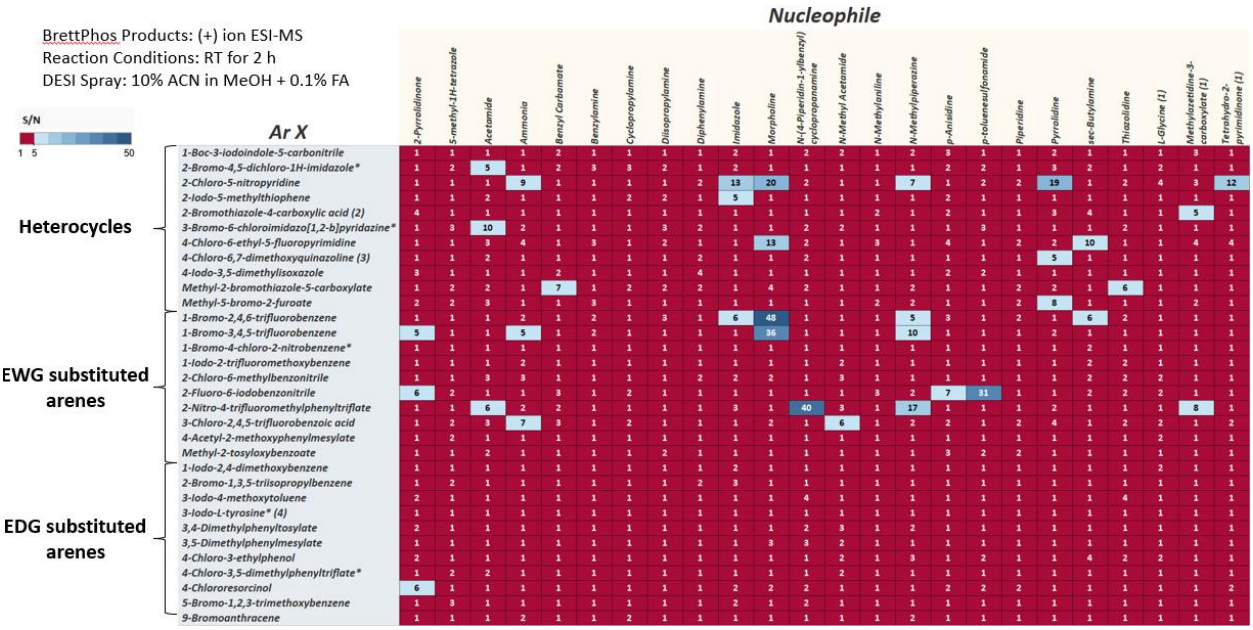

Figure 28. Positive ion heat map from the BrettPhos experiment after sitting at RT for 2 h. (1) is 50% *t*BuOH in H_2O. (2) is 30% 1,4-Dioxane in *t*BuOH. (3) is 10% *t*BuOH in PhMe. (4) is 20% *t*BuOH, 30% 1,4-Dioxane, 50% H_2O.

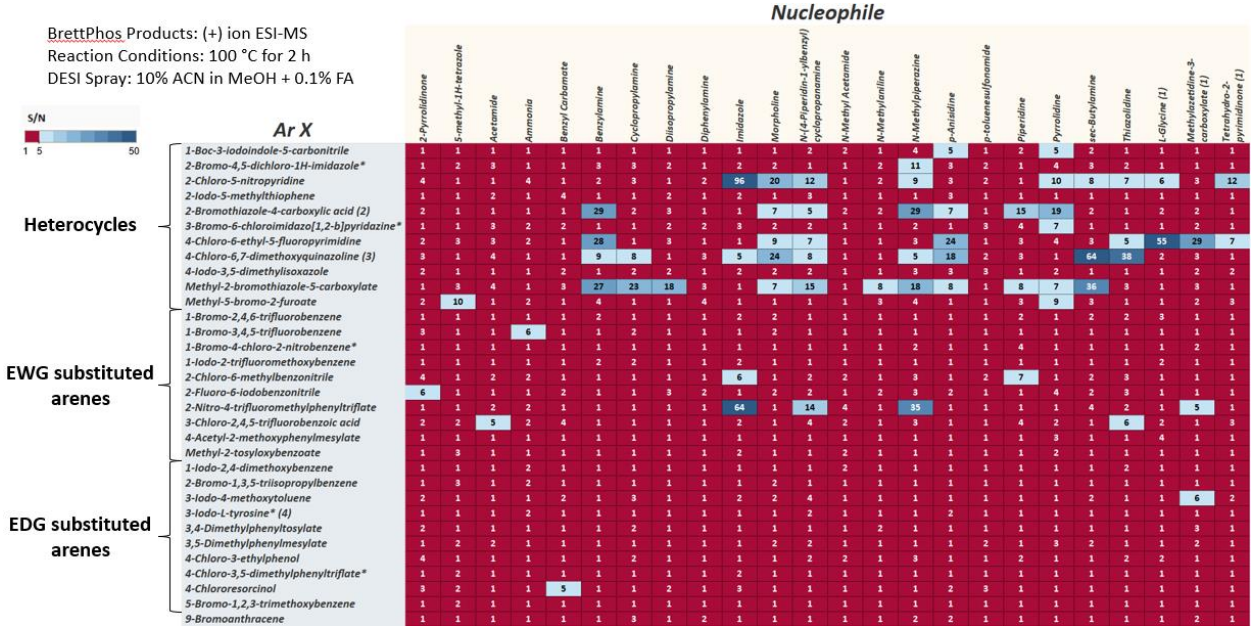

Figure 29. Positive ion heat map from the BrettPhos experiment after sitting at 100 °C for 2 h. (1) is 50% *t*BuOH in H_2O. (2) is 30% 1,4-Dioxane in *t*BuOH. (3) is 10% *t*BuOH in PhMe. (4) is 20% *t*BuOH, 30% 1,4-Dioxane, 50% H_2O.

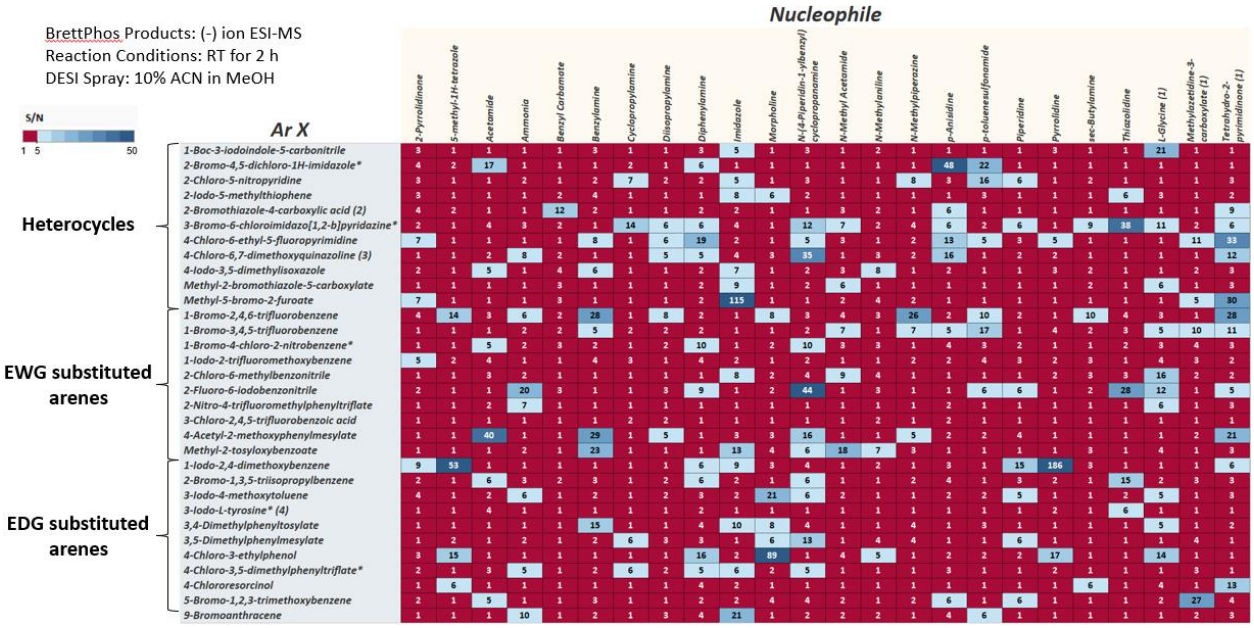

Figure 30. Negative ion heat map from the BrettPhos experiment after sitting at RT for 2 h. (1) is 50% *t*BuOH in H_2O. (2) is 30% 1,4-Dioxane in *t*BuOH. (3) is 10% *t*BuOH in PhMe. (4) is 20% *t*BuOH, 30% 1,4-Dioxane, 50% H_2O.

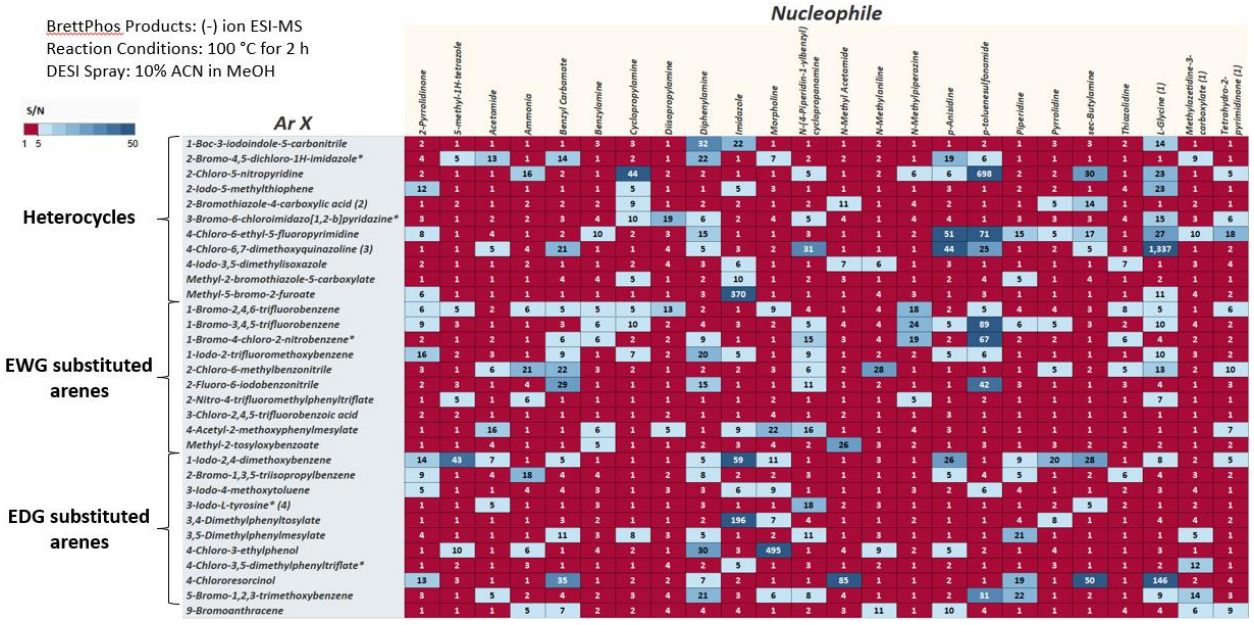

Figure 31. Negative ion heat map from the BrettPhos experiment after sitting at 100 °C for 2 h. (1) is 50% *t*BuOH in H_2O. (2) is 30% 1,4-Dioxane in *t*BuOH. (3) is 10% *t*BuOH in PhMe. (4) is 20% *t*BuOH, 30% 1,4-Dioxane, 50% H_2O.

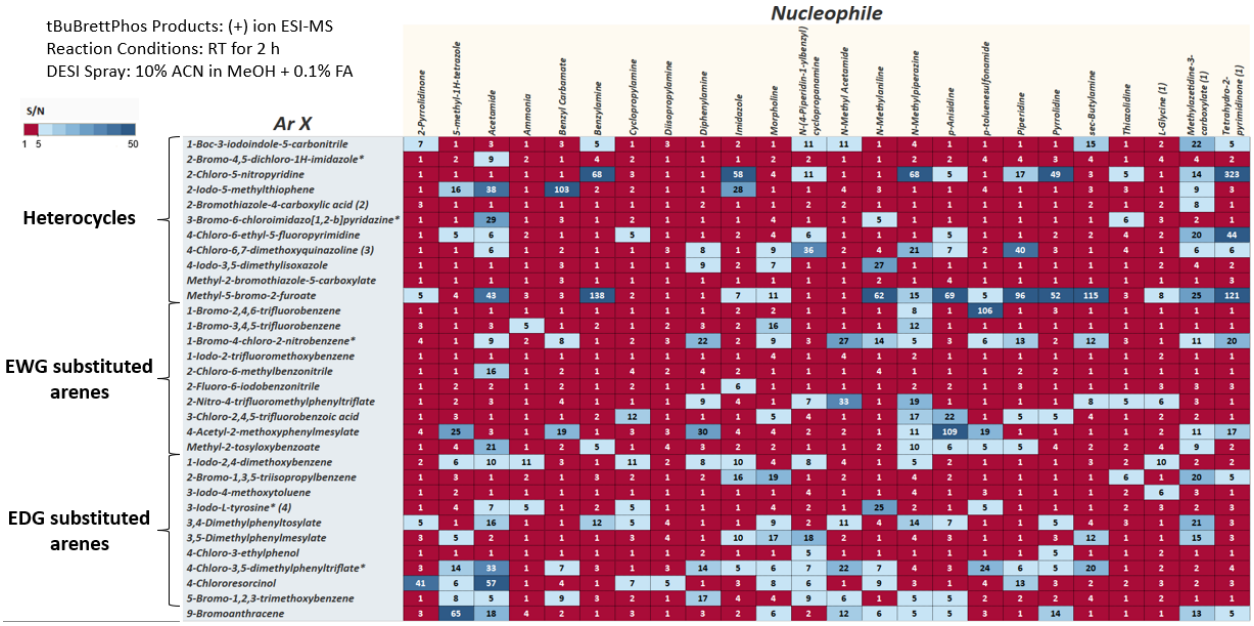

Figure 32. Positive ion heat map from the *t*BuBrettPhos experiment after sitting at RT for 2 h. (1) is 50% *t*BuOH in H_2O. (2) is 30% 1,4-Dioxane in *t*BuOH. (3) is 10% *t*BuOH in PhMe. (4) is 20% *t*BuOH, 30% 1,4-Dioxane, 50% H_2O.

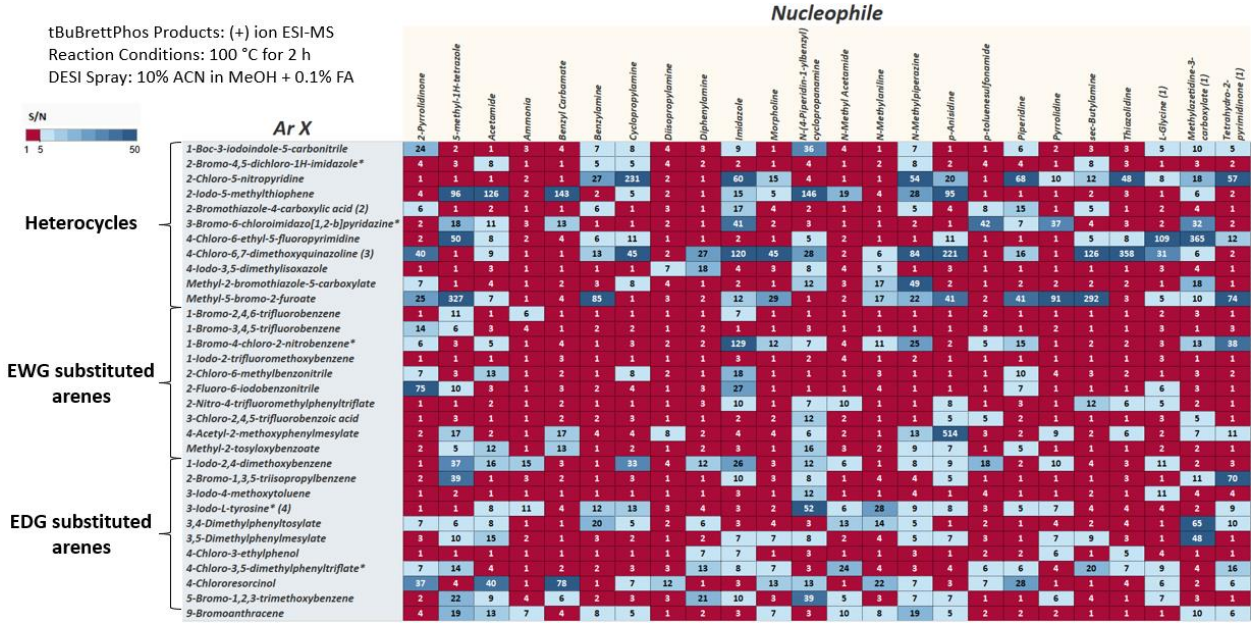

Figure 33. Positive ion heat map from the *t*BuBrettPhos experiment after sitting at 100 °C for 2 h. (1) is 50% *t*BuOH in H_2O. (2) is 30% 1,4-Dioxane in *t*BuOH. (3) is 10% *t*BuOH in PhMe. (4) is 20% *t*BuOH, 30% 1,4-Dioxane, 50% H_2O.

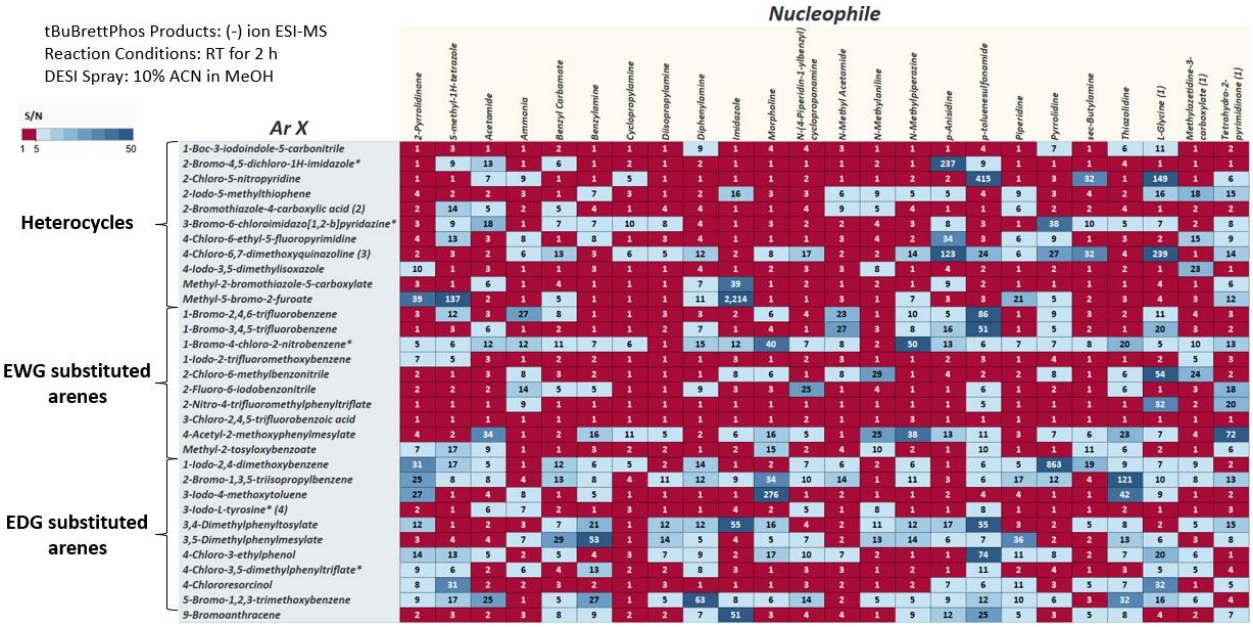

Figure 34. Negative ion heat map from the *t*BuBrettPhos experiment after sitting at RT for 2 h. (1) is 50% *t*BuOH in H_2O. (2) is 30% 1,4-Dioxane in *t*BuOH. (3) is 10% *t*BuOH in PhMe. (4) is 20% *t*BuOH, 30% 1,4-Dioxane, 50% H_2O.

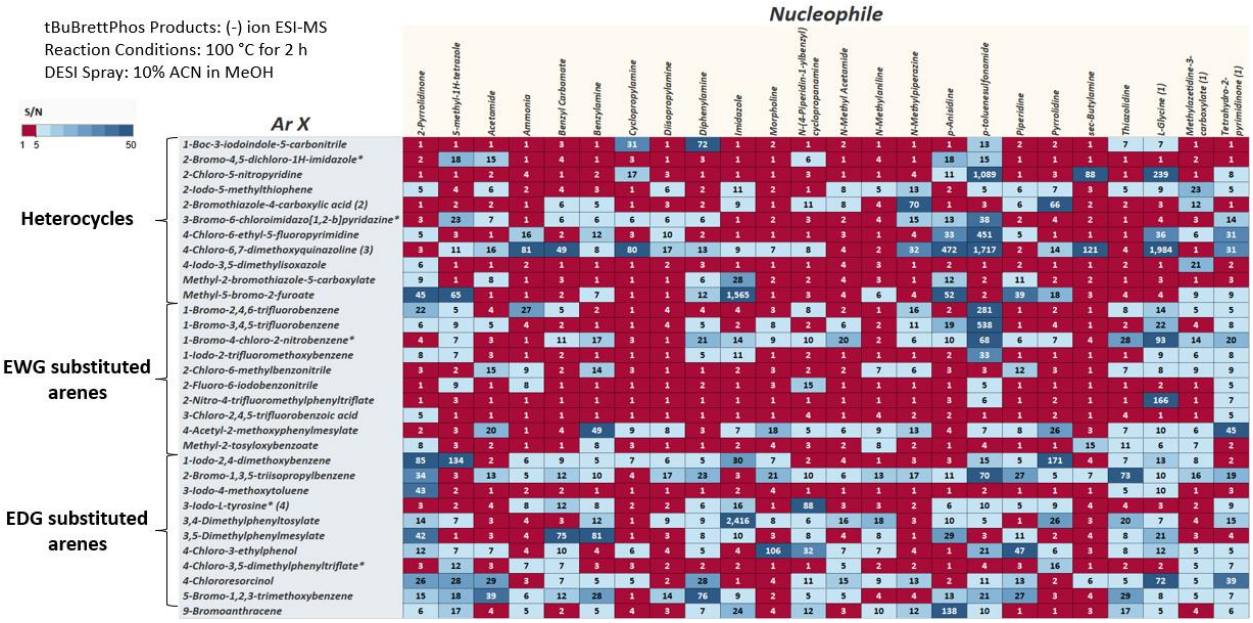

Figure 35. Negative ion heat map from the *t*BuBrettPhos experiment after sitting at 100 °C for 2 h. (1) is 50% *t*BuOH in H_2O. (2) is 30% 1,4-Dioxane in *t*BuOH. (3) is 10% *t*BuOH in PhMe. (4) is 20% *t*BuOH, 30% 1,4-Dioxane, 50% H_2O.

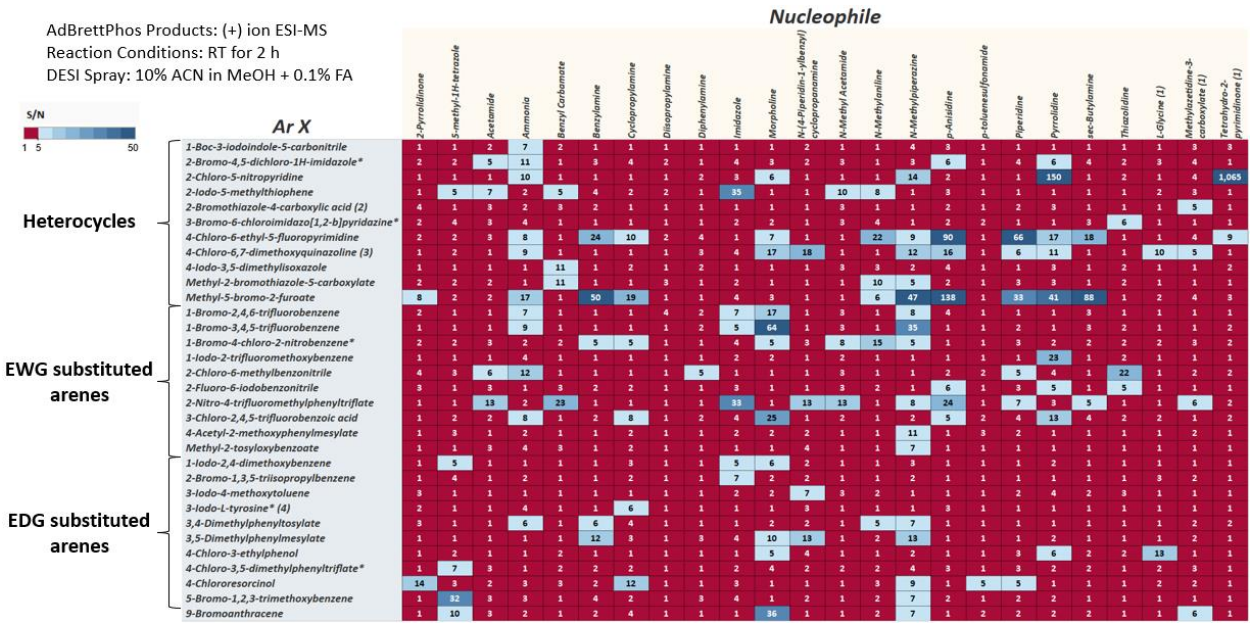

Figure 36. Positive ion heat map from the AdBrettPhos experiment after sitting at RT for 2 h. (1) is 50% *t*BuOH in H_2O. (2) is 30% 1,4-Dioxane in *t*BuOH. (3) is 10% *t*BuOH in PhMe. (4) is 20% *t*BuOH, 30% 1,4-Dioxane, 50% H_2O.

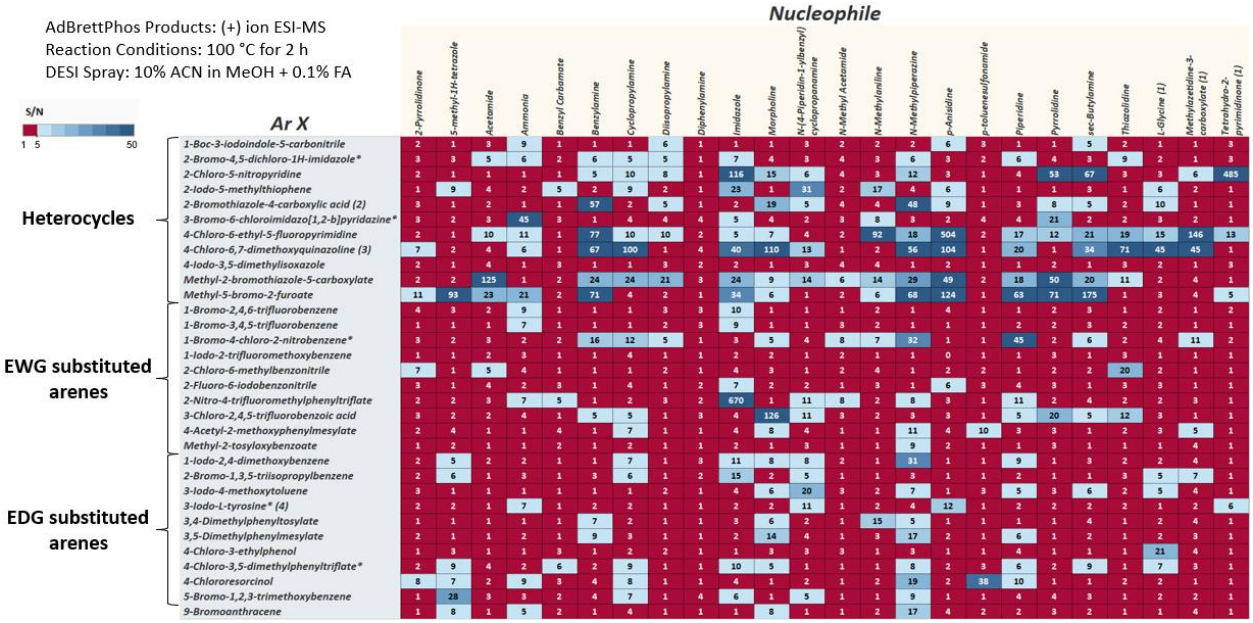

Figure 37. Positive ion heat map from the AdBrettPhos experiment after sitting at 100 °C for 2 h. (1) is 50% *t*BuOH in H_2O. (2) is 30% 1,4-Dioxane in *t*BuOH. (3) is 10% *t*BuOH in PhMe. (4) is 20% *t*BuOH, 30% 1,4-Dioxane, 50% H_2O.

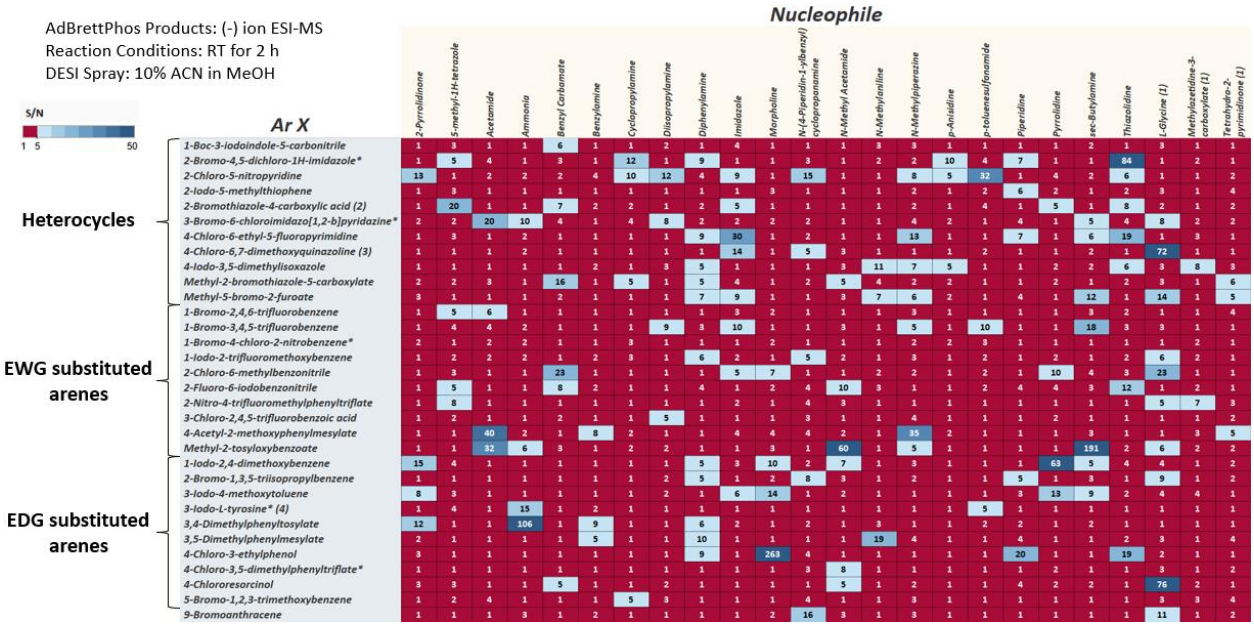

Figure 38. Negative ion heat map from the AdBrettPhos experiment after sitting at RT for 2 h. (1) is 50% *t*BuOH in H_2O. (2) is 30% 1,4-Dioxane in *t*BuOH. (3) is 10% *t*BuOH in PhMe. (4) is 20% *t*BuOH, 30% 1,4-Dioxane, 50% H_2O.

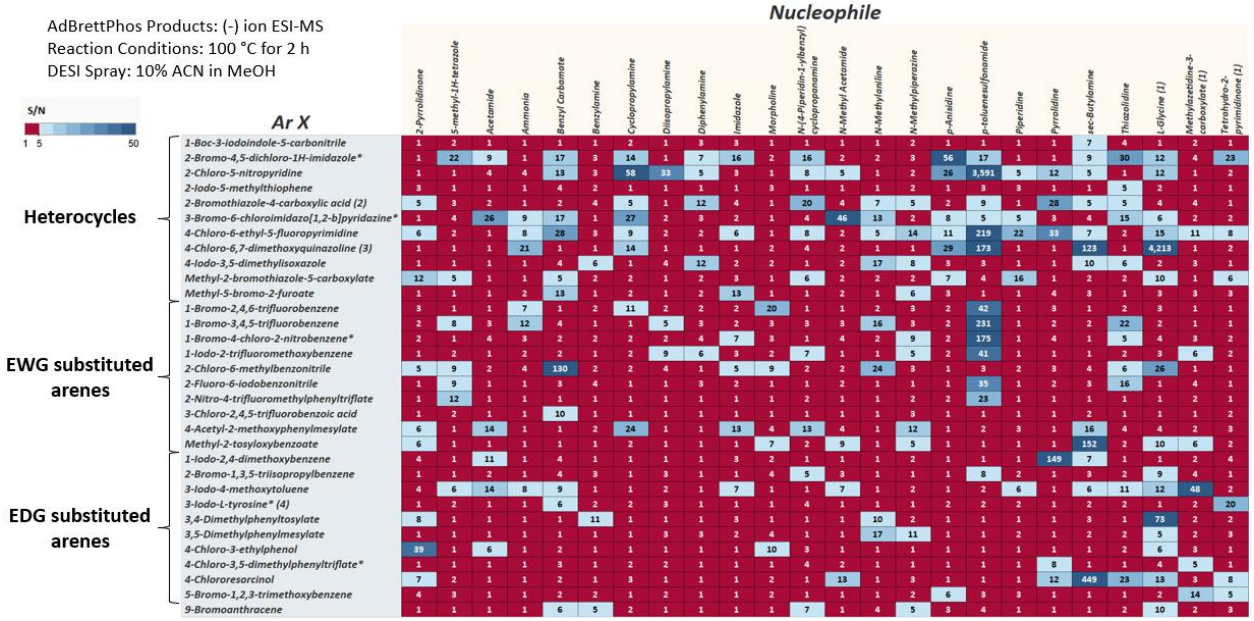

Figure 39. Negative ion heat map from the AdBrettPhos experiment after sitting at 100 °C for 2 h. (1) is 50% *t*BuOH in H_2O. (2) is 30% 1,4-Dioxane in *t*BuOH. (3) is 10% *t*BuOH in PhMe. (4) is 20% *t*BuOH, 30% 1,4-Dioxane, 50% H_2O.

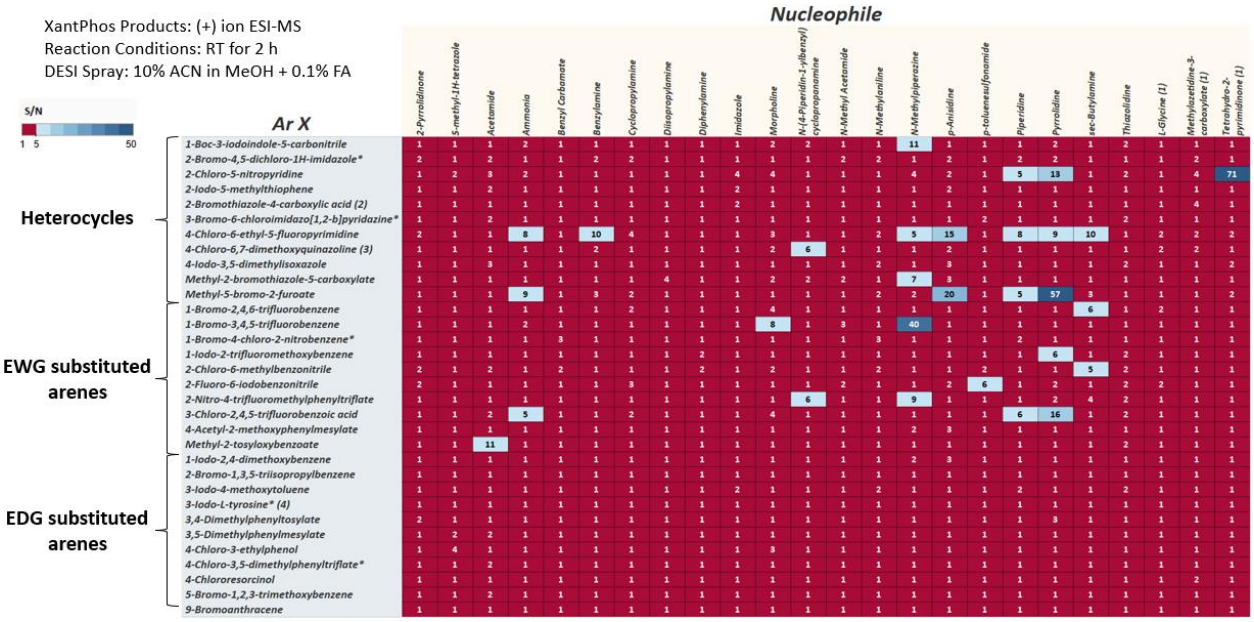

Figure 40. Positive ion heat map from the XantPhos experiment after sitting at RT for 2 h. (1) is 50% *t*BuOH in H_2O. (2) is 30% 1,4-Dioxane in *t*BuOH. (3) is 10% *t*BuOH in PhMe. (4) is 20% *t*BuOH, 30% 1,4-Dioxane, 50% H_2O.

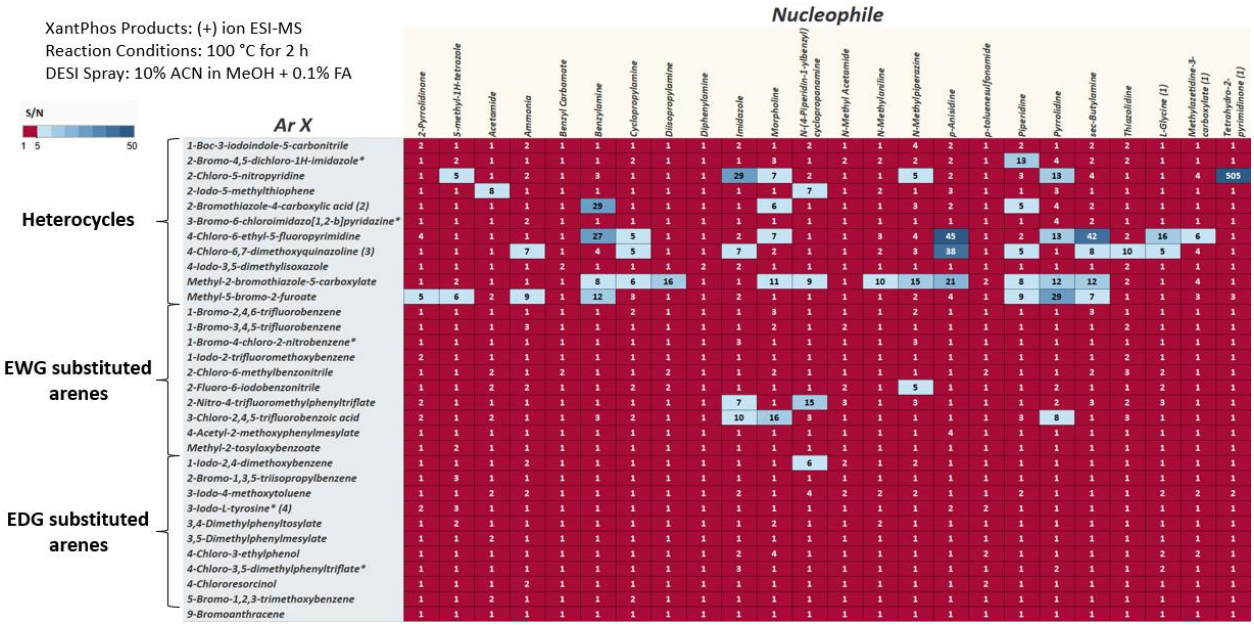

Figure 41. Positive ion heat map from the XantPhos experiment after sitting at 100 °C for 2 h. (1) is 50% *t*BuOH in H_2O. (2) is 30% 1,4-Dioxane in *t*BuOH. (3) is 10% *t*BuOH in PhMe. (4) is 20% *t*BuOH, 30% 1,4-Dioxane, 50% H_2O.

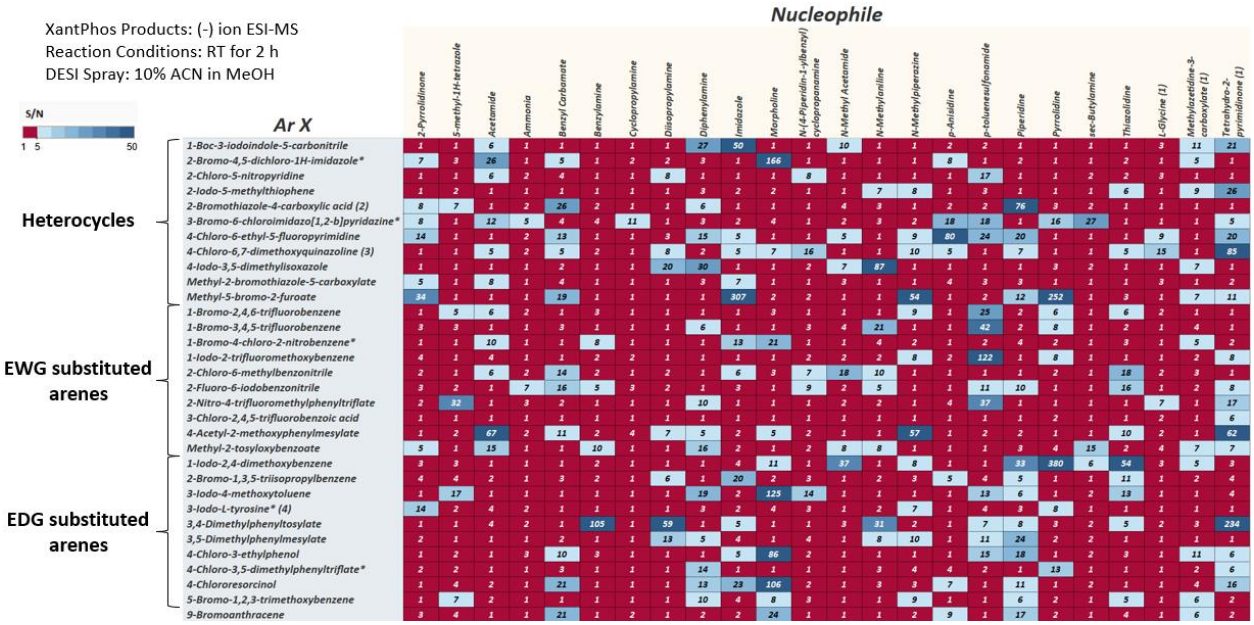

Figure 42. Negative ion heat map from the XantPhos experiment after sitting at RT for 2 h. (1) is 50% *t*BuOH in H_2O. (2) is 30% 1,4-Dioxane in *t*BuOH. (3) is 10% *t*BuOH in PhMe. (4) is 20% *t*BuOH, 30% 1,4-Dioxane, 50% H_2O.

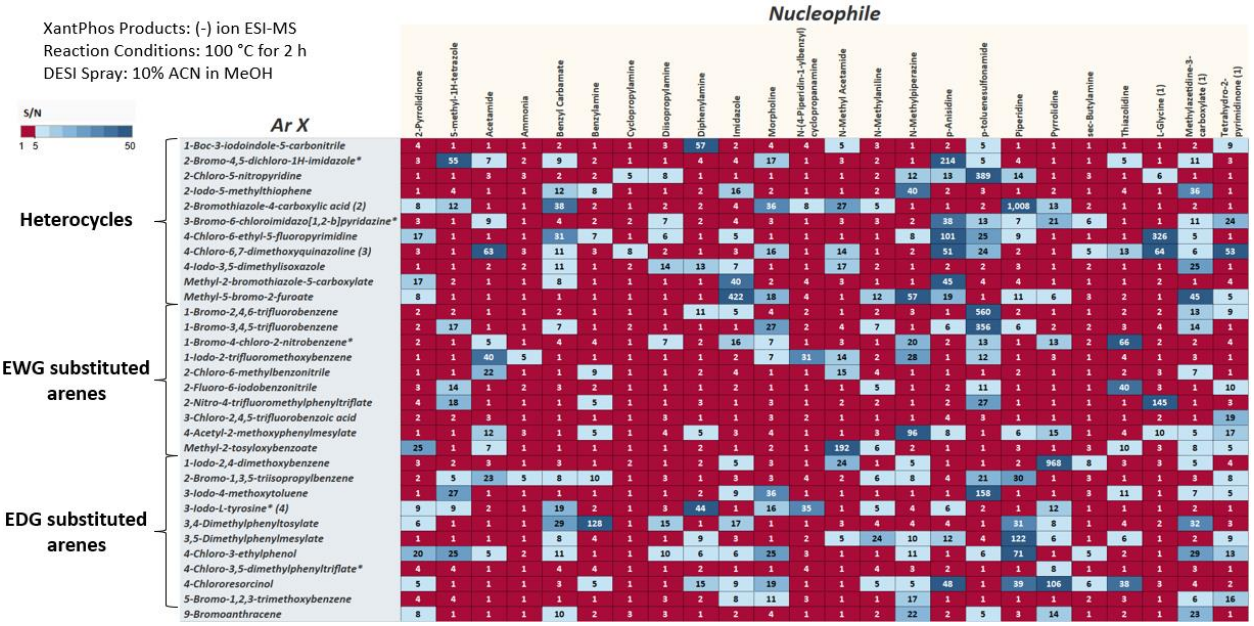

Figure 43. Negative ion heat map from the XantPhos experiment after sitting at 100 °C for 2 h. (1) is 50% *t*BuOH in H_2O. (2) is 30% 1,4-Dioxane in *t*BuOH. (3) is 10% *t*BuOH in PhMe. (4) is 20% *t*BuOH, 30% 1,4-Dioxane, 50% H_2O.

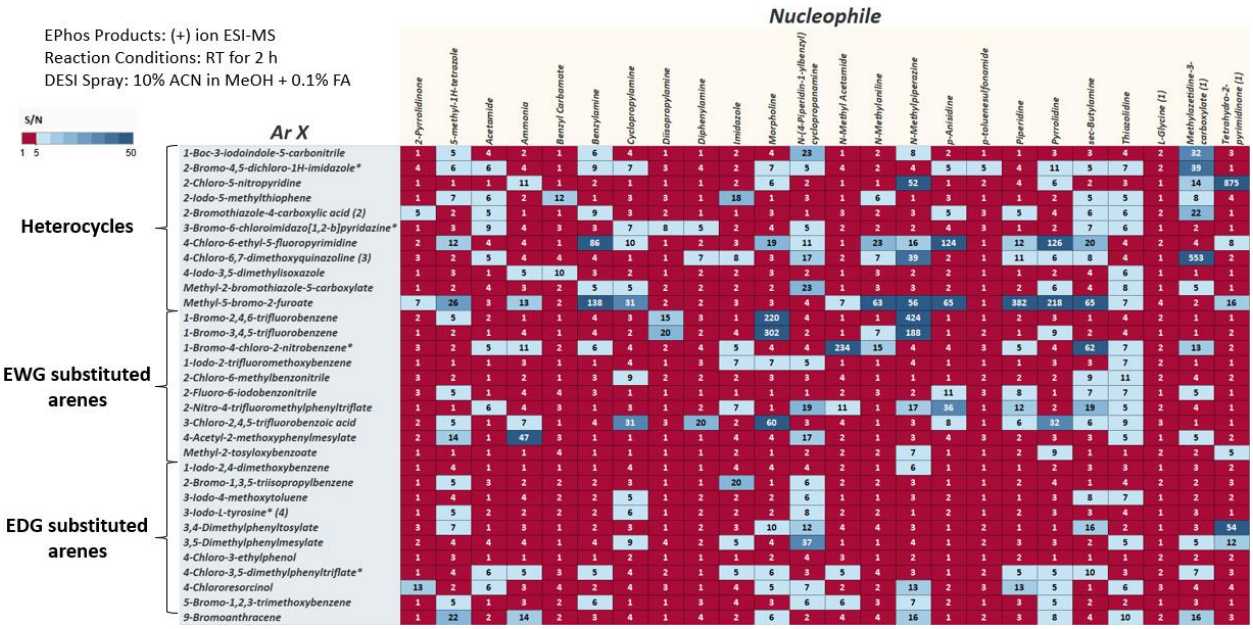

Figure 44. Positive ion heat map from the EPhos experiment after sitting at RT for 2 h. (1) is 50% *t*BuOH in H_2O. (2) is 30% 1,4-Dioxane in *t*BuOH. (3) is 10% *t*BuOH in PhMe. (4) is 20% *t*BuOH, 30% 1,4-Dioxane, 50% H_2O.

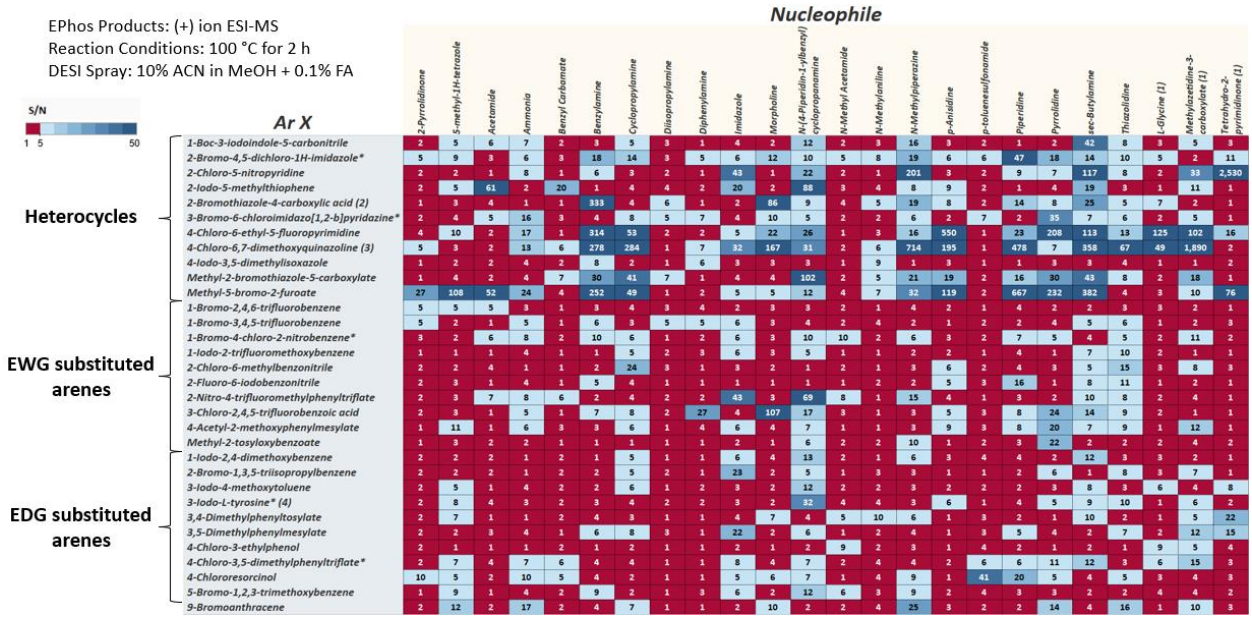

Figure 45. Positive ion heat map from the EPhos experiment after sitting at 100 °C for 2 h. (1) is 50% *t*BuOH in H_2O. (2) is 30% 1,4-Dioxane in *t*BuOH. (3) is 10% *t*BuOH in PhMe. (4) is 20% *t*BuOH, 30% 1,4-Dioxane, 50% H_2O.

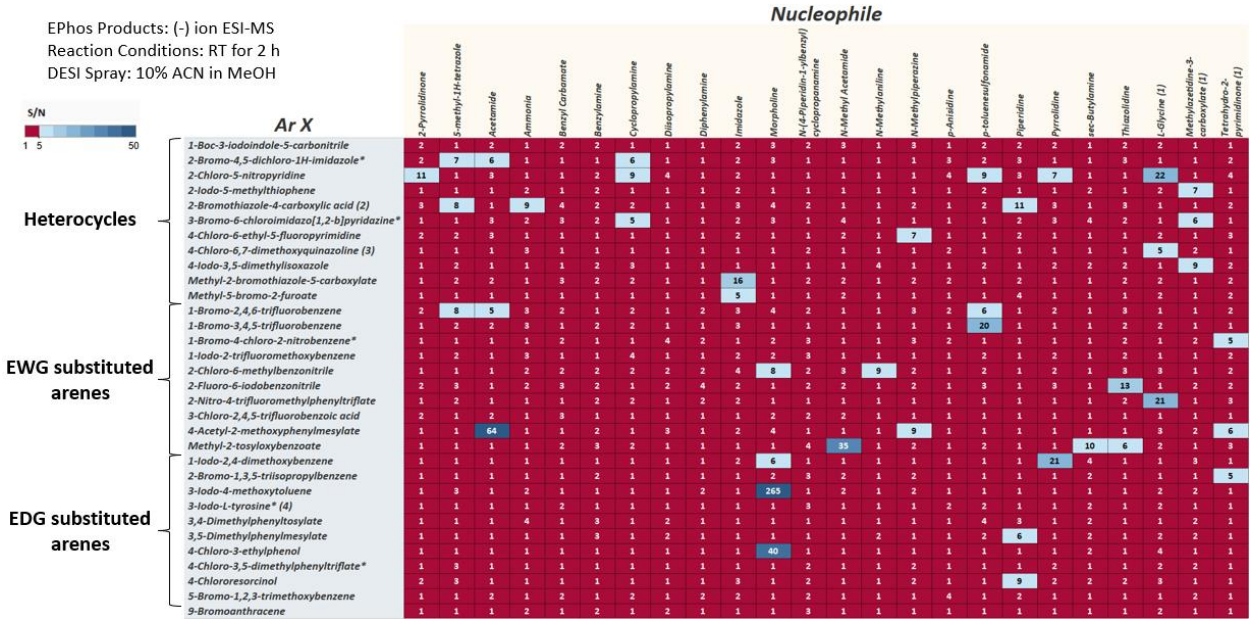

Figure 46. Negative ion heat map from the EPhos experiment after sitting at RT for 2 h. (1) is 50% *t*BuOH in H_2O. (2) is 30% 1,4-Dioxane in *t*BuOH. (3) is 10% *t*BuOH in PhMe. (4) is 20% *t*BuOH, 30% 1,4-Dioxane, 50% H_2O.

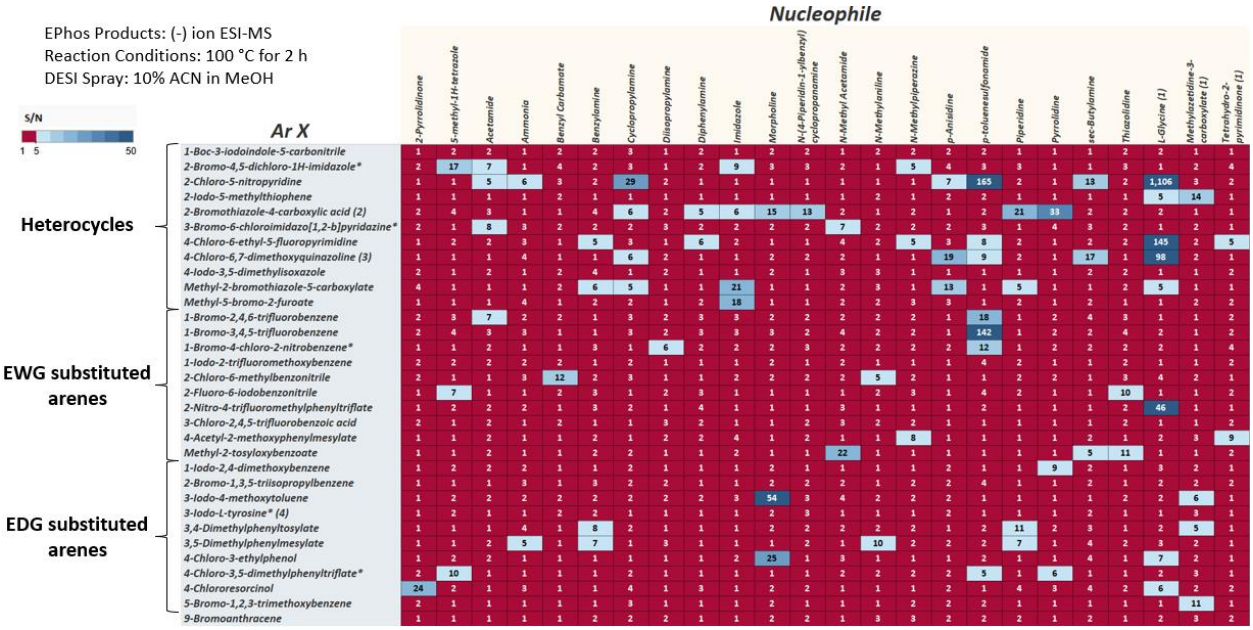

Figure 47. Negative ion heat map from the EPhos experiment after sitting at 100 °C for 2 h. (1) is 50% *t*BuOH in H_2O. (2) is 30% 1,4-Dioxane in *t*BuOH. (3) is 10% *t*BuOH in PhMe. (4) is 20% *t*BuOH, 30% 1,4-Dioxane, 50% H_2O.

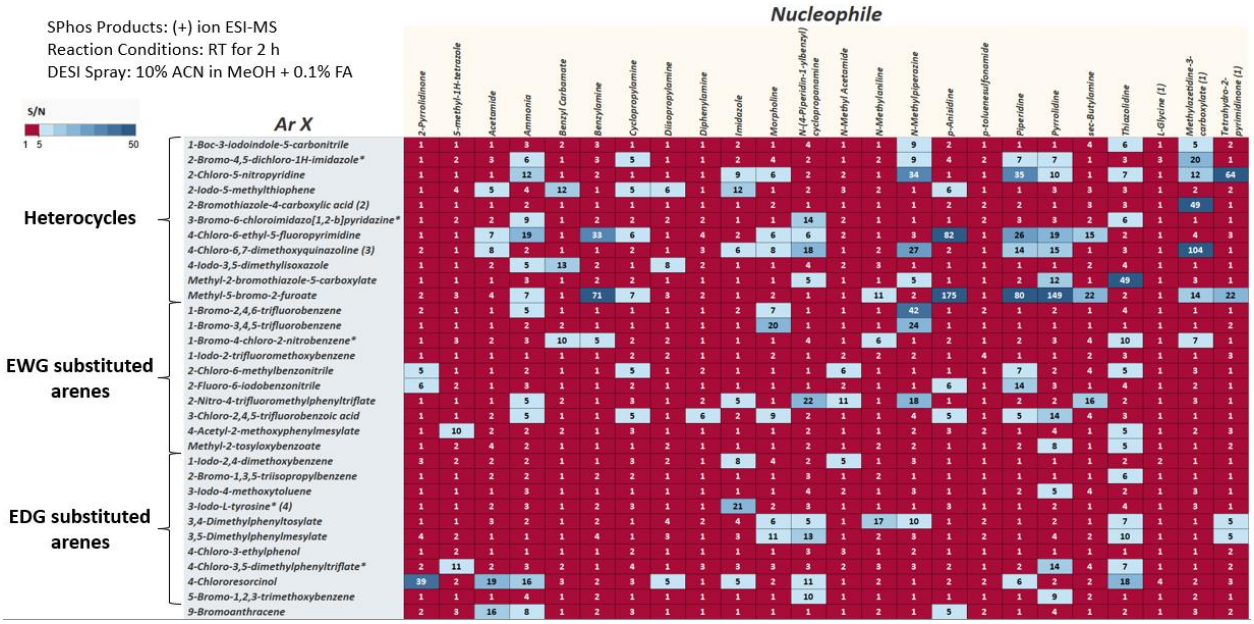

Figure 48. Positive ion heat map from the SPhos experiment after sitting at RT for 2 h. (1) is 50% *t*BuOH in H_2O. (2) is 30% 1,4-Dioxane in *t*BuOH. (3) is 10% *t*BuOH in PhMe. (4) is 20% *t*BuOH, 30% 1,4-Dioxane, 50% H_2O.

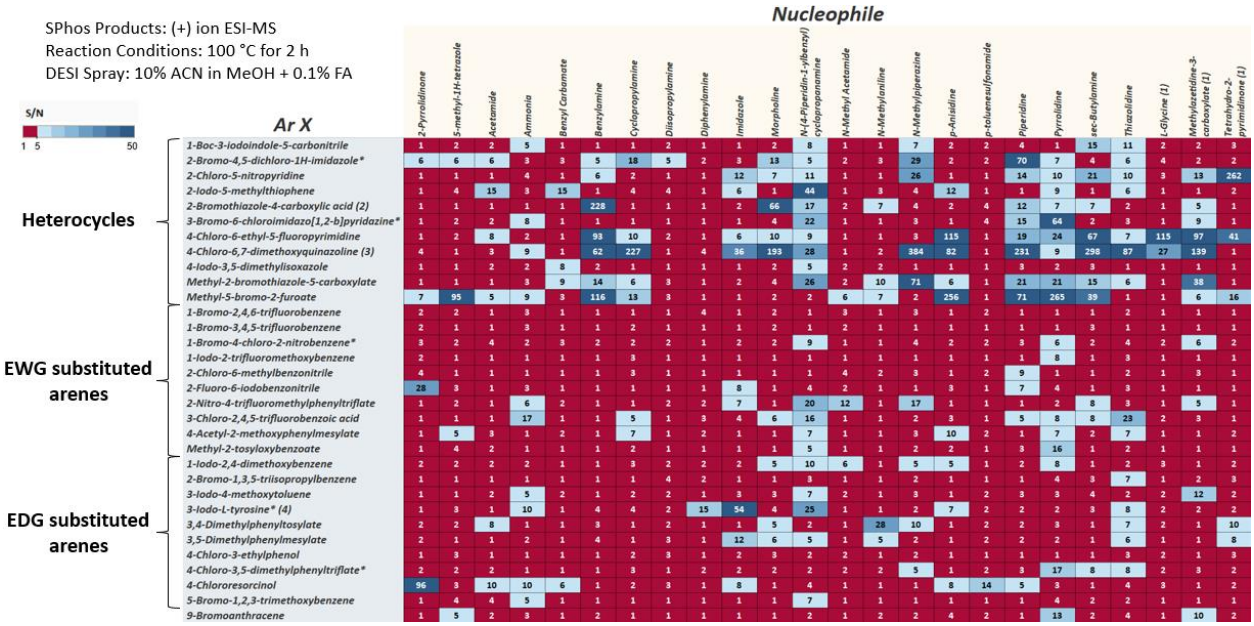

Figure 49. Positive ion heat map from the SPhos experiment after sitting at 100 °C for 2 h. (1) is 50% *t*BuOH in H_2O. (2) is 30% 1,4-Dioxane in *t*BuOH. (3) is 10% *t*BuOH in PhMe. (4) is 20% *t*BuOH, 30% 1,4-Dioxane, 50% H_2O.

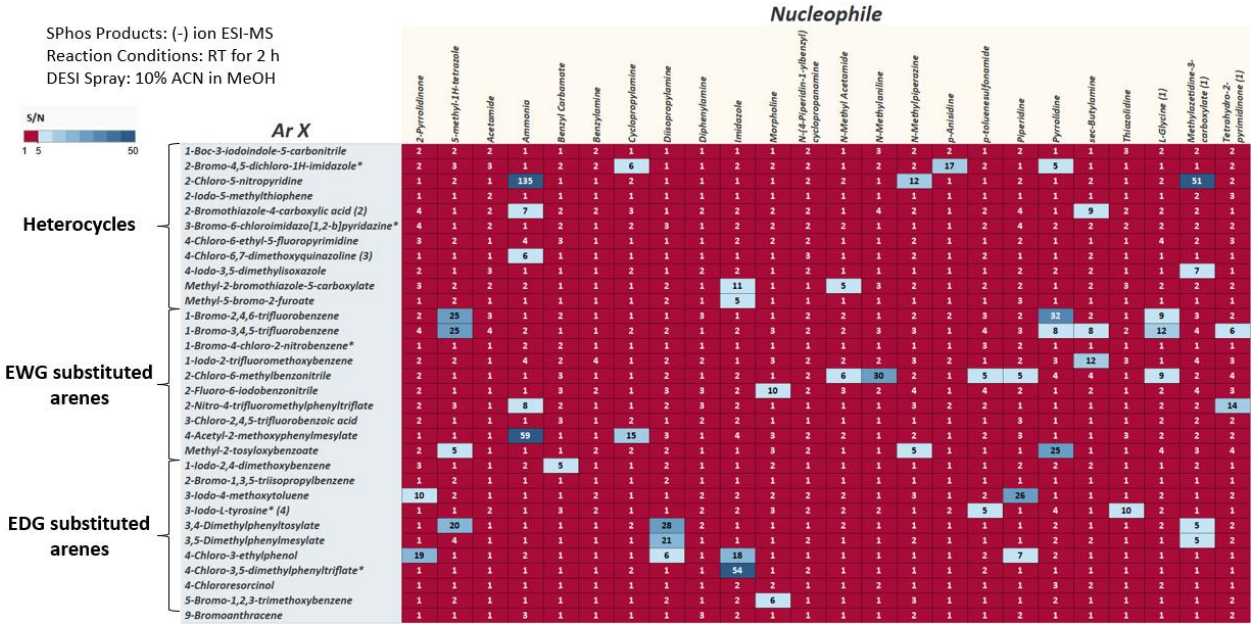

Figure 50. Negative ion heat map from the SPhos experiment after sitting at RT for 2 h. (1) is 50% *t*BuOH in H_2O. (2) is 30% 1,4-Dioxane in *t*BuOH. (3) is 10% *t*BuOH in PhMe. (4) is 20% *t*BuOH, 30% 1,4-Dioxane, 50% H_2O.

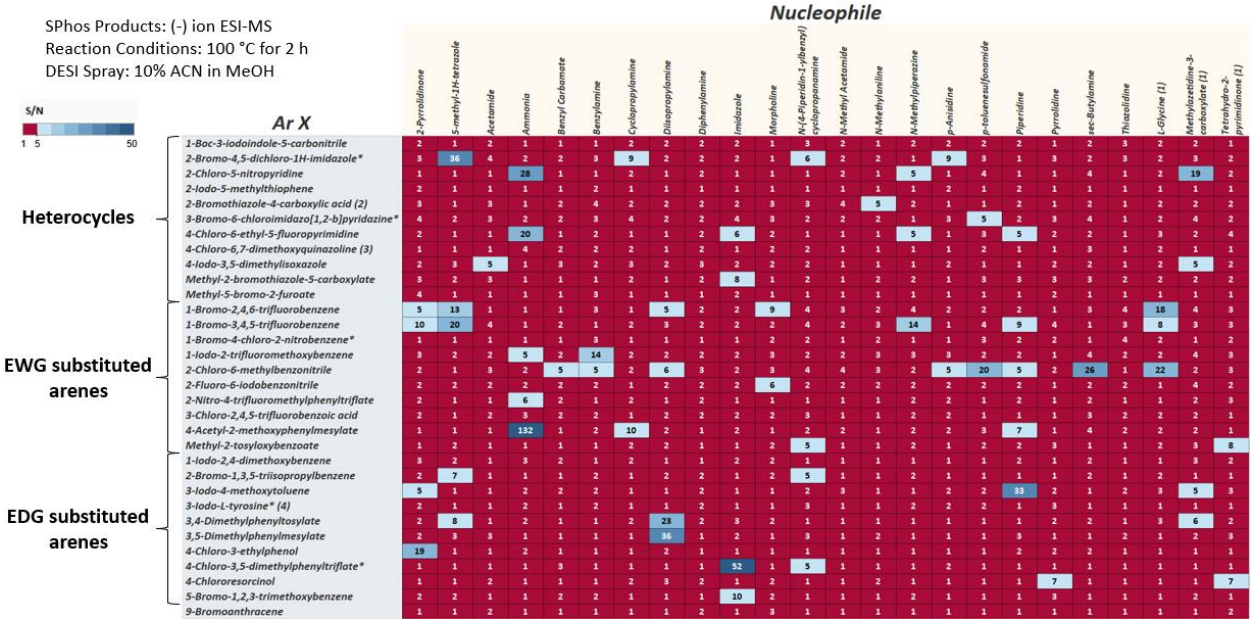

Figure 51. Negative ion heat map from the SPhos experiment after sitting at 100 °C for 2 h. (1) is 50% *t*BuOH in H_2O. (2) is 30% 1,4-Dioxane in *t*BuOH. (3) is 10% *t*BuOH in PhMe. (4) is 20% *t*BuOH, 30% 1,4-Dioxane, 50% H_2O.

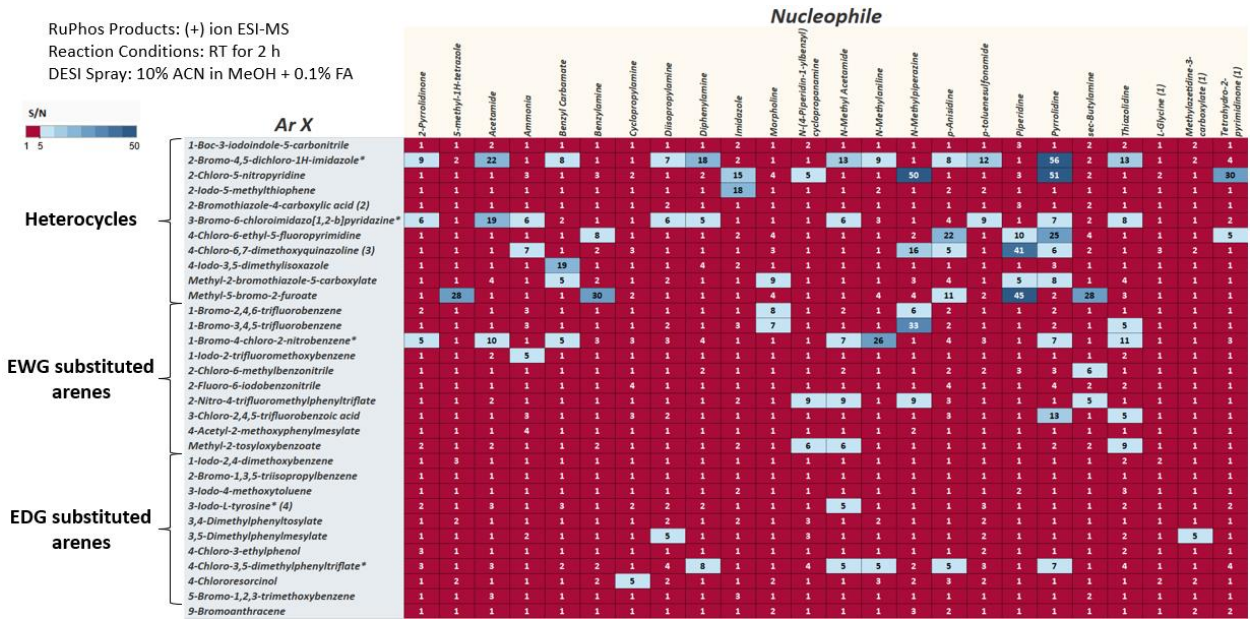

Figure 52. Positive ion heat map from the RuPhos experiment after sitting at RT for 2 h. (1) is 50% *t*BuOH in H_2O. (2) is 30% 1,4-Dioxane in *t*BuOH. (3) is 10% *t*BuOH in PhMe. (4) is 20% *t*BuOH, 30% 1,4-Dioxane, 50% H_2O.

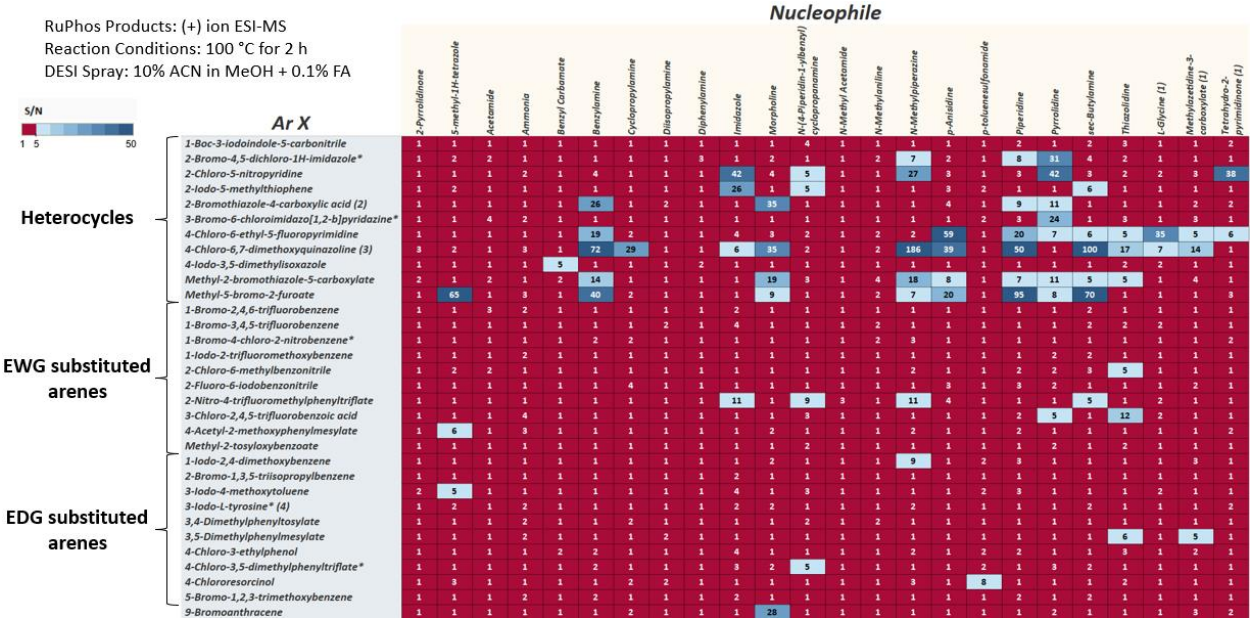

Figure 53. Positive ion heat map from the RuPhos experiment after sitting at 100 °C for 2 h. (1) is 50% *t*BuOH in H_2O. (2) is 30% 1,4-Dioxane in *t*BuOH. (3) is 10% *t*BuOH in PhMe. (4) is 20% *t*BuOH, 30% 1,4-Dioxane, 50% H_2O.

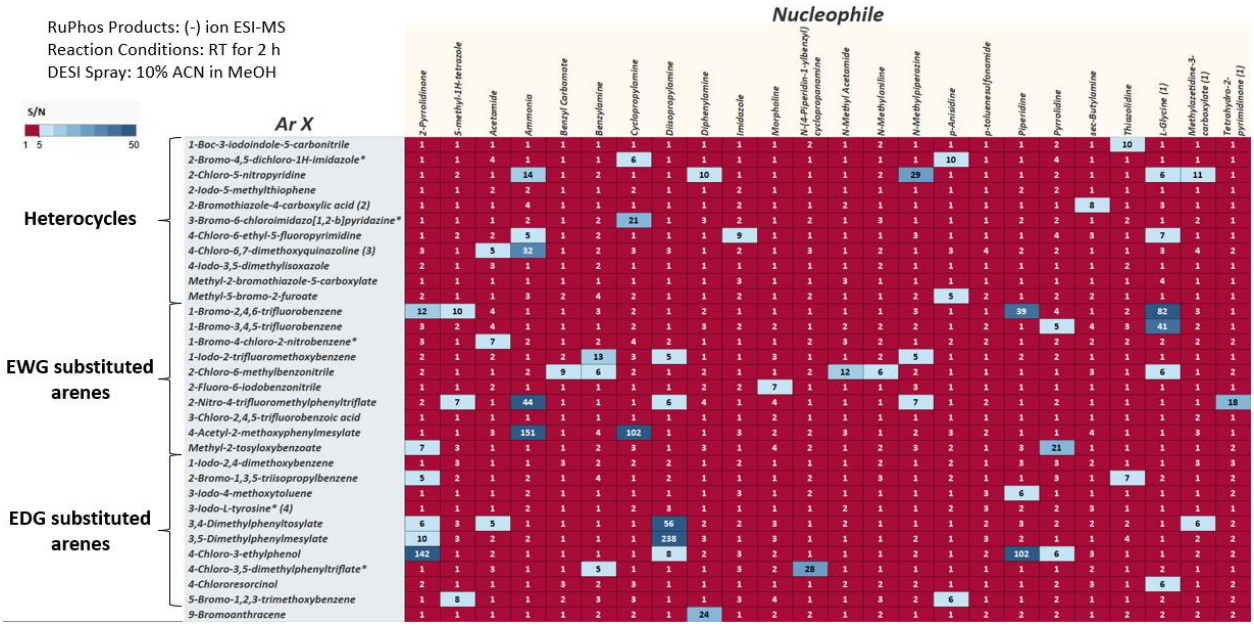

Figure 54. Negative ion heat map from the RuPhos experiment after sitting at RT for 2 h. (1) is 50% *t*BuOH in H_2O. (2) is 30% 1,4-Dioxane in *t*BuOH. (3) is 10% *t*BuOH in PhMe. (4) is 20% *t*BuOH, 30% 1,4-Dioxane, 50% H_2O.

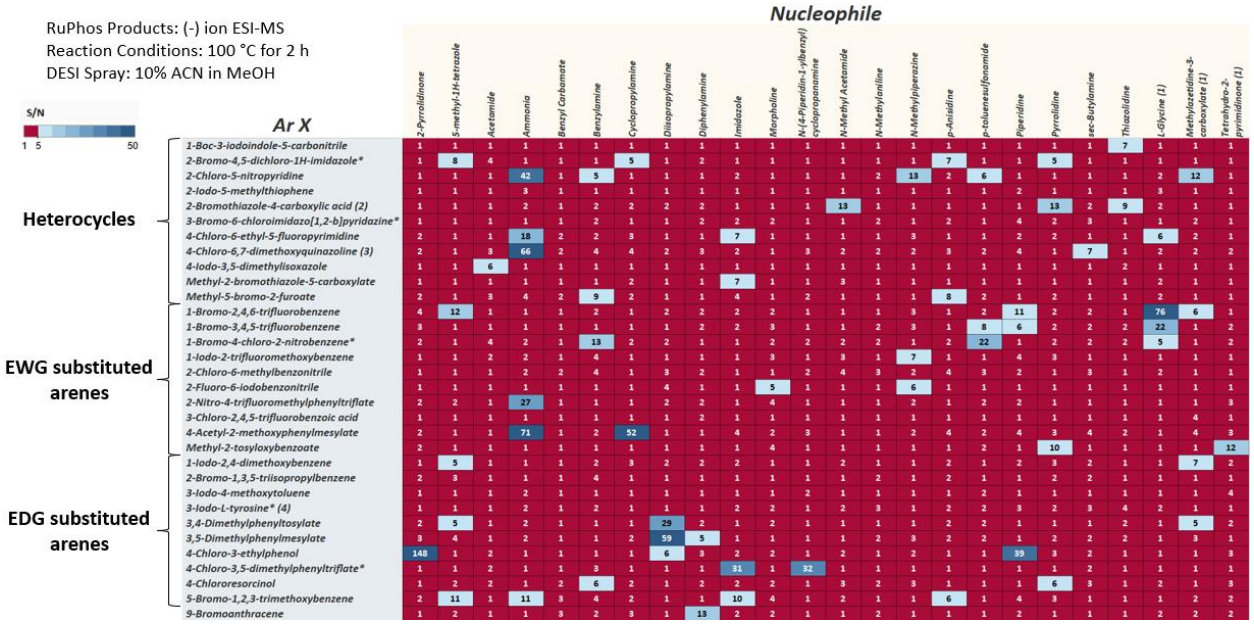

Figure 55. Negative ion heat map from the RuPhos experiment after sitting at 100 °C for 2 h. (1) is 50% *t*BuOH in H_2O. (2) is 30% 1,4-Dioxane in *t*BuOH. (3) is 10% *t*BuOH in PhMe. (4) is 20% *t*BuOH, 30% 1,4-Dioxane, 50% H_2O.

2.5.4 NMR Spectra

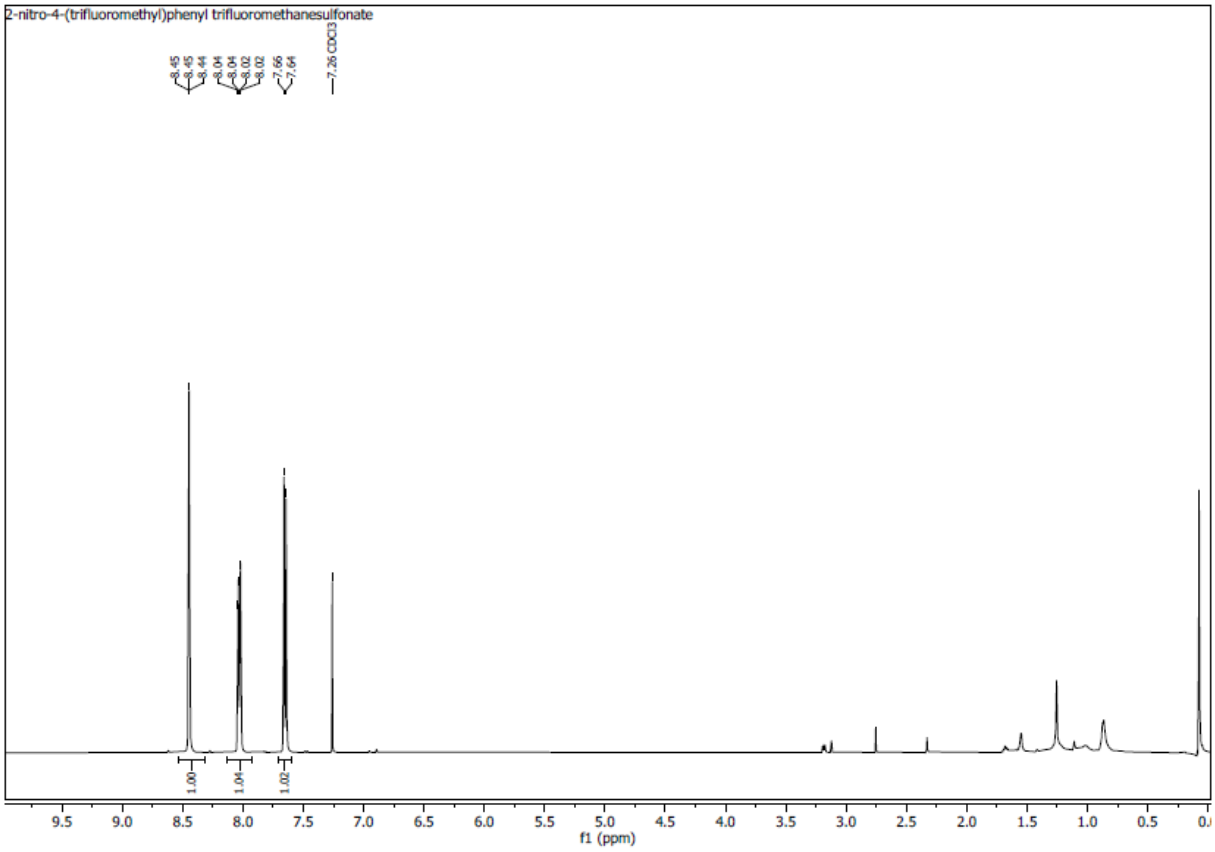

Figure 56. ^{1}H NMR spectrum of 2-nitro-4-(trifluoromethyl)phenyl trifluoromethanesulfonate in $CDCl_3$.

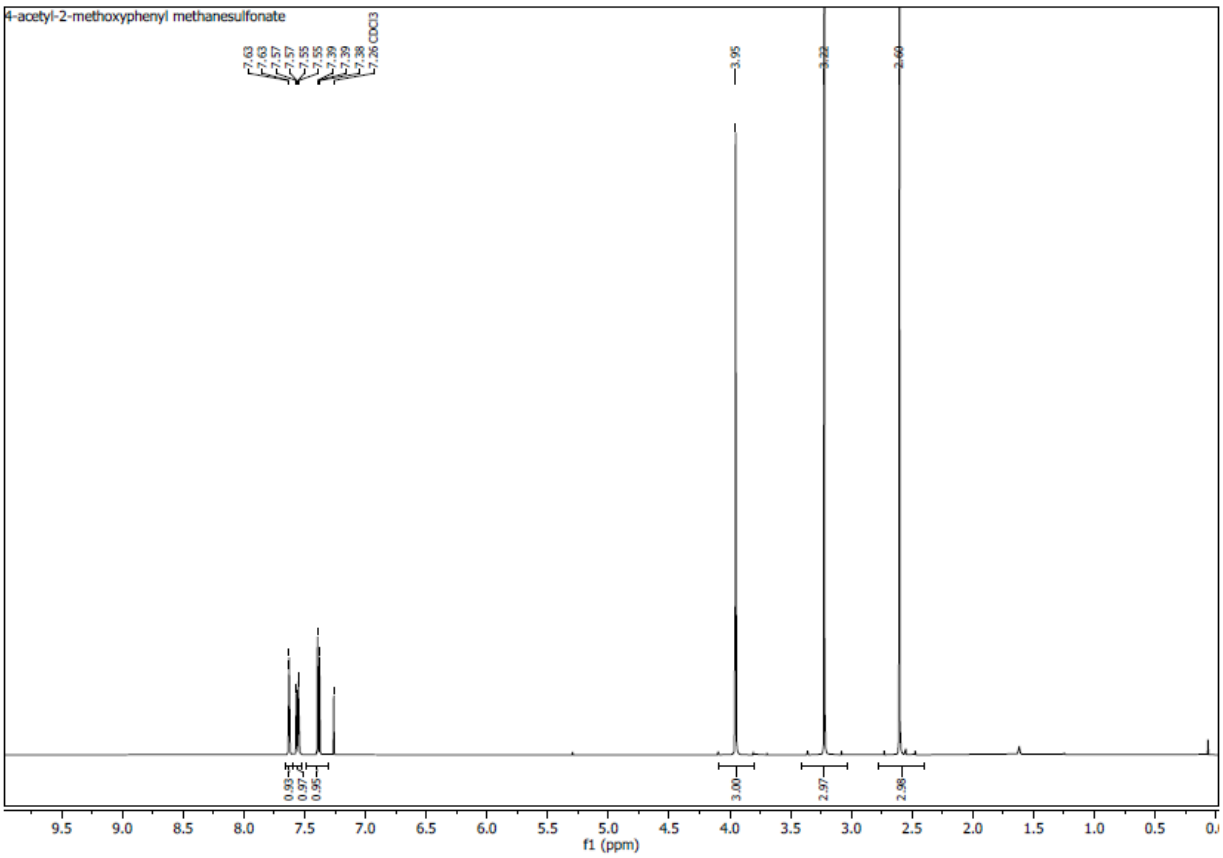

Figure 57. ^{1}H NMR spectrum of 4-acetyl-2-methoxyphenyl methanesulfonate in $CDCl_3$.

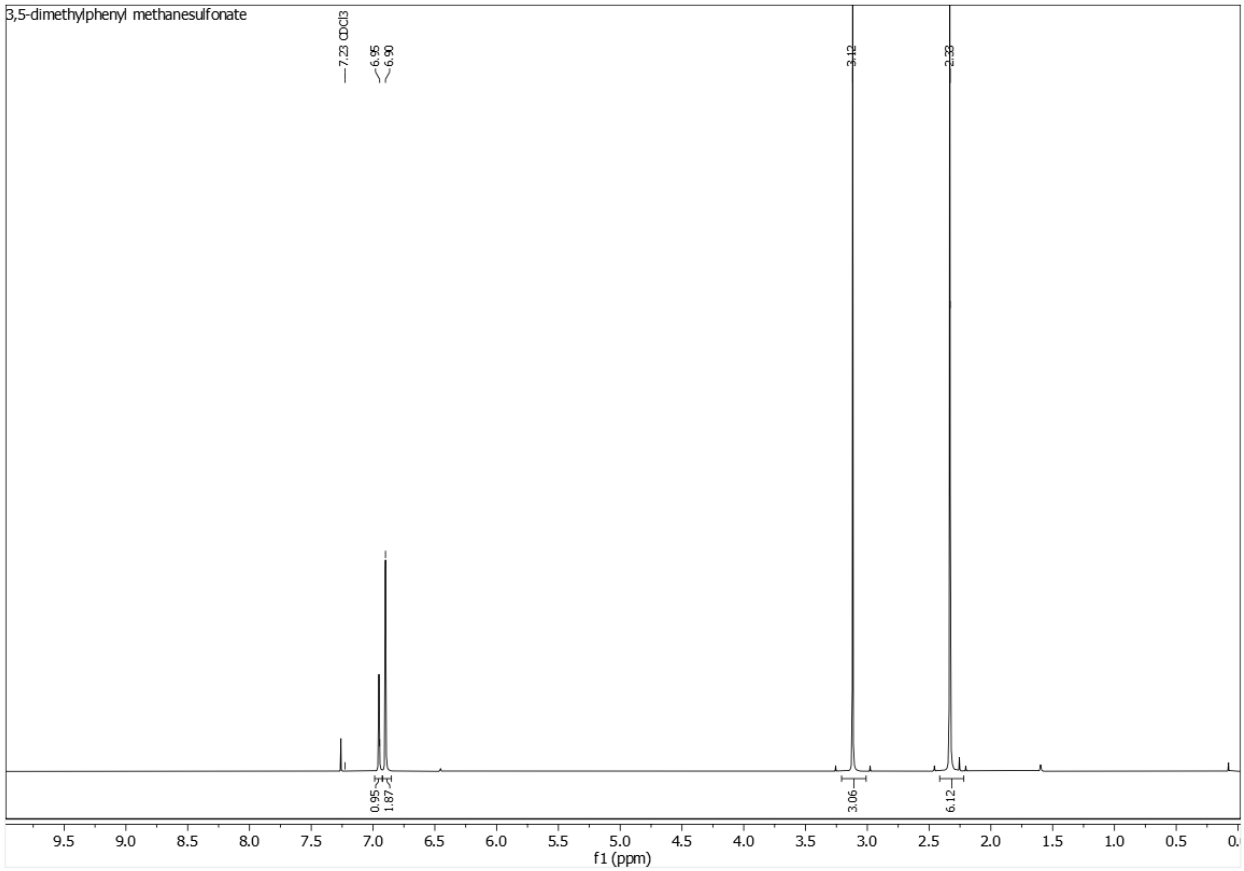

Figure 58. ^{1}H NMR spectrum of 3,5-dimethylphenyl methanesulfonate in $CDCl_3$.

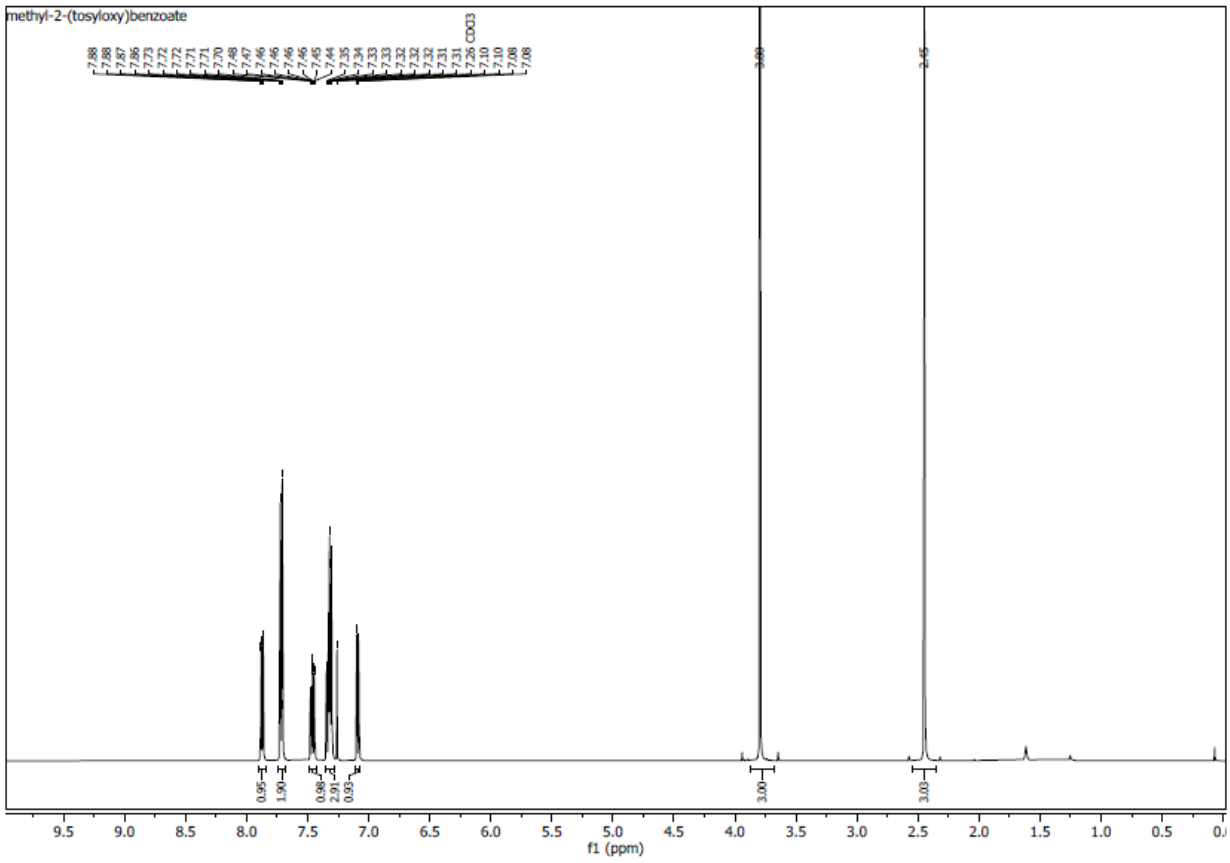

Figure 59. ^{1}H NMR spectrum of methyl-2-(tosyloxy)benzoate in $CDCl_3$.

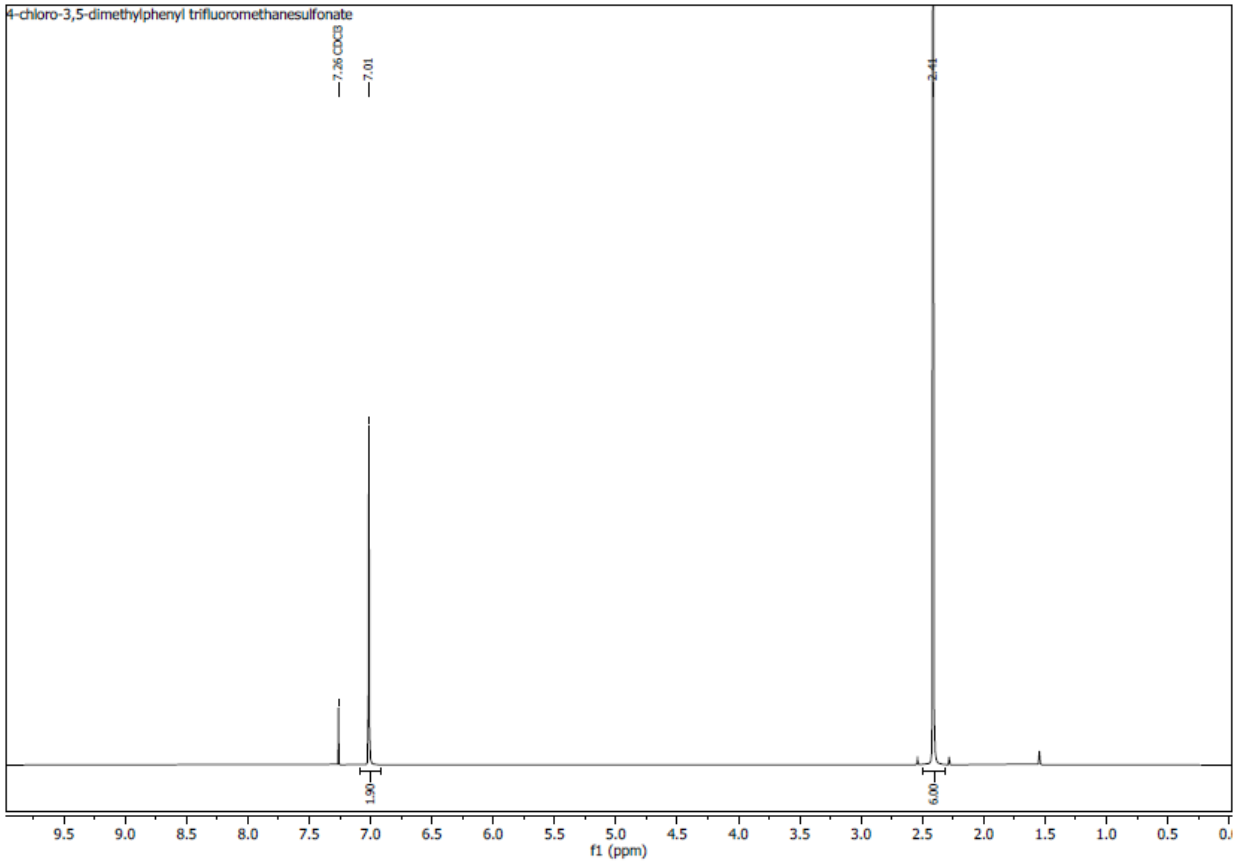

Figure 60. ^{1}H NMR spectrum of 4-chloro-3,5-dimethylphenyl trifluoromethanesulfonate in $CDCl_3$.

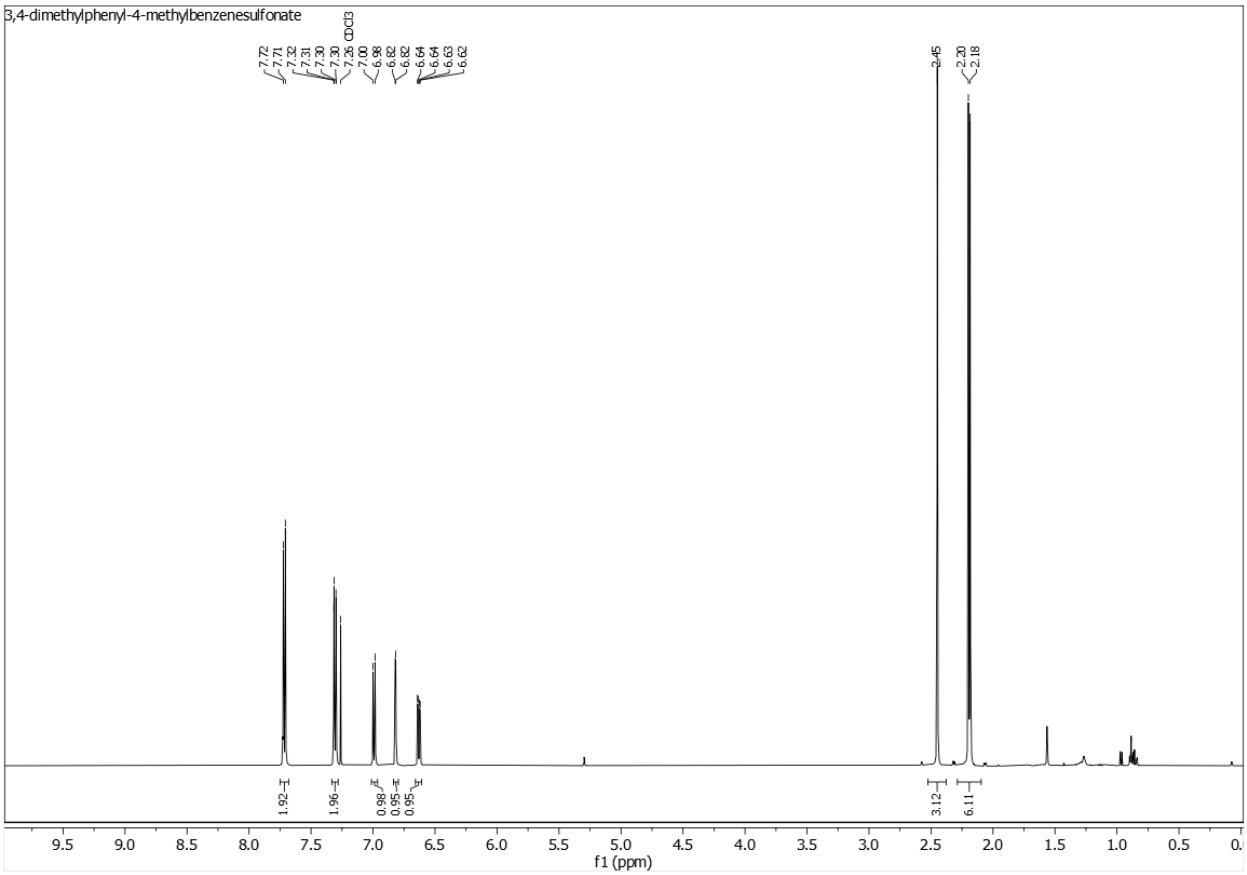

Figure 61. ^{1}H NMR spectrum of 3,4-dimethylphenyl-4-methylbenzenesulfonate in $CDCl_3$.

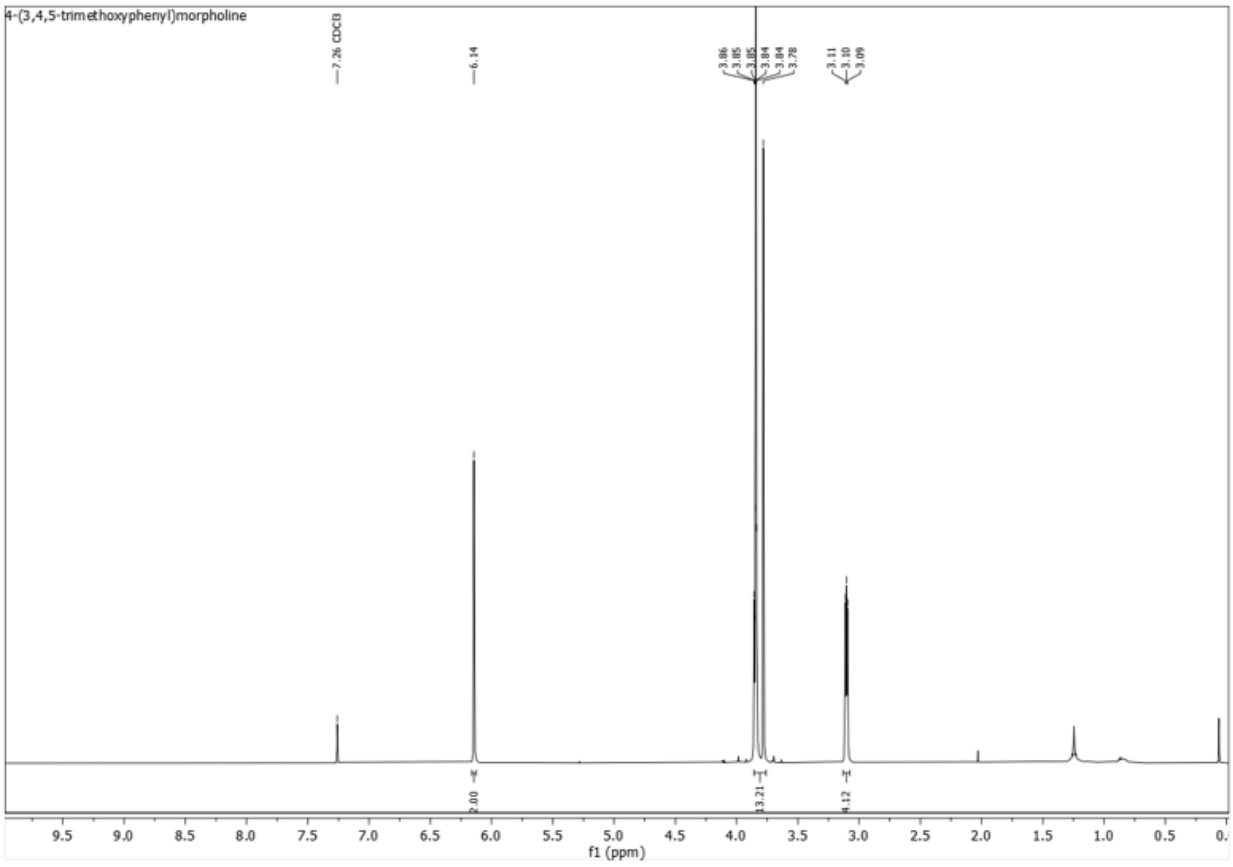

Figure 62. ^{1}H NMR spectrum of 4-(3,4,5-trimethoxyphenyl)morpholine in $CDCl_3$.

2.6 References

(1) Jaman, Z.; Mufti, A.; Sah, S.; Avramova, L.; Thompson, D. H. High Throughput Experimentation and Continuous Flow Validation of Suzuki–Miyaura Cross-Coupling Reactions. *Chemistry – A European Journal.* **2018**, *24* (38), 9546–9554. https://doi.org/10.1002/chem.201801165.

(2) Wleklinski, M.; Loren, B. P.; Ferreira, C. R.; Jaman, Z.; Avramova, L.; Sobreira, T. J. P.; Thompson, D. H.; Cooks, R. G., High Throughput Reaction Screening Using Desorption Electrospray Ionization Mass Spectrometry. *Chem. Sci.* **2018**, 9, 1647-1653.

(3) Tardiff, B. J.; Stradiotto, M. Buchwald–Hartwig Amination of (Hetero)Aryl Chlorides by Employing Mor-DalPhos under Aqueous and Solvent-Free Conditions. *European Journal of Organic Chemistry.* **2012**, *2012* (21), 3972–3977. https://doi.org/10.1002/ejoc.201200510.

(4) Renault, Y. J. G.; Lynch, R.; Marelli, E.; Sharma, S. V.; Pubill-Ulldemolins, C.; Sharp, J. A.; Cartmell, C.; Cárdenas, P.; Goss, R. J. M. Buchwald Hartwig Diversification of Unprotected Halotryptophans, Halotryptophan Containing Tripeptides and the Natural Product Barettin in Aqueous Conditions. *Chem. Commun.* **2019**, *55* (91), 13653–13656. https://doi.org/10.1039/C9CC02554E.

(5) Logsdon, D. L.; Li, Y.; Paschoal Sobreira, T. J.; Ferreira, C. R.; Thompson, D. H.; Cooks, R. G. High-Throughput Screening of Reductive Amination Reactions Using Desorption Electrospray Ionization Mass Spectrometry. *Org. Process Res. Dev.* **2020**, *24* (9), 1647–1657. https://doi.org/10.1021/acs.oprd.0c00230.